

**HYDRODYNAMIC, SEDIMENT TRANSPORT AND WIND WAVES IN  
AN ERODING SALT MARSH ENVIRONMENT, BOMBAY HOOK  
NATIONAL WILDLIFE REFUGE, DELAWARE**

Mithun Deb<sup>1</sup>, Ali Abdolali<sup>2,3</sup>, James T. Kirby<sup>1</sup>, and Fengyan Shi<sup>1</sup>

<sup>1</sup>Center for Applied Coastal Research, Department of Civil and Environmental Engineering,  
University of Delaware, Newark, DE 19716 USA

<sup>2</sup>NWS/NCEP/Environmental Modeling Center, National Oceanic and Atmospheric  
Administration (NOAA), College Park, MD 20740 USA

<sup>3</sup>University Corporation for Atmospheric Research (UCAR), Boulder, CO 80301 USA

**RESEARCH REPORT NO. CACR-18-04**

Research Supported by

The National Fish and Wildlife Foundation, Grant #43752

National Oceanic and Atmospheric Administration (NOAA)  
Award No. NA18OAR4170086, Project RRCE-12



**CENTER FOR APPLIED COASTAL RESEARCH**

Coastal Engineering Laboratory  
University of Delaware  
Newark, Delaware 19716

## Abstract

This report describes the development and validation of a 3D numerical code for simulating hydrodynamic and sediment processes in Bombay Hook National Wildlife Refuge, Delaware. The modeling employs the 2D, depth-integrated version of the open source model FVCOM, which solves the hydrostatic equations for fluid motion, salinity, temperature and sediment load on a horizontally unstructured grid. The 2D model is validated against water level and current data. The model is then extended to 3D to incorporate modeling of suspended sediment transport. The model is used to examine several scenarios for modification to flow and sediment transport based on historical estimates or future possible alterations to marsh channel geometry. The report identifies a significant modeling problem associated with artificial ponding or storage of water in isolated depressions in the model grid. This effect limits the expected accuracy of estimates of sediment flux rates and net water and sediment pathways in the marsh system, and serves as the basis for additional work funded by Sea Grant. The report also describes a study of wind wave climate in an alternately wet and dry tidal flat area within the marsh. Additional work on analysis of historic sedimentation rates and sediment budget within the marsh system are reported separately by [McDowell \(2017\)](#). Project-supported data collection carried out in support of this effort is reported in [Deb \*et al.\* \(2018\)](#).

# Contents

<b>1</b>	<b>Introduction</b>	<b>1</b>
1.1	Study area . . . . .	5
<b>2</b>	<b>Model DEM and grid development</b>	<b>6</b>
2.1	LiDAR data sets . . . . .	7
2.2	Vegetation bias correction . . . . .	12
2.2.1	Minimum Bin Technique . . . . .	12
2.2.2	Artificial Neural Network . . . . .	13
2.3	Unstructured grid development . . . . .	23
<b>3</b>	<b>FVCOM hydrodynamic modeling and validation (2D)</b>	<b>26</b>
3.1	FVCOM model description . . . . .	27
3.1.1	Model forcing . . . . .	29
3.1.2	ROMS sub-tidal correction . . . . .	31
3.1.3	Water level over marsh platform . . . . .	34
3.2	Model validation . . . . .	35
<b>4</b>	<b>FVCOM sediment transport model (3D)</b>	<b>45</b>
4.1	Governing equations . . . . .	45

4.2	Model forcing and sediment parameters . . . . .	46
<b>5</b>	<b>Wetland morphology scenarios and net transport</b>	<b>48</b>
5.1	Simulations of scenarios based on altered marsh configurations . . . . .	51
5.1.1	Baseline conditions. . . . .	51
5.1.2	Scenario 1: Reduced channel depth and closure of Sluice Ditch . . . . .	55
5.1.3	Scenario 2: Reduced channel depth with Sluice Ditch open . . . . .	63
5.1.4	Scenario 3: Future opening of a connection between Duck Creek and Delaware Bay . . . . .	66
5.2	Erosion and net sediment transport . . . . .	66
<b>6</b>	<b>Wind waves on the Money Marsh mudflat</b>	<b>78</b>
6.1	Instrument location . . . . .	79
6.2	Data processing and extraction of wave signal . . . . .	79
6.2.1	Pressure to surface conversion . . . . .	83
6.3	Wave data analysis . . . . .	87
6.4	Spectral wave model SWAN . . . . .	92
6.4.1	Model background . . . . .	92
6.4.2	Unstructured grid for the mudflat . . . . .	93
6.4.3	SWAN model validation with the field data . . . . .	94

6.5	Analytic estimates of fetch limited waves . . . . .	105
6.5.1	Methodology . . . . .	105
6.5.2	Fetch limited wave growth vs SWAN . . . . .	107
<b>7</b>	<b>Conclusions</b>	<b>110</b>

## List of Figures

1	The geographic location of the Bombay Hook National Wildlife Refuge and estimated historic salt marsh loss in the area collected from McDowell & Sommerfield (2016). Red color shows the area already eroded. . . . .	3
2	(left) Bombay Hook National Wildlife Refuge, outlined in red. (right) Location in mid-Atlantic region. . . . .	6
3	DEM data set derived from the NOAA 2011 LiDAR survey is shown using black dashed line. The remaining topography of the domain is taken from a DEM prepared using the DNREC 2007 survey. The merged DEM represents the entire BHNWR area used for hydrodynamic modeling. Elevation information shown on the left side is measured from NAVD88 vertical reference level (in meters). . . . .	9
4	DEM data set derived from the USGS 2014 LiDAR survey for the entire BHNWR area. Elevation information shown on the left side is measured from NAVD88 vertical reference level (in meters). The red zone showing higher elevation is outside of our area interest and we neglected this portion for any further analysis. . . . .	10
5	Comparison between marsh elevation extracted from the NOAA 2011 and USGS 2014 LiDAR data sets, a previous grid by Stammerman (2013) and true ground surface measured using RTK GPS. The ground surface elevation was measured following a transect and we used the transect points for LiDAR accuracy check. Elevation information shown here is referenced to NAVD88 vertical datum (in meters). . . . .	11

6	BHNWR; (Upper Right) Ground truth survey; marsh (red); and fresh water impoundment (yellow) (A) Corresponding elevations extracted from LiDAR and survey data along a sample transect. . . . .	17
7	Optimization of Low-Bin bias correction technique. . . . .	18
8	Delaware community distribution. . . . .	19
9	RTK survey along a transect and corresponding elevation from 3 Lidar data sets (NAVD88) in upper panel and statistics in lower subplots: USGS 2014 (left), NOAA 2011 (center) and NOAA 2014 (right) . . . . .	20
10	Vegetation species distribution. . . . .	21
11	schematic view of Artificial Neural Network Algorithm . . . . .	21
12	Vegetation bias correction via ANN using 70% for training, 15 % validation and 15 % for test . . . . .	22
13	Unstructured grid domain used for the hydrodynamic and sediment transport study in BHNWR. The colorbar on the right represents the topo-bathymetry (in meters) referenced to NAVD88 vertical level. The forcing boundaries are the transects across the bay at the northern and southern limits of the grid. .	24
14	Higher resolution representation of the BHNWR channels and mudflats. The contour label on the right represents the topo-bathymetry (in meters) referenced to NAVD88 vertical level. Locations of four tide gauges inside BHNWR, used for model validation, are indicated. . . . .	25

15	Unstructured grid model FVCOM and structured grid model ROMS domains covering the entire Delaware Bay and estuary. Color label on the right side represents depth (in meters, from NAVD88 vertical reference level). . . . .	30
16	Unstructured grid model FVCOM (left subplot, red surface) and structured grid model ROMS (left subplot, blue surface) direct nesting at the common boundary. Variables at the unstructured grid boundary nodes and cells are extracted from overlapped structured grid. . . . .	31
17	An illustration showing the correction sub-tidal signals from ROMS results. The top subplot shows surface elevation comparison between ROMS and in-situ data from a NOAA tide gauge (at Ship John Shoal, Delaware Bay) during September 15 to October 15, 2015. Surface elevation was separated into harmonics and sub-tidal (second and third subplot) using t-tide. Finally, the corrected surface elevation is generated from superimposed ROMS harmonics and in-situ sub-tidal (bottom subplot). . . . .	33
18	Water level data recorded using HOBO pressure gauge at six locations on the BHNWR marsh platform. The Dock tide gauge shows the water level variation in Leipsic River. The geographic locations of the HOBO gauges are shown in Figure 24. . . . .	34
19	Comparison between FVCOM model (in blue) and in-situ (in red) water surface elevation during February, 2012 at different tide gauge locations in the BHNWR (in meters, from NAVD88 vertical reference level) . . . . .	36

20	Comparison between ROMS (in black), FVCOM (in blue) and in-situ (in red) water surface elevation during Hurricane Sandy, 2012 at different tide gauge locations in the Delaware Bay (in meters, from NAVD88 vertical reference level) . . . . .	37
21	Comparison between FVCOM (in black) and in-situ (in red) water surface elevation during Hurricane Sandy, 2012 at different tide gauge locations in the BHNWR (in meters, from NAVD88 vertical reference level) . . . . .	38
22	A snapshot of model surface elevation during a low tide and artificial ponding on the marsh platform. The colorbar on the right side represents water surface elevation (in meters, from NAVD88 vertical reference level) . . . . .	40
23	(a) Geographic representation of Bombay Hook wetland and Delaware Bay area separated into land (in blue) and water surface (in yellow) (b) Total volume of water going in and out of the system (top subplot), volume exchange in the channels (middle subplot) and volume exchange over marsh platforms (bottom subplot) . . . . .	41
24	Comparison between FVCOM model (in blue) and in-situ (in red) water surface elevation during September storm, 2015 at different tide gauge locations in the Bombay Hook area (in meters, from NAVD88 vertical reference level). . . . .	42
25	(a) Geographic location of deployed HOBO gauges in the Bombay Hook area (b) Comparison between FVCOM model (in blue) and in-situ (in red) water surface elevation during September storm, 2015 at different HOBO gauge locations (in meters, from NAVD88 vertical reference level) . . . . .	43

26	(a) Geographic location of deployed ADCP in Duck Creek (b) Comparison between FVCOM model (in blue) and aquadopp depth-averaged current data (in red) collected from Duck Creek, Bombay Hook during May, 2015 . . . . .	44
27	Leipsic River, Simon River, Sluice Ditch/Duck Creek and Woodland Beach inlets that connect BHNWR wetland system with the Delaware estuary and Bay. The total volume and sediment flux going in/out of the system are estimated later using these four inlets. . . . .	49
28	A critical location close to Leipsic River where an interior pool in the marsh platform is rapidly growing from inside and also the shoreline being eroded due to wind waves. This could possibly end up merging both the interior channel, Duck Creek and the Bay, creating a new inlet for the wetland. . . . .	50

29	<p>Total volume flux (in <math>\text{m}^3/\text{s}</math>) going in/out of BHNWR for different morphological scenarios. First subplot shows total flux for the entire spring-neap cycle used for model run (here, positive flux represents going out from the wetland, negative represents going in). The second and third subplot represents total flux magnitude separated into a spring and neap tidal cycle respectively (label provided on the right side). Surface elevation from a Leipsic River inlet model grid point (referenced to NAVD88, in meters) is shown with the solid black line (label provided on the left side). Flux magnitude and surface elevation are plotted together to identify the asymmetry during flood and ebb tide. <b>[legend:</b> depth 5m + wo SD: all channel depth goes up to 5 m and no Sluice Ditch, depth 5m + w SD: depth kept to 5 m and we have Sluice Ditch, org bathy: present grid bathymetry, org bathy + opening: present grid bathymetry with a new inlet, no Marsh: marsh surface is elevated by 2 m and kept above the tidal range]</p>	53
30	<p>Tide averaged volume flux (in <math>\text{m}^3/\text{s}</math>) going in/out of BHNWR for different morphological scenarios. The wave averaging is done by applying zero-upcrossing method on the surface elevation data from Leipsic River inlet model grid point. Total averaged flux is not exactly zero due to approximate estimation using transects; however, it is more or less than 1% of the peak flux magnitude of almost <math>1250 \text{ m}^3/\text{s}</math> during spring and <math>1000 \text{ m}^3/\text{s}</math> during neap tide. Detailed description about the figure legend is given in Figure 29.</p>	54

31	Stage/discharge relationship during a spring tide at the four inlets (Leipsic River, Woodland Beach, Sluice Ditch and Simon River) of BHNWR with different morphology scenarios. Here, positive flux represents going out from the wetland and negative represents going in. Detailed description about the figure legend is given in Figure 29. . . . .	57
32	Along channel velocity and volume flux (in m <sup>3</sup> /s) going in/out through Leipsic River inlet for different morphological scenarios. First subplot shows along channel velocity magnitude at the middle of the inlet during a spring tide and the second subplot represents the corresponding volume flux through the entire inlet. Remaining third and fourth subplot displays similar velocity and flux magnitude during a neap tide. Surface elevation from a Leipsic River inlet model grid point (referenced to NAVD88, in meters) is shown with the solid black line (label provided on the left side). Velocity and flux magnitude, and surface elevation are plotted together to identify the asymmetry during flood and ebb tide. Detailed description about the figure legend is given in Figure 29. . . . .	58
33	Stage/discharge relationship during a neap tide at the four inlets (Leipsic River, Woodland Beach, Sluice Ditch and Simon River) of BHNWR with different morphology scenarios. Here, positive flux represents going out from the wetland and negative represents going in. Detailed description about the figure legend is given in Figure 29. . . . .	59

34	<p>Along channel velocity and volume flux (in m<sup>3</sup>/s) going in/out through Sluice Ditch inlet for different morphological scenarios. First subplot shows along channel velocity magnitude at the middle of the inlet during a spring tide and the second subplot represents the corresponding volume flux through the entire inlet. Remaining third and fourth subplot displays similar velocity and flux magnitude during a neap tide. Surface elevation from a Sluice Ditch inlet model grid point (referenced to NAVD88, in meters) is shown with the solid black line (label provided on the left side). Velocity and flux magnitude, and surface elevation are plotted together to identify the asymmetry during flood and ebb tide. Detailed description about the figure legend is given in Figure 29. . . . .</p>	60
35	<p>Along channel velocity and volume flux (in m<sup>3</sup>/s) going in/out through Simon River inlet for different morphological scenarios. First subplot shows along channel velocity magnitude at the middle of the inlet during a spring tide and the second subplot represents the corresponding volume flux through the entire inlet. Remaining third and fourth subplot displays similar velocity and flux magnitude during a neap tide. Surface elevation from a Simon River inlet model grid point (referenced to NAVD88, in meters) is shown with the solid black line (label provided on the left side). Velocity and flux magnitude, and surface elevation are plotted together to identify the asymmetry during flood and ebb tide. Detailed description about the figure legend is given in Figure 29. . . . .</p>	61

36	Along channel velocity and volume flux (in m <sup>3</sup> /s) going in/out through Woodland Beach inlet for different morphological scenarios. First subplot shows along channel velocity magnitude at the middle of the inlet during a spring tide and the second subplot represents the corresponding volume flux through the entire inlet. Remaining third and fourth subplot displays similar velocity and flux magnitude during a neap tide. Surface elevation from a Woodland Beach inlet model grid point (referenced to NAVD88, in meters) is shown with the solid black line (label provided on the left side). Velocity and flux magnitude, and surface elevation are plotted together to identify the asymmetry during flood and ebb tide. Detailed description about the figure legend is given in Figure 29. . . . .	62
37	Changes in the tidal range (referenced to NAVD88, in meters) in BHNWR due to different morphological scenarios. . . . .	64
38	Changes in the maximum velocity magnitude (in m/s) in BHNWR due to different morphological scenarios. . . . .	65
39	Total volume flux (in m <sup>3</sup> /s) through each inlet in scenario 3, with a new entrance on Duck Creek. . . . .	67
40	Centerline velocity (m/s) in each inlet in scenario 3, with a new entrance on Duck Creek. . . . .	68

41	Total sediment flux (in kg/s) going in/out of BHNWR for different morphological scenarios. First subplot shows total flux for the entire spring-neap cycle used for model run (here, positive flux represents going out from the wetland, negative represents going in). The second and third subplot represents total flux magnitude separated into a spring and neap tidal cycle respectively (label provided on the right side). Surface elevation from a Leipsic River inlet model grid point (referenced to NAVD88, in meters) is shown with the solid black line (label provided on the left side). Flux magnitude and surface elevation are plotted together to identify the asymmetry during flood and ebb tide. . . .	70
42	Tide averaged sediment flux/residual transport (in kg/s) going in/out of BHNWR for different morphological scenarios. The wave averaging is done by applying zero-upcrossing method on the surface elevation data from Leipsic River inlet model grid point. Detailed description about the figure legend is given in Figure ?? . . . . .	71
43	Changes in the maximum sediment concentration (in g/L) in BHNWR due to different morphological scenarios. . . . .	72
44	Total sediment flux (in kg/s) during spring and neap tide conditions in the Leipsic River for each of the scenarios considered. . . . .	73
45	Total sediment flux (in kg/s) during spring and neap tide conditions in Sluice Ditch for each of the scenarios considered. . . . .	74
46	Total sediment flux (in kg/s) during spring and neap tide conditions in the Simon River for each of the scenarios considered. . . . .	75

47	Total sediment flux (in kg/s) during spring and neap tide conditions in the Woodland Beach entrance for each of the scenarios considered. . . . .	76
48	Sediment flux (in kg/s) during spring and neap tide conditions in the each entrance for scenario 3. . . . .	77
49	Pressure gauges in the tidal flat . . . . .	80
50	Barometric pressure and raw pressure data (dBar) collected from the RBR gauges . . . . .	81
51	Pressure data (dBar) collected from the gauge excluding barometric pressure. First subplot represents the pressure data for long waves and the last two illustrates wind waves at different locations . . . . .	82
52	(a) Pressure response factor $K_p$ at RBR1 location during a storm event & high tide (b) same storm event & low tide. Here, the dashed line represents maximum frequency taken into account based on the pressure response factor value 0.01. . . . .	85
53	a) Pressure response factor $K_p$ at RBR2 location during high tide (b) during low tide (c) during a storm event & high tide (d) same storm event & low tide	86
54	Pressure head and the surface elevation (in meters) using $K_p$ . . . . .	90
55	Smoothed spectral estimate obtained using Welch's method at RBR1 for pressure head (in blue) and corrected surface elevation (in red). Tail of the spectrum is reconstructed following the shape of a TMA spectrum. . . . .	91
56	(a) Unstructured grid resolution (b) Topo-bathymetry of the unstructured grid (in meters) from NAVD88 vertical reference level . . . . .	96

57	(a)(b) Significant wave height (in meters) and peak wave period (in seconds) for the high resolution structured grid (c)(d) Significant wave height (in meters) and peak wave period (in seconds) for the unstructured grid . . . . .	97
58	(a) Comparison between structured and unstructured grid significant wave height (in meters). (b) Comparison between structured and unstructured grid peak wave period (in seconds). . . . .	98
59	Wind rose diagram and wind speed at 10 m elevation (in m/s) during a storm (September 25 to October 8, 2015) at Ship John Shoal, NJ . . . . .	99
60	Water level data from Leatherbery tide gauge (in meters, referenced from NAVD88 vertical datum) during a storm (September 25 to October 8, 2015) .	100
61	Spatial representation of the vegetation coverage around money marsh tidal flat . . . . .	100
62	Comparison between SWAN generated and measured significant wave height at RBR1 (in meters) . . . . .	101
63	Comparison between SWAN generated and measured peak period at RBR1 (in seconds) . . . . .	102
64	Comparison between SWAN generated and measured significant wave height at RBR2 (in meters) . . . . .	103
65	Comparison between SWAN generated and measured peak period at RBR2 (in seconds) . . . . .	104
66	Transects and wind directions to compute wave growth using non-dimensional fetch distance and depth . . . . .	107

67	Comparison of depth (in meters) from NAVD88 vertical reference level, significant wave height (in meters) and peak wave period (in seconds) for Fetch-wave and SWAN at Transect 1 . . . . .	108
68	Comparison of depth (in meters) from NAVD88 vertical reference level, significant wave height (in meters) and peak wave period (in seconds) for Fetch-wave and SWAN at Transect 2 . . . . .	109

# 1 Introduction

The Bombay Hook National Wildlife Refuge (BHNWR) protects one of the largest remaining expanses of tidal wetlands in the mid-Atlantic region. The refuge salt marsh is unique because it is minimally altered compared to other tidal marshes in Delaware. Although channels have been constructed during historical times, there is very little grid ditching or open marsh water management (OMWM). It serves as an important link in the Atlantic migration corridor, providing refuge and breeding grounds for migrating shorebirds, waterfowl, and other wildlife. The marshes of BHNWR provide a buffer to adjacent communities and large areas of highly productive farmland. The refuge itself is a key component of the local economy, its combination of salt marsh and freshwater impoundments distinguishing it nationally as a top birdwatching location. Economic studies have found that the refuge accounts for millions of dollars of expenditures each year in the surrounding area, as visitors come primarily from out of state. Furthermore, it is estimated that a functioning salt marsh provides nearly 8,000 /acre/year to the surrounding communities in ecosystem services alone, such as clean water, fisheries habitat, and carbon sequestration, which amounts to \$100M/year for BHNWR marshes (Kauffman *et al.*, 2011).

Bombay Hook has experienced substantial loss of salt marsh in recent decades. During a large storm in May 2008, the refuge's wildlife drive was breached by water for the first time in the history of refuge management, illustrating the increasing vulnerability of the wetlands and freshwater impoundments to storms and sea level rise. Marsh loss is believed to be due to a combination of factors such as past marsh alterations (ditches, channels) and snow goose herbivory, further complicated by sea level rise. Little is known about the mechanisms of marsh loss as related to tidal hydrology and wind-wave dynamics, important controls on sediment transport and marsh accretion. What data has been collected on

the refuge suggests that the marsh hydrology may be out of balance due to significant increases in open water area. The United States Fish and Wildlife Service (USFWS) needs to build on existing science to gain a better understanding of the relationship between the morphology and physical dynamics of the wetlands to determine if there are management or restoration actions that could mitigate marsh loss and improve its resiliency and viability in the long term. This information will be coupled with the refuge's ongoing biological monitoring efforts, which are conducted in conjunction with other refuges and partners, and thus ensure science-based refuge management. Preliminary hydrodynamic modeling by Drexel University has shown that artificial channels created in the refuge may have influenced the natural wetland hydrology and potentially sediment transport with implications to marsh accretion ([Stammerman, 2013](#)).

The sustainability of Mid-Atlantic tidal wetlands was recently addressed as part of a comprehensive report by the U.S. Climate Change Science Program. The authors identified the general lack of information on local rates of marsh accretion as an obstacle in assessing wetland vulnerabilities to sea level rise and storm surge, recommending that “regional or national scale assessments should not be used to develop local management plans where local accretionary dynamics may override regional controls on wetland vertical development” ([Cahoon \*et al.\*, 2009](#)). Accretion rates are used by wetland scientists and managers to assess whether the marsh platform is capable of building upward in advance of rising sea level. The authors encouraged coastal managers to acquire data on environmental stressors, accretionary processes, and geomorphic setting, as a basis for developing local management plans, which often involve models of dynamic processes such tides, wind waves and storm surge.

The absolute elevation of the marsh surface is controlled by rates of vertical accretion and land subsidence relative to sea level, the balance of which sets the position of the marsh

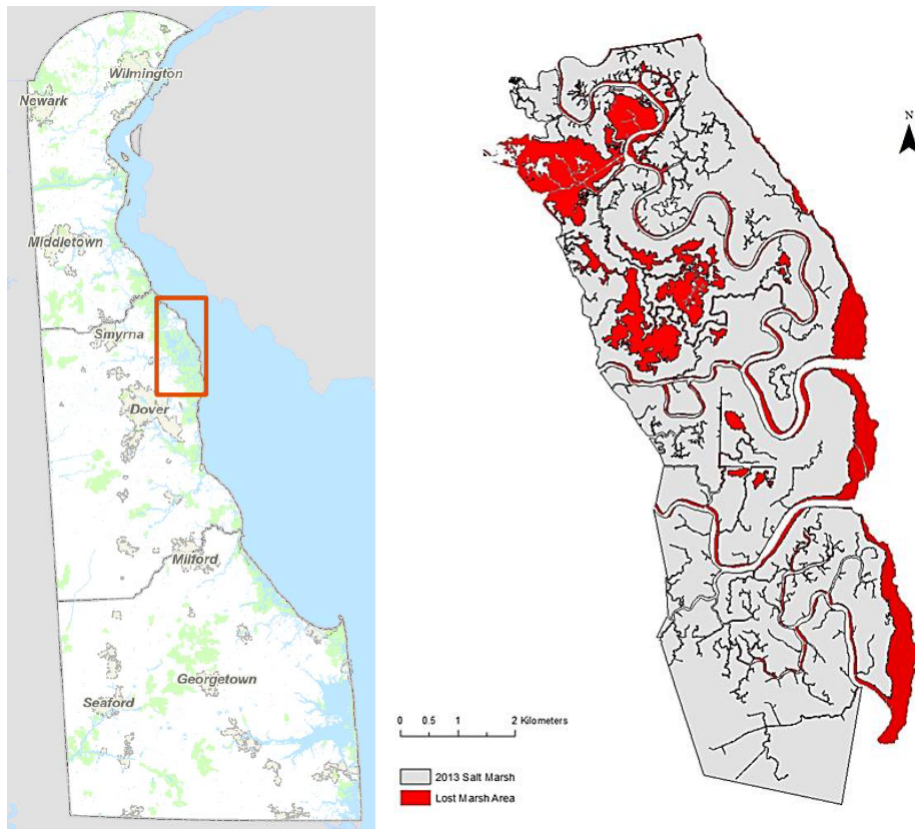


Figure 1: The geographic location of the Bombay Hook National Wildlife Refuge and estimated historic salt marsh loss in the area collected from [McDowell & Sommerfield \(2016\)](#). Red color shows the area already eroded.

platform within the tidal frame. The rate of accretion is driven by physical and biotic processes that contribute soil volume, for example, production of below-ground biomass and tidal sedimentation of organic and mineral matter ([Else-Quirk \*et al.\*, 2011](#)). Because the elevation of the marsh surface relative to sea level determines patterns of tidal inundation and hydroperiod, the rate of accretion influences wetland morphology, hydrodynamics, and sediment transport through a feedback loop. Hence, establishing the accretionary status of marshland is fundamental to wetland resiliency planning. Ongoing research has shown that, whereas most salt marshes of the Delaware Estuary region are accreting in advance of local

sea level rise, some are deficient and in jeopardy of drowning should the rate of sea level rise accelerate (Sommerfield & Velinsky, 2010). However, the accretionary status of BHNWR salt marsh is unknown.

A great deal of scientific understanding has been gained by developing idealized model approaches to wetland processes. These models have illuminated the coupled interplay of sediment supply, vegetation, and environmental stress such as waves in determining the growth and maintenance of marsh surfaces, or in leading to their failure and transition to tidal flats (see Fagherazzi *et al.* (2012) for a comprehensive overview of work carried out to date). Knowledge of this balance provides a context for understanding, in a general sense, whether existing sediment supply from inorganic or organic sources would be likely to be adequate for maintaining the health and extent of marsh surfaces in the presence of accelerated sea level rise. However, actual tidal wetland environments such as Bombay Hook NWR can be immensely complex systems, with large numbers of hydrologic interconnections, and the sole utilization of simplified models would not provide a means for understanding site-specific responses or apparent spatial variability across the wetland. Simplified models are also not directly useful in evaluating wetland response to possible remedial alterations aimed at changing flow patterns, tidal range or sediment supply using site-specific modifications.

In light of the importance of the BHNWR to both the ecology and economy of the Delaware coastal environment, and of the need to obtain a better functional understanding and predictive capability for its complex biogeophysical structure, this study has developed a comprehensive, three dimensional model system for the BHNWR tidal wetland environment, and has conducted a measurement program to collect a comprehensive data set needed for verification of the model. The aim of the model is to provide a robust means for evaluating the present tidal regime in the wetland, for evaluating potential remedial steps leading to a healthier marsh environment, and ultimately for making predictions of the long-term

sustainability of the marsh environments within the system.

In this report, we describe the development of model grid and boundary forcing in section 2. A 2D, depth integrated version of the code, which is useful for describing the basic aspects of tidal circulation, is described and validated in section 3. Section 4 describes the extension to 3D and incorporation of sediment transport capabilities, for which we do not as yet have an adequate set of data for testing purposes. Section 5 shows calculations for a range of hypothetical scenarios, illustrating the effects of various change on tidal circulation and sediment transport. Section 6 describes work that has been done to assess wave climate and its contribution to shoreline erosion in open mud flat areas within BHNWR. Conclusions and observations on needed work are provided in section 7.

## **1.1 Study area**

The BHNWR consists of about 16,000 acres located in Kent County, Delaware near the towns of Smyrna and Dover, along the western shore of the Delaware Bay. It is managed by the U.S. Fish and Wildlife Service (USFWS) as part of the Coastal Delaware NWR Complex, along with Prime Hook NWR located in southern Delaware. The refuge was established in 1937 under the authority of the Migratory Bird Conservation Act (16 U.S.C. 715-715r), "for use as an inviolate sanctuary, or for any other management purpose, for migratory birds." The refuge is about 16,000 acres and is composed of upland habitats, freshwater impoundments and 13,000 acres of tidal wetlands.

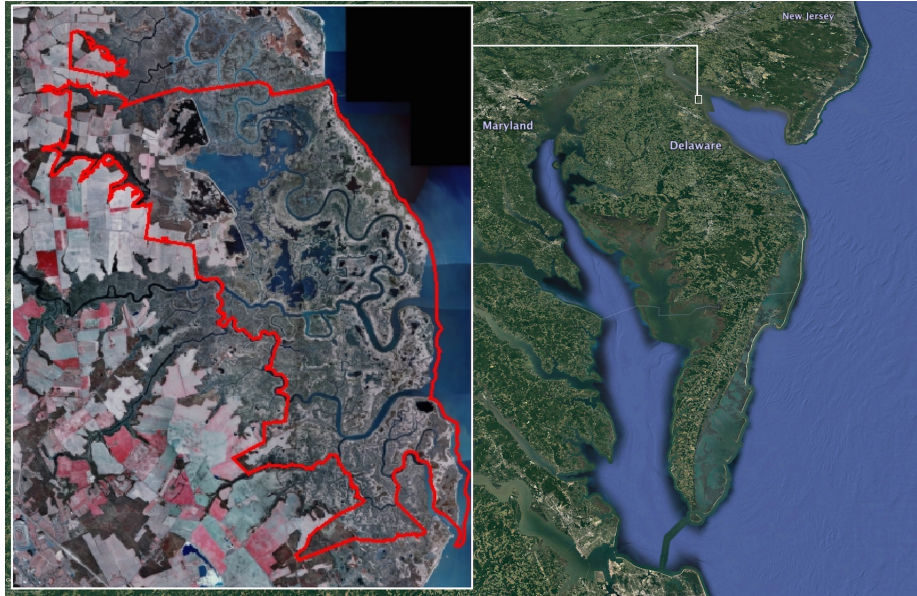


Figure 2: (left) Bombay Hook National Wildlife Refuge, outlined in red. (right) Location in mid-Atlantic region.

## 2 Model DEM and grid development

Accurate ground elevation is critical for assessing the health and stability of coastal salt marshes and for hydrodynamic modeling of wetland circulation patterns. Elevation of the marsh platform is used for mapping of potential inundation from relative sea-level rise, calculation of sediment deposition and accretion rates, vegetative species identification, and assessments of flood risk from coastal storms. Errors of a few centimeters in vertical elevation could cause inaccuracies that subsequently lead to biased evaluation of risk mapping, marsh productivity, flooding and draining behavior, and morphodynamics.

## 2.1 LiDAR data sets

Light Detection and Ranging (LiDAR) is a popular and advanced growing technology for observing vertical elevations with high spatial and vertical accuracy for large areas very quickly. The high vertical accuracy of LiDAR data sets to calculate the bare-earth ground surface has been proved for unvegetated areas. However, in highly vegetated areas like tidal marshlands, the vertical bias of the bare-earth surface increases due to the inability of LiDAR to reliably penetrate dense vegetation canopies.

We have utilized three high resolution LiDAR data sets, processed to a regular grid with 1 m in resolution, along with an earlier data set spanning the state of Delaware. The processed LiDAR DEM's include

- a 2007 data set (DNREC, 2007), referred to as the DNREC 2007 data.  
([https://coast.noaa.gov/htdata/lidar1\\_z/geoid12a/data/109/](https://coast.noaa.gov/htdata/lidar1_z/geoid12a/data/109/))
- a 2011 data set commissioned by the Delaware Department of Natural Resources and Environmental Control (DNREC) and collected by NOAA (Hund, 2013) and primarily covering wetland areas from BHNWR south to the St. Joans and Murderkill Rivers, referred to as the NOAA 2011 data.  
([https://coast.noaa.gov/htdata/lidar1\\_z/geoid12a /data/1172/2011\\_DNREc\\_BombayHook\\_metadata.html](https://coast.noaa.gov/htdata/lidar1_z/geoid12a/data/1172/2011_DNREc_BombayHook_metadata.html))
- a 2014 dataset collected by the U. S. Geological Survey (USGS) (USGS, 2014), referred to as the USGS 2014 data.  
([https://coast.noaa.gov/htdata/lidar1\\_z/geoid12b/data/4969/](https://coast.noaa.gov/htdata/lidar1_z/geoid12b/data/4969/))
- a dataset collected by NOAA (NOAA, 2016), referred to as the NOAA 2014 data.  
([https://coast.noaa.gov/htdata/lidar1\\_z/geoid12b/data/4800/](https://coast.noaa.gov/htdata/lidar1_z/geoid12b/data/4800/))

2014\_NGS\_postSandy\_topobathy\_metadata.html)

Figure 3 shows a map created by an overlay of the NOAA 2011 data onto the earlier DNREC 2007 data, which was used to create the earlier grid of Stammerman (2013). Figure 4 shows a DEM derived from the USGS 2014 survey. Each of these will be compared with ground truth survey data below and in section 2.2. This is done to represent the BHNWR marsh topography as accurately as possible for further modeling works.

The NOAA 2011 LiDAR data set has a vertical accuracy of 9 cm RMSE at flat non-vegetated areas and less than 15 cm for points falling in marshes (see <https://coast.noaa.gov/dataviewer/#/lidar/>). Meanwhile, the horizontal accuracy is kept below 50 cm RMSE. The horizontal and vertical datum of the DEM are assigned to Delaware State Plane using the North American Horizontal Datum of 1983 and the North American Vertical Datum of 1988 respectively, and the unit of measurement is in meters. For the USGS 2014 LiDAR data, the datums and unit of measurement are observed to be the same. The 95th percentile error for the vertical accuracy is approximately 15 cm for high grass, weeds and crops, and 12 cm for urban area. We compared the collected DEM's with surveyed marsh surface elevation at multiple locations in BHNWR to find the actual vegetation bias in them, as the LiDAR surveys were completed under different seasonal and tidal conditions. From Figure 5, we can see the vegetation bias at a transect location in BHNWR for both the NOAA 2011 and USGS 2014 DEM's, and a previous model grid. The NOAA 2011 data set has been identified as the one with least bias and has continued to be used as the basis for our modeling work with further vegetation correction (detailed description of the vegetation bias correction is given in section 2.2). The NOAA 2011 LiDAR survey was conducted for the large part of BHNWR and didn't cover the entire wetland. For a complete representation of BHNWR, we have merged the NOAA 2011 DEM with the DNREC 2007 state DEM as shown in Figure 2.

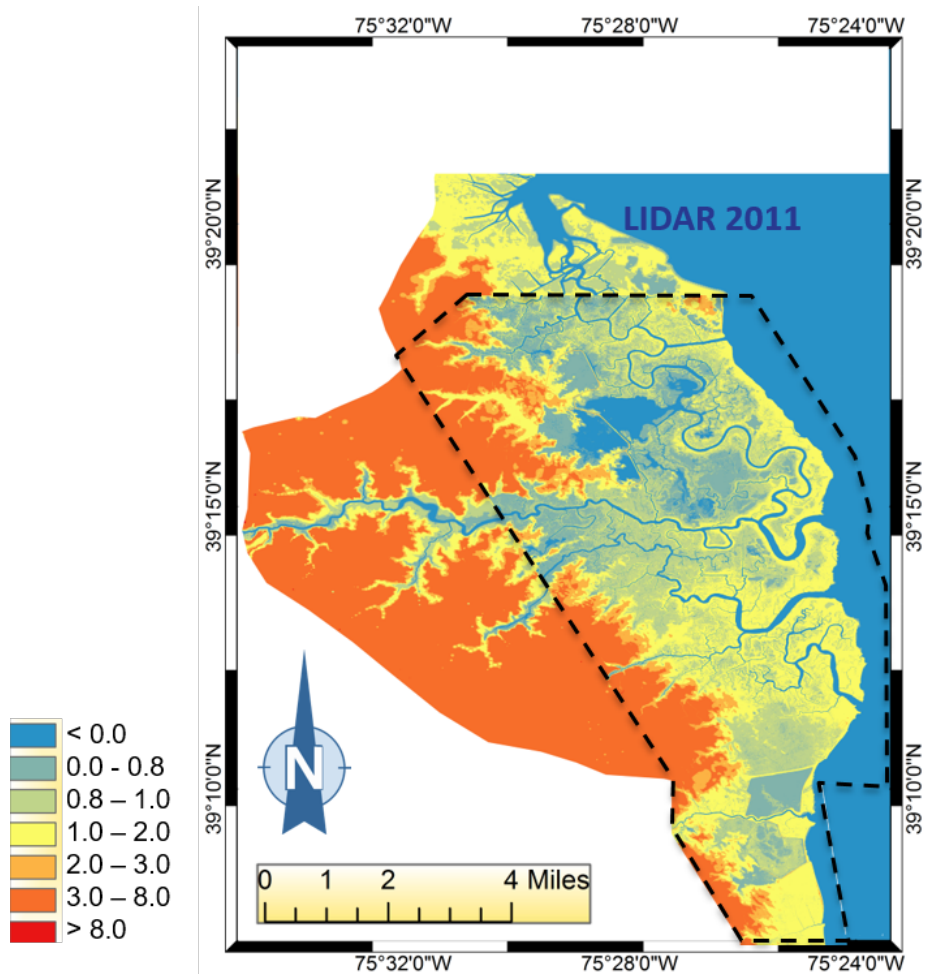


Figure 3: DEM data set derived from the NOAA 2011 LiDAR survey is shown using black dashed line. The remaining topography of the domain is taken from a DEM prepared using the DNREC 2007 survey. The merged DEM represents the entire BHNWR area used for hydrodynamic modeling. Elevation information shown on the left side is measured from NAVD88 vertical reference level (in meters).

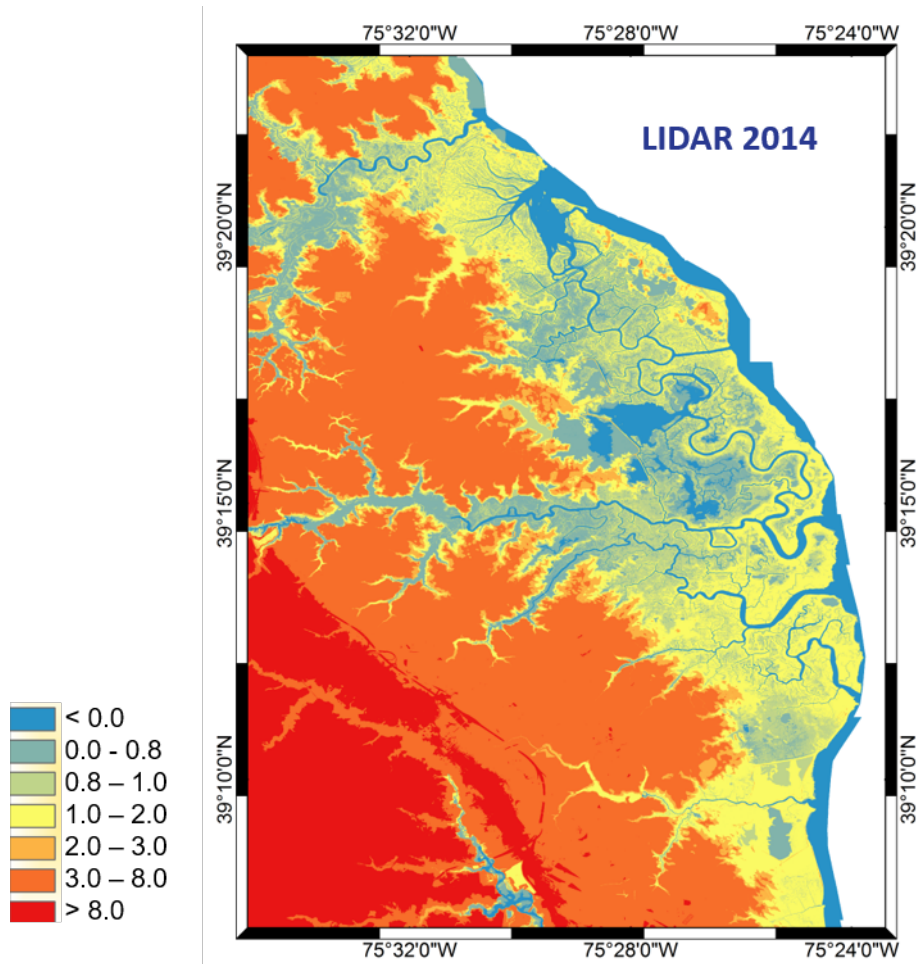


Figure 4: DEM data set derived from the USGS 2014 LiDAR survey for the entire BHNWR area. Elevation information shown on the left side is measured from NAVD88 vertical reference level (in meters). The red zone showing higher elevation is outside of our area interest and we neglected this portion for any further analysis.

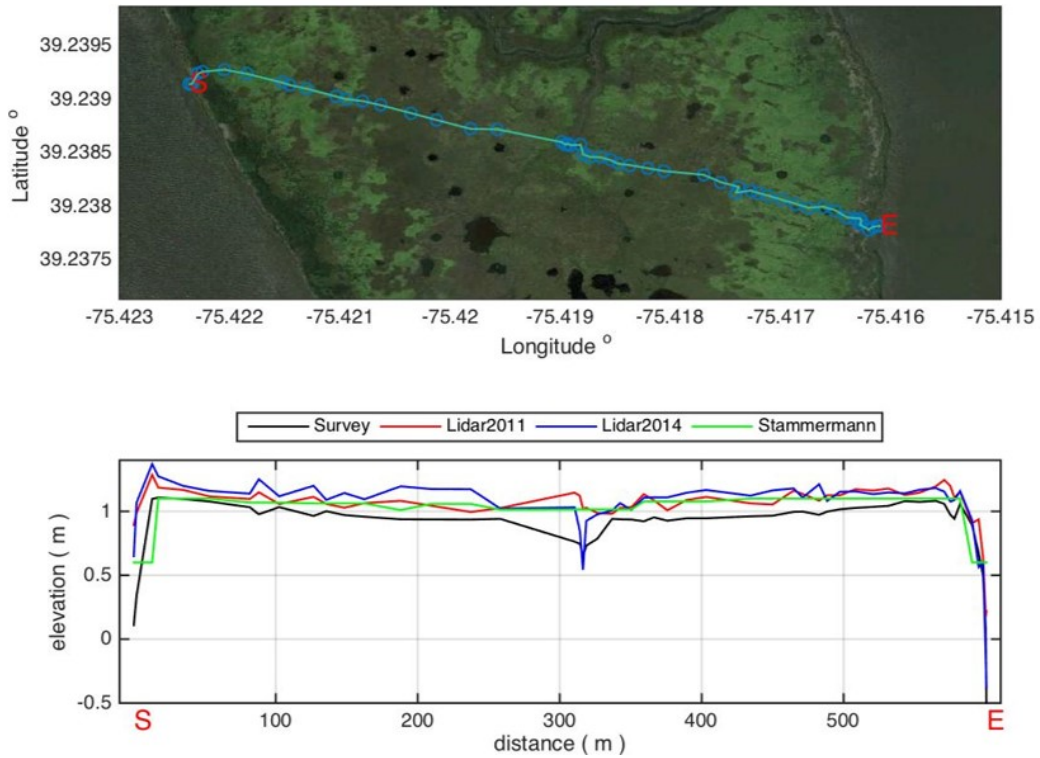


Figure 5: Comparison between marsh elevation extracted from the NOAA 2011 and USGS 2014 LiDAR data sets, a previous grid by [Stammerman \(2013\)](#) and true ground surface measured using RTK GPS. The ground surface elevation was measured following a transect and we used the transect points for LiDAR accuracy check. Elevation information shown here is referenced to NAVD88 vertical datum (in meters).

## 2.2 Vegetation bias correction

Light Detection and Ranging (LiDAR) is a popular and advanced growing technology for observing vertical elevations with high spatial and vertical accuracy for large areas very quickly (Figures 3 and 4). The high vertical accuracy of LiDAR data sets for determination of the bare-earth ground surface has been proven for unvegetated areas. However, in highly vegetated areas like tidal marshlands, the vertical bias of the bare-earth surface increases due to the inability of LiDAR to reliably penetrate dense vegetation canopies (Figure 5).

Accurate ground elevation is critical for assessing the health and stability of coastal salt marshes and for hydrodynamic modeling of wetland circulation patterns. Elevation of the marsh platform is used for mapping of potential inundation from relative sea-level rise, calculation of sediment deposition and accretion rates, vegetative species identification, and assessments of flood risk from coastal storms. Errors of a few centimeters in vertical elevation could cause inaccuracies that subsequently lead to biased evaluation of risk mapping, marsh productivity, flooding and draining behavior, and morphodynamics. In the present work, we have implemented two methodologies to decrease the LiDAR vertical bias of the bare-earth surface in a coastal salt marsh; the Minimum Bin Technique, and a method based on a trained Artificial Neural Network (ANN). Survey tracks for collection of ground truth data, and an example of elevations derived from a variety of sources along a sample track, are shown in Figure 6.

### 2.2.1 Minimum Bin Technique

The minimum bin technique picks the lowest point within a grid cell of size  $A$ , which is assigned as the grid or raster value. If the cell resolution is equal to DEM resolution, there is one point within the cell. For larger cell size, the number of points increases. In this

technique, the bin size should be optimized, therefore the best performance can be achieved where the min value is selected among an adequate number of points. The lowest elevation in a bin represents the bare earth where Lidar could penetrate and reach the bottom. In this study, we varied the cell size around control points and optimized bin size, as it is shown in Figure 7 where 4 m bin resolution leads to the lowest bias.

### 2.2.2 Artificial Neural Network

The ANN approach is a suitable candidate to address problems where the relationships among variables are complex and nonlinear. The behavior of an ANN is defined based on a training rule and determine the connection between variables by allocating weight ( $w_i$ ) and bias ( $b_i$ ) to each function. The ANN in this study is trained by existing vegetation maps, LiDAR intensity distribution, and multiple LiDAR digital elevation models (DEMs) acquired for BHNWR area on three separate occasions: topographic LiDAR in spring 2011 (NOA 2011), topographic LiDAR in winter 2014 (USGS 2014), and topo-bathymetric LiDAR by NOAA NGS also in winter 2014 (NOAA 2014). The statistics for each data set are shown in Figure 8. We selected the earliest high quality LiDAR dataset among others which covers the entire control points. Other input variables in the ANN include vegetation maps provided by the USFWS and National Wetlands Inventory (NWI), LiDAR intensity from the USGS 2014 LiDAR acquisition project, and multiple DEMs, each derived from high-quality LiDAR collected at Quality Level 2 or better. Tables 1 shows the number of surveyed points within 6 Delaware community classes together with LiDAR bias statistics. The percentage of each category is shown in the pie chart (Fig. 9). Vegetation species classification information for surveyed points are shown in Table 2 and Figure 10. We have trained, validated and tested the performance of the ANN using an extensive surveyed dataset collected over the marsh platform (Deb *et al.*, 2018). Ground truth is provided by a set of RTK survey points

Delaware community	n	MAE (m)	RMSE (m)	$\sigma$ (m)
(I) North Atlantic Low SaltMarsh	630	0.17	0.19	0.1
(II) Estuarine Coastal Polyhaline Water	48	0.22	0.25	0.11
(III) Atlantic Cordgrass Marsh	28	0.2	0.22	0.09
(IN) Irregularly Flooded Eastern Tidal Salt-Shrub	18	0.12	0.15	0.08
(V) North Atlantic High SaltMarsh	234	0.19	0.21	0.11
(VI) Reed Tidal Marsh	51	0.23	0.25	0.1
70 %	1010	0.18	0.2	0.1
Test - 30 %	437	0.07	0.09	0.09

Table 1: Delaware community statistics.

collected at numerous locations over the marsh platform, covering a variety of dominant vegetation types including *Spartina patens*, *Spartina alterniflora*, *Spartina cynosuroides*, *Scirpus robustus*, *Phragmites australis*, *Iva frutescens* and *Distichlis spicata*. The data set includes 1484 points over the saltwater marsh and in a fresh water impoundments. We have used Matlab software for programming Table 2.

There are uncertainties in the vegetation maps and missing information at some points, therefore vegetation bias correction based on one single vegetation map, as described in previous sections, is not an appropriate solution. Moreover, determination of multiple corrections based on different classification and maps with nonlinear relationship and weights is a difficult task. On the other hand, a well trained ANN has the capability of overcoming such difficulties and estimate the corrected values based on what it has as inputs (Abdolali *et al.*, 2016a).

Figure 11 shows a schematic view of ANN algorithm, while the top panel in Figure 12

Vegetation species	n	MAE (m)	RMSE (m)	$\sigma$ (m)
(I) <i>Spartina Alterniflora</i>	128	0.19	0.2	0.07
(II) <i>Spartina Alterniflora Tall</i>	71	0.22	0.24	0.15
(III) <i>Spartina Alterniflora Short</i>	245	0.21	0.23	0.08
(IV) <i>Spartina Cynosuroides</i>	93	0.25	0.26	0.07
(V) <i>Spartina Patens</i>	153	0.12	0.14	0.06
(VI) <i>Scirpus Robustus</i>	16	0.2	0.21	0.07
(VII) <i>Phragmites Australis</i>	26	0.18	0.19	0.08
(VIII) <i>Iva Frutescens</i>	8	0.10	0.12	0.05
(IX) <i>Distichlis Spicata</i>	96	0.11	0.13	0.06
(X) Bare	18	0.2	0.26	0.18
70 %	854	0.18	0.21	0.1
Test - 30 %	373	0.08	0.1	0.1

Table 2: Vegetation species statistics.

displays the relative amount of data points used for training, validation and testing of the ANN used here. The following list indicates the process used in training the ANN.

1. 70% of dataset is picked randomly for training.
2. Training data is classified for each class into each subcategory (i.e. Delaware Community, Vegetation species, LiDAR intensity, etc).
3. Correction coefficients for different sub-categories are determined (Mean Error).
4. Through an iterative procedure, the weight for each class is determined in order to obtain the minimum standard deviation and Mean Absolute Error.

5. The model is used to correct 15% of data for validation using different classes with different correction factor and weight.
6. Finally, the rest of data (15%) is corrected as a test.

The coefficient of determination  $R^2$ , the standard deviation  $\sigma$ , the root mean square error and the mean absolute error are the main criteria that are used to evaluate the ANN performance. Sensitivity analysis has been performed to ensure the efficiency of ANN as well as a comparison of the ANN to other correction techniques (i.e. vegetation type sensitive correction and lowest bin gridding). Results show that application of the ANN led to a reduction in vertical bias by almost 65 %. The ANN could efficiently decrease the mean absolute error from 20 cm to 8 cm ([Abdolali \*et al.\*, 2016a](#)).

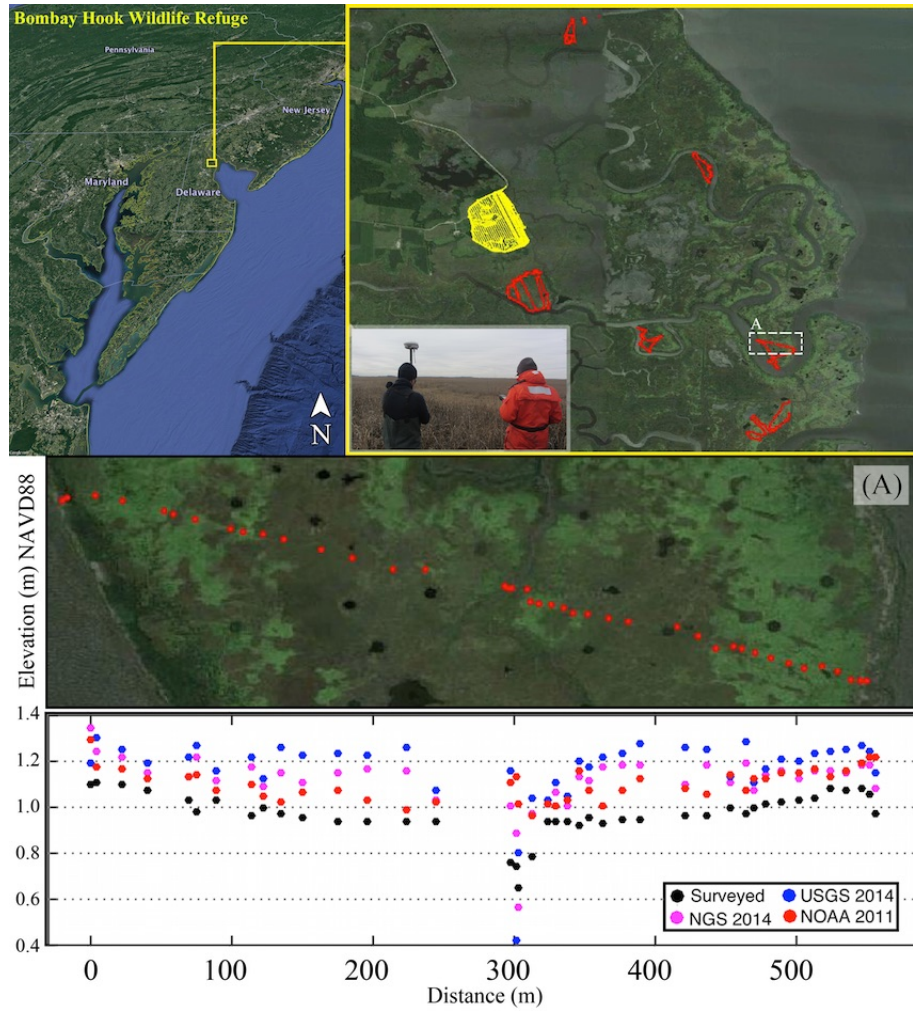


Figure 6: BHNWR; (Upper Right) Ground truth survey; marsh (red); and fresh water impoundment (yellow) (A) Corresponding elevations extracted from LiDAR and survey data along a sample transect.

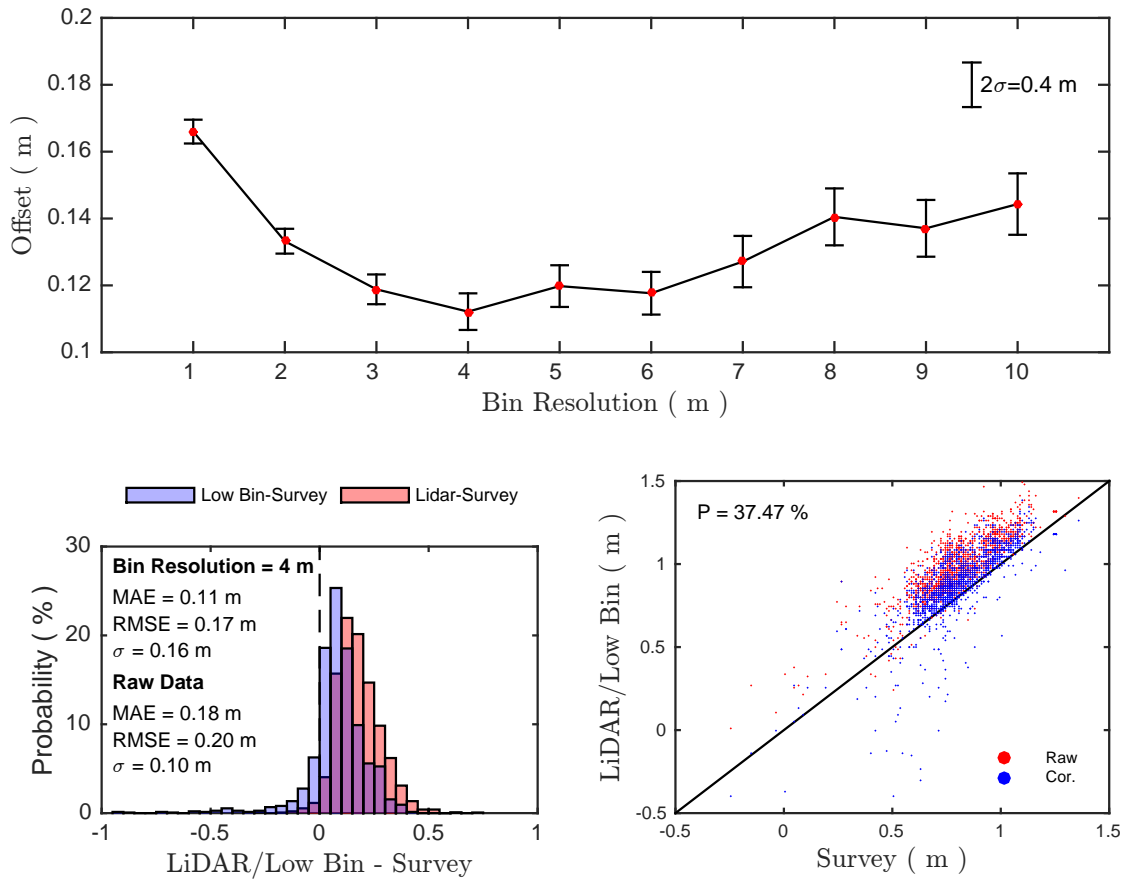


Figure 7: Optimization of Low-Bin bias correction technique.

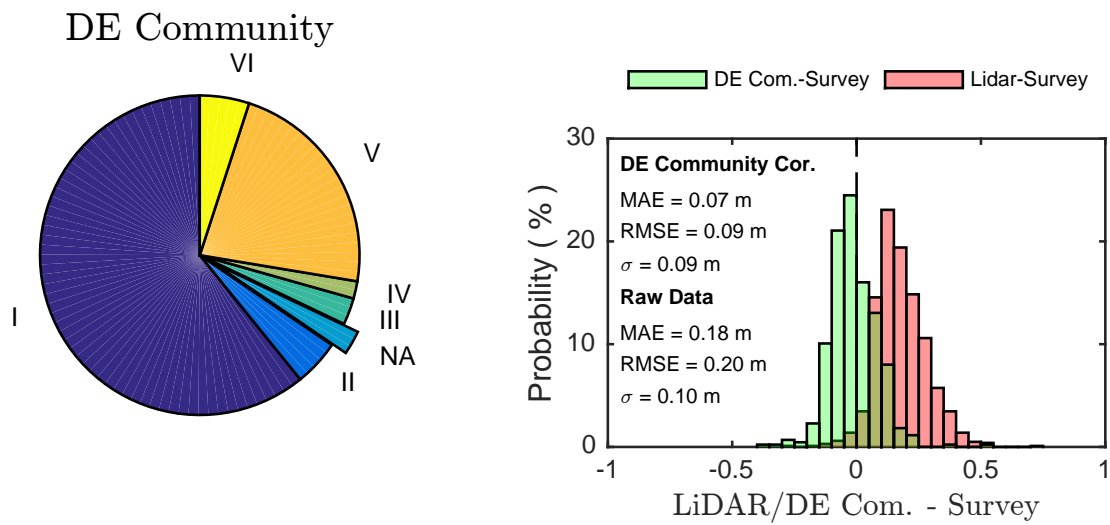


Figure 8: Delaware community distribution.

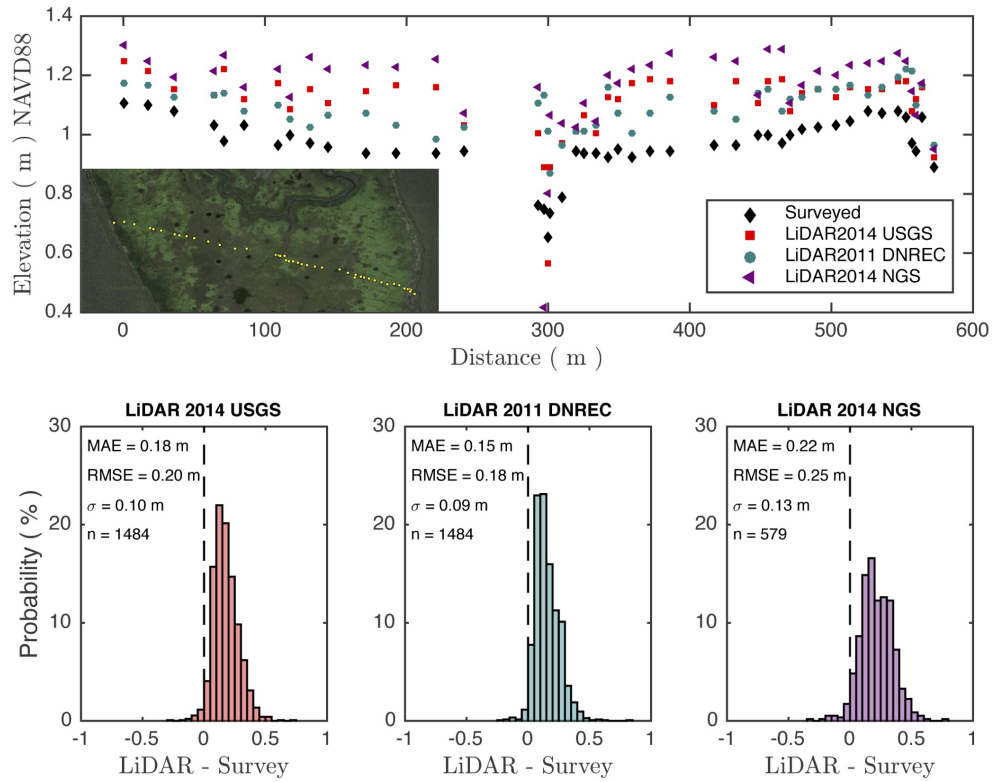


Figure 9: RTK survey along a transect and corresponding elevation from 3 Lidar data sets (NAVD88) in upper panel and statistics in lower subplots: USGS 2014 (left), NOAA 2011 (center) and NOAA 2014 (right)

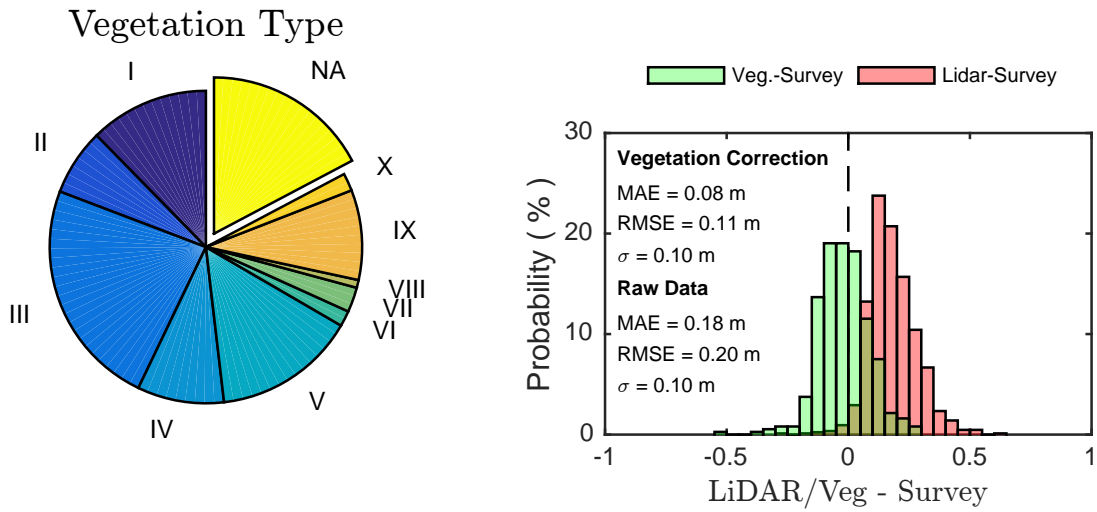


Figure 10: Vegetation species distribution.

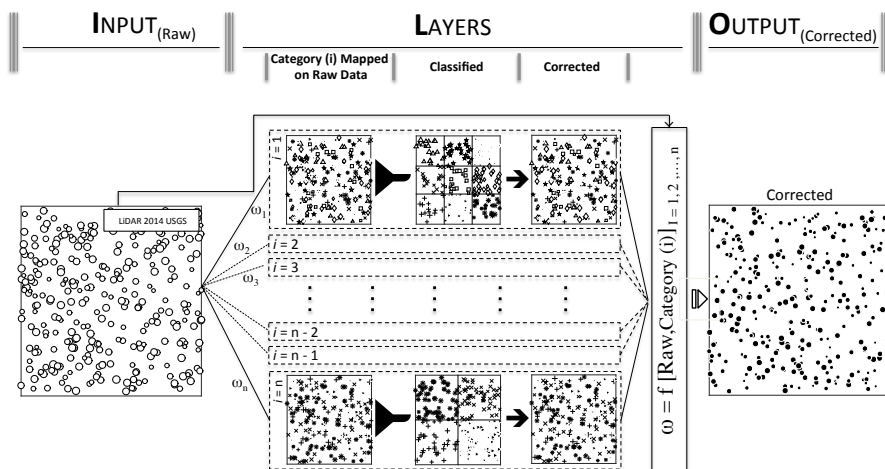


Figure 11: schematic view of Artificial Neural Network Algorithm

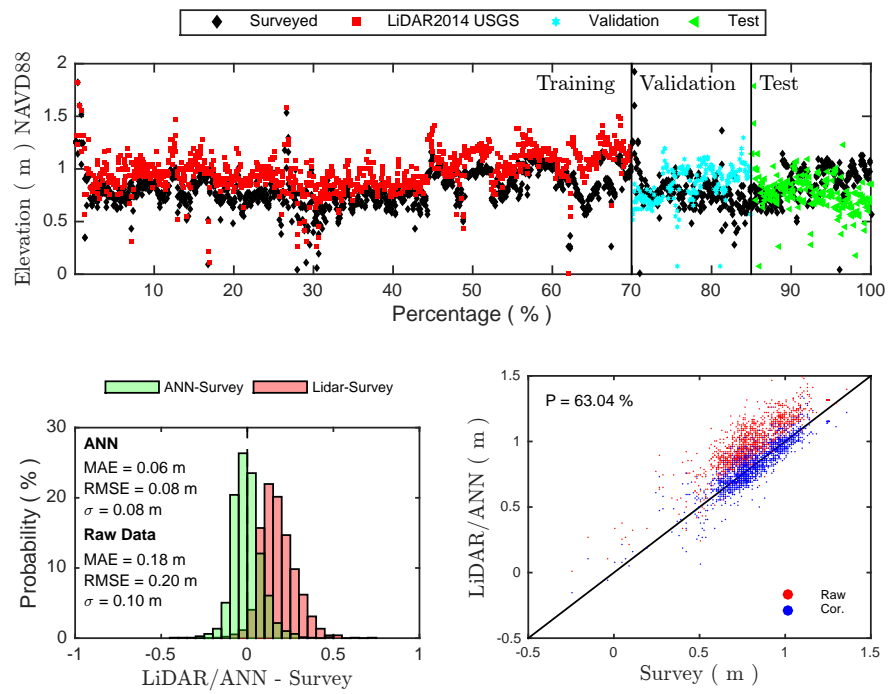


Figure 12: Vegetation bias correction via ANN using 70% for training, 15 % validation and 15 % for test

### 2.3 Unstructured grid development

We initially utilized an unstructured grid developed by [Stammerman \(2013\)](#) for a hydrodynamic study of the same area. Model grid domain shown in [Figure 13](#) covered the entire BHNWR wetland, and forcing boundaries are assigned on Delaware River in the northern side (upstream) and Delaware Bay in the southern side (downstream). The unstructured grid has almost 700,000 elements, with a finest grid resolution of about 3 m to resolve small tidal creeks and channels inside the wetland area, and dropping to up to 1 km in the Bay region. [Stammerman \(2013\)](#) used a mesh generation tool JANET for the unstructured grid development. JANET uses forcing polygons or break lines to enforce the alignment of elements along the lines and define grid resolution at the zones of interest. The detailed description of the mesh triangulation is given in [Stammerman \(2013\)](#). To represent channel bathymetry, channel cross-sections in BHNWR were surveyed using a handheld SONAR and referenced to the NAVD88 vertical datum. A total of 48 cross-sections and five mudflat transects were selected for the measurement. Surface elevation data were taken from the NOAA 2011 LiDAR survey, where available. The NOAA 2011 LiDAR data set did not cover the entire BHNWR, and the DNREC 2007 LiDAR is used to cover the remaining area.

In our study, we have updated the grid topo-bathymetry with the recent channel surveys and vegetation bias corrected LiDAR 2011 data mentioned at the previous data collection section. In the original grid, some of the artificially dredged interior channels which had been artificially dredged, such as the internal tidal creek that connects Money Marsh mudflat to Leipsic River, had small vertical walls at several locations throughout the channel, possibly due to grid resolution or interpolation error. They have been identified and modified by channel depth from both side of the wall. Similarly, there are few other interior creeks where we have assigned an average depth to improve the connectivity.

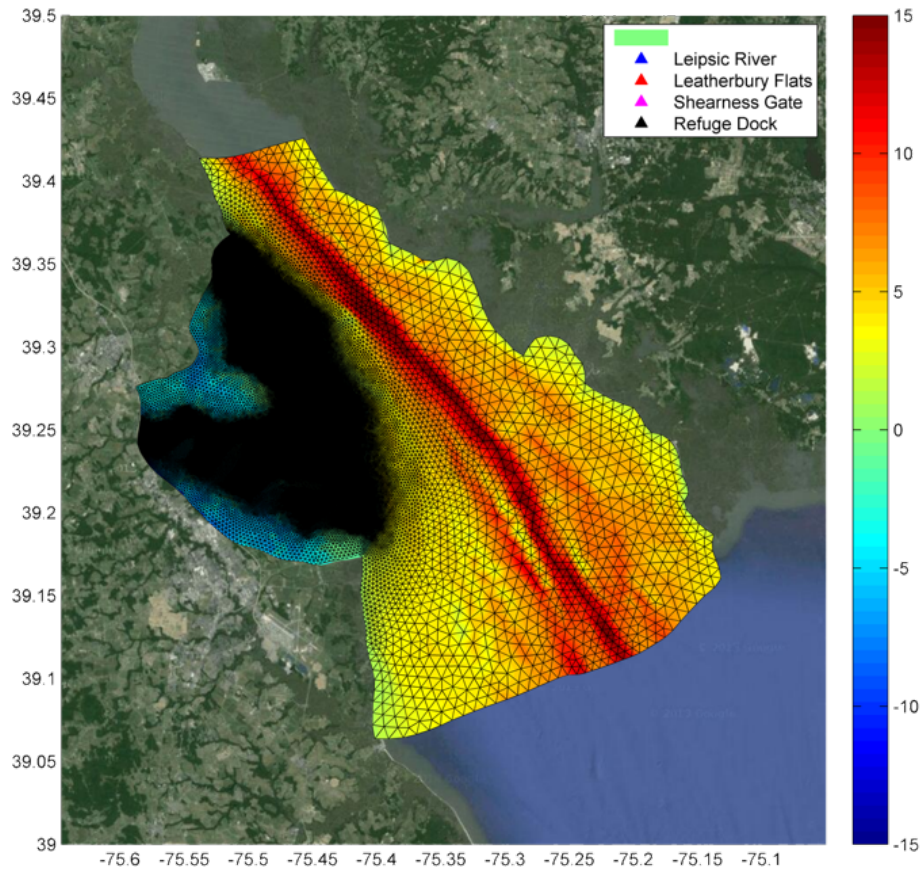


Figure 13: Unstructured grid domain used for the hydrodynamic and sediment transport study in BHNWR. The colorbar on the right represents the topo-bathymetry (in meters) referenced to NAVD88 vertical level. The forcing boundaries are the transects across the bay at the northern and southern limits of the grid.

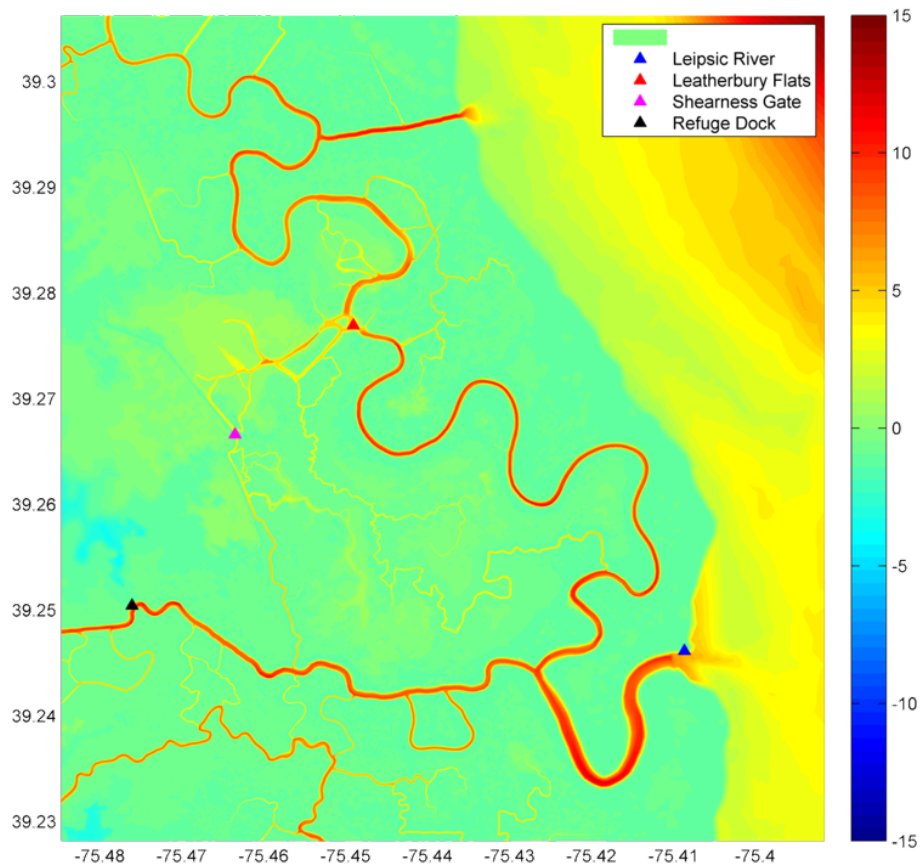


Figure 14: Higher resolution representation of the BHNWR channels and mudflats. The contour label on the right represents the topo-bathymetry (in meters) referenced to NAVD88 vertical level. Locations of four tide gauges inside BHNWR, used for model validation, are indicated.

### 3 FVCOM hydrodynamic modeling and validation (2D)

We have used the Finite - Volume Coastal Ocean circulation Model FVCOM (Chen *et al.*, 2013) to develop a high resolution, tidal creek resolving, hydrodynamic and sediment transport model for our study area. This model has been previously used in several estuarine and coastal studies featuring complex topo-bathymetry, inter-tidal wetting and drying, and irregular coastline (Chen *et al.*, 2008). Zhao *et al.* (2010) used FVCOM 3D successfully to analyze wetland-estuarine-shelf interaction processes in the Plum Island Sound and Merrimack River system in the Massachusetts coast. Similarly, Ralston *et al.* (2013) validated FVCOM using field data and investigated hydrodynamics and sediment transport on deltaic tidal flats at the mouth of the Skagit River, in Puget Sound, WA.

FVCOM solves seven primitive governing equations, three for momentum, one for incompressible continuity, two for temperature and salinity, and one for density. The primitive equations described in the following section are mathematically closed using horizontal and vertical diffusion for momentum, temperature and salinity. Users can choose between using a constant value or the Smagorinsky eddy parameterization method for the horizontal diffusion coefficient. For vertical eddy viscosity and vertical thermal diffusion coefficients, FVCOM provides a wide range of ocean turbulence closure models such as Mellor and Yamada level-2.5 (MY-2.5) and  $k - \epsilon$ . The model uses  $\sigma$  or  $s$  coordinates in the vertical, or a hybrid coordinate in the vertical to convert the irregular bottom topography to a uniform image domain. The momentum equations are solved using the mode-splitting method, in which, an external mode solves 2D depth-integrated equations and an internal mode solves the equations in vertical direction. The finite-volume approach in FVCOM guarantees mass conservation in both individual control elements and the entire computational domain, as it solves integral form of the equations via flux calculation over a random sized triangular

grid.

### 3.1 FVCOM model description

The 3-D primitive equations in the cartesian coordinates are

$$\frac{\partial u}{\partial t} + u \frac{\partial u}{\partial x} + v \frac{\partial u}{\partial y} + w \frac{\partial u}{\partial z} - f v = -\frac{1}{\rho_0} \frac{\partial(p_H + p_a)}{\partial x} - \frac{1}{\rho_0} \frac{\partial q}{\partial x} + \frac{\partial}{\partial z} (K_m \frac{\partial u}{\partial z}) + F_u \quad (1)$$

$$\frac{\partial v}{\partial t} + u \frac{\partial v}{\partial x} + v \frac{\partial v}{\partial y} + w \frac{\partial v}{\partial z} + f u = -\frac{1}{\rho_0} \frac{\partial(p_H + p_a)}{\partial y} - \frac{1}{\rho_0} \frac{\partial q}{\partial y} + \frac{\partial}{\partial z} (K_m \frac{\partial v}{\partial z}) + F_v \quad (2)$$

$$\frac{\partial w}{\partial t} + u \frac{\partial w}{\partial x} + v \frac{\partial w}{\partial y} + w \frac{\partial w}{\partial z} = -\frac{1}{\rho_0} \frac{\partial q}{\partial z} + \frac{\partial}{\partial z} (K_m \frac{\partial w}{\partial z}) + F_w \quad (3)$$

$$\frac{\partial u}{\partial x} + \frac{\partial v}{\partial y} + \frac{\partial w}{\partial z} = 0 \quad (4)$$

$$\frac{\partial T}{\partial t} + u \frac{\partial T}{\partial x} + v \frac{\partial T}{\partial y} + w \frac{\partial T}{\partial z} = \frac{\partial}{\partial z} (K_h \frac{\partial T}{\partial z}) + F_T \quad (5)$$

$$\frac{\partial S}{\partial t} + u \frac{\partial S}{\partial x} + v \frac{\partial S}{\partial y} + w \frac{\partial S}{\partial z} = \frac{\partial}{\partial z} (K_h \frac{\partial S}{\partial z}) + F_S \quad (6)$$

$$\rho = \rho(T, S, p) \quad (7)$$

where  $x, y$  and  $z$  are the east, north, and vertical axes in the Cartesian coordinate system;  $u, v$  and  $w$  are the  $x, y, z$  velocity components,  $T$  is the temperature,  $S$  is the salinity,  $\rho$  is the density,  $p_a$  is the air pressure at sea surface,  $p_H$  is the hydrostatic pressure,  $q$  is the non-hydrostatic pressure,  $f$  is the Coriolis parameter,  $g$  is the gravitational acceleration,  $K_m$  is the vertical eddy viscosity coefficient; and  $K_h$  is the thermal vertical eddy diffusion coefficient.  $F_u$ ,  $F_v$ ,  $F_T$  and  $F_S$  represent the horizontal momentum, thermal, and salt diffusion terms. Detailed description of these terms and surface and bottom boundary conditions for  $u, v, w, T$  and  $S$  are given in [Chen \*et al.\* \(2013\)](#).

For the model efficiency, the momentum equations are solved using the mode-splitting method which includes an external model and internal model. The external mode is a gravity wave mode which solves the 2-D depth-integrated equations in a smaller time step.

The internal mode is a vertical shear mode solving the 3-D equations in the vertical direction. The internal mode can be solved in a larger time step. The 2-D, depth-integrated momentum and continuity equations in the generalized terrain-following coordinate system are given as

$$\frac{\partial \eta}{\partial t} + \frac{\partial(\bar{u}D)}{\partial x} + \frac{\partial(\bar{v}D)}{\partial y} = 0 \quad (8)$$

$$\begin{aligned} & \frac{\partial \bar{u}D}{\partial t} + \frac{\partial \bar{u}^2 D}{\partial x} + \frac{\partial \bar{u}\bar{v}D}{\partial y} - f\bar{v}D - D\bar{F}_u - G_x - \frac{\tau_{sx} - \tau_{bx}}{\rho_0} \\ & = -gD \frac{\partial \eta}{\partial x} - \frac{D}{\rho_0} \frac{\partial p_a}{\partial x} - \frac{g}{\rho_0} \int_{-1}^0 (J[\int_r^0 J(\frac{\partial \rho}{\partial x} + \frac{\partial \rho}{\partial r'} \frac{\partial r'}{\partial x})dr'])dr' - \frac{1}{\rho_0} \int_{-1}^0 J(\frac{\partial qJ}{\partial x} + \frac{\partial qA_1}{\partial r}dr') \end{aligned} \quad (9)$$

$$\begin{aligned} & \frac{\partial \bar{v}D}{\partial t} + \frac{\partial \bar{u}\bar{v}D}{\partial x} + \frac{\partial \bar{v}^2 D}{\partial y} + f\bar{u}D - D\bar{F}_v - G_y - \frac{\tau_{sy} - \tau_{by}}{\rho_0} \\ & = -gD \frac{\partial \eta}{\partial y} - \frac{D}{\rho_0} \frac{\partial p_a}{\partial y} - \frac{g}{\rho_0} \int_{-1}^0 (J[\int_r^0 J(\frac{\partial \rho}{\partial y} + \frac{\partial \rho}{\partial r'} \frac{\partial r'}{\partial y})dr'])dr' - \frac{1}{\rho_0} \int_{-1}^0 J(\frac{\partial qJ}{\partial y} + \frac{\partial qA_2}{\partial r}dr') \end{aligned} \quad (10)$$

where,  $J = \frac{\partial z}{\partial r}$ ,  $A_1$  and  $A_2$  are coordinate transformation coefficients defined as  $A_1 = J \frac{\partial r}{\partial x}$  and  $A_2 = J \frac{\partial r}{\partial y}$ .  $G_x$  and  $G_y$  are

$$G_x = \frac{\partial \bar{u}^2 D}{\partial x} + \frac{\partial \bar{u}\bar{v}D}{\partial y} - D\tilde{F}_x - [\frac{\partial \bar{u}^2 D}{\partial x} + \frac{\partial \bar{u}\bar{v}D}{\partial y} - D\bar{F}_x] \quad (11)$$

$$G_y = \frac{\partial \bar{u}\bar{v}D}{\partial x} + \frac{\partial \bar{v}^2 D}{\partial y} - D\tilde{F}_y - [\frac{\partial \bar{u}\bar{v}D}{\partial x} + \frac{\partial \bar{v}^2 D}{\partial y} - D\bar{F}_y] \quad (12)$$

and the horizontal diffusion terms are approximately given as

$$D\tilde{F}_x \approx \frac{\partial}{\partial x} [2\bar{A}_m h \frac{\partial \bar{u}}{\partial x}] + \frac{\partial}{\partial y} [\bar{A}_m h (\frac{\partial \bar{u}}{\partial y} + \frac{\partial \bar{v}}{\partial x})] \quad (13)$$

$$D\tilde{F}_y \approx \frac{\partial}{\partial x} [\bar{A}_m h (\frac{\partial \bar{u}}{\partial y} + \frac{\partial \bar{v}}{\partial x})] + \frac{\partial}{\partial y} [2\bar{A}_m h \frac{\partial \bar{v}}{\partial y}] \quad (14)$$

$$D\bar{F}_x \approx \frac{\partial}{\partial x} [2A_m h \frac{\partial u}{\partial x}] + \frac{\partial}{\partial y} [A_m h (\frac{\partial u}{\partial y} + \frac{\partial v}{\partial x})] \quad (15)$$

$$D\bar{F}_y \approx \frac{\partial}{\partial x} \overline{[A_m h (\frac{\partial u}{\partial y} + \frac{\partial v}{\partial x})]} + \frac{\partial}{\partial y} \overline{[2A_m h \frac{\partial v}{\partial y}]} \quad (16)$$

Overbar here denotes the vertical integration,  $D = h + \eta$  is the total depth and  $A_m$  is the horizontal eddy diffusion coefficient.

### 3.1.1 Model forcing

For the unstructured grid FVCOM hydrodynamic modeling in BHNWR area, we extracted surface elevation and flux information at the model grid boundary nodes (both upstream and downstream) from a large scale study using Regional Ocean Modeling System (ROMS) [<https://www.myroms.org/>]. ROMS simulations were performed for the year of 2012 and 2015 which covered the entire Delaware Bay ([Kukulka \*et al.\*, 2017](#); [Rodrigues, 2016](#)). The ocean model is driven with the tidal constituents and wind forcing at a larger scale, and results are compared against NOAA tide gauges located in the Bay. The structured grid domain used for ROMS goes up to the continental shelf boundary and covers the entire Delaware Bay and estuary as is shown in Figure 15 ([Abdolali \*et al.\*, 2016b](#)).

At the open ocean boundary, amplitude and phases of nine tidal harmonics (M2, S2, M4, M6, K2, K1, N2, O1, and Q1) have been imposed from ADCIRC database. Meteorological forces are taken from the NAM model and river discharge data has been added from a USGS gauge at the upstream boundary that represents the Delaware River. ROMS output showed that it eventually lacks accuracy in predicting the sub-tidal surface elevation, possibly due to inaccurate representation of the remote forcing. We have separated the sub-tidal signal from ROMS results using harmonic analysis, and replaced it with the local tide gauge data from bay locations close to BHNWR. Then, we forced the model with corrected sub-tidal data and volume flux from the grid open boundary. In FVCOM, it is possible to implement three different nesting conditions at the boundary, denoted as "direct nesting", "indirect

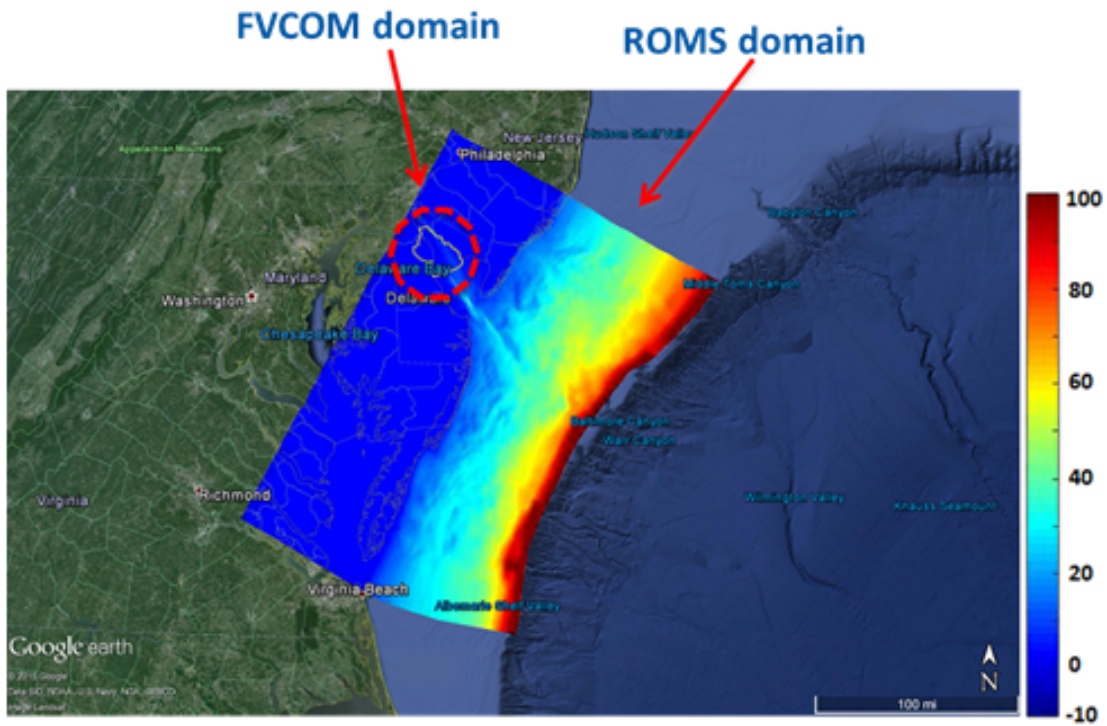


Figure 15: Unstructured grid model FVCOM and structured grid model ROMS domains covering the entire Delaware Bay and estuary. Color label on the right side represents depth (in meters, from NAVD88 vertical reference level).

nesting" and "relaxation nesting". In our study, we used the "direct nesting" approach, which allows nesting between small domain FVCOM and large domain ROMS. The variables at boundary nodes and cells, mainly surface elevation and current data are required from the larger domain. Figure 16 shows an example of "direct nesting" between FVCOM and ROMS model that has been collected from the FVCOM developer website.

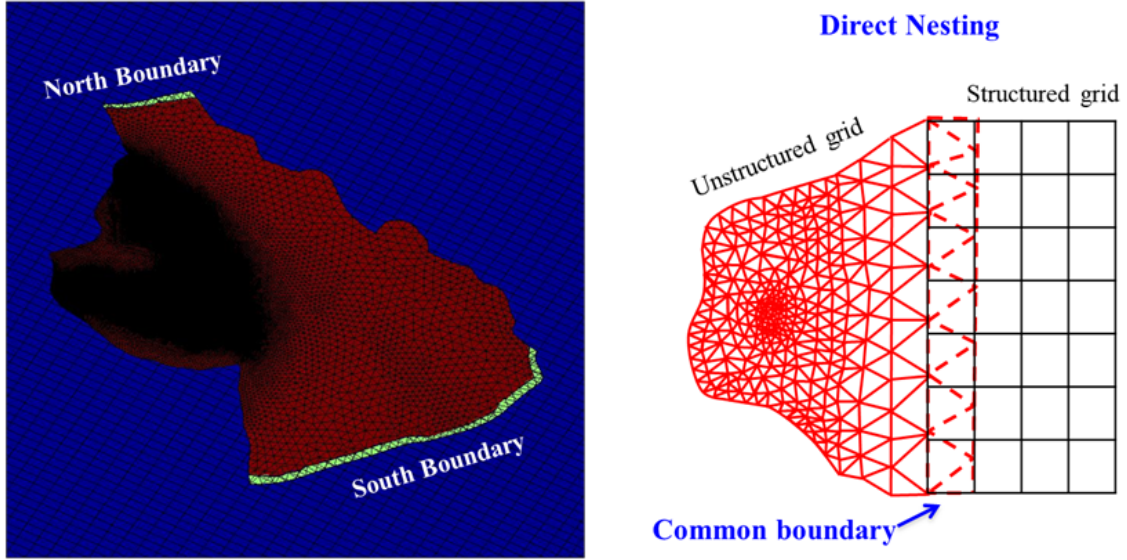


Figure 16: Unstructured grid model FVCOM (left subplot, red surface) and structured grid model ROMS (left subplot, blue surface) direct nesting at the common boundary. Variables at the unstructured grid boundary nodes and cells are extracted from overlapped structured grid.

### 3.1.2 ROMS sub-tidal correction

To properly represent surface elevation at the FVCOM boundary, we separated the elevation data from ROMS into tidal and sub-tidal signals using *t-tide*, a tidal harmonic analysis tool (Pawlowicz *et al.*, 2002). Then, we applied the same procedure to data collected from a few local tide gauges and replaced the sub-tidal information from ROMS with the in-situ data. At first, we compared the ROMS and in-situ tidal harmonics and then looked into the sub-tidal comparison (Figure 17). From Figure 17 (third subplot) we can clearly see that ROMS underestimates the sub-tidal signal at Ship John Shoal tide gauge, Delaware Bay. We implemented the same procedure on other publicly available tide gauge datasets from Delaware Bay and observed a similar trend. This underestimation of the sub-tidal signal could be due to inaccurate representation of the remote forcing as mentioned before.

Finally, we have superimposed the ROMS tidal harmonics at the FVCOM boundary nodes with in-situ sub-tidal data from NOAA tide gauges near to both the boundaries. This has improved the surface elevation forcing at FVCOM boundaries. Meanwhile, we kept the volume flux information from ROMS unchanged at the FVCOM boundary nodes, and did not pursue any additional correction.

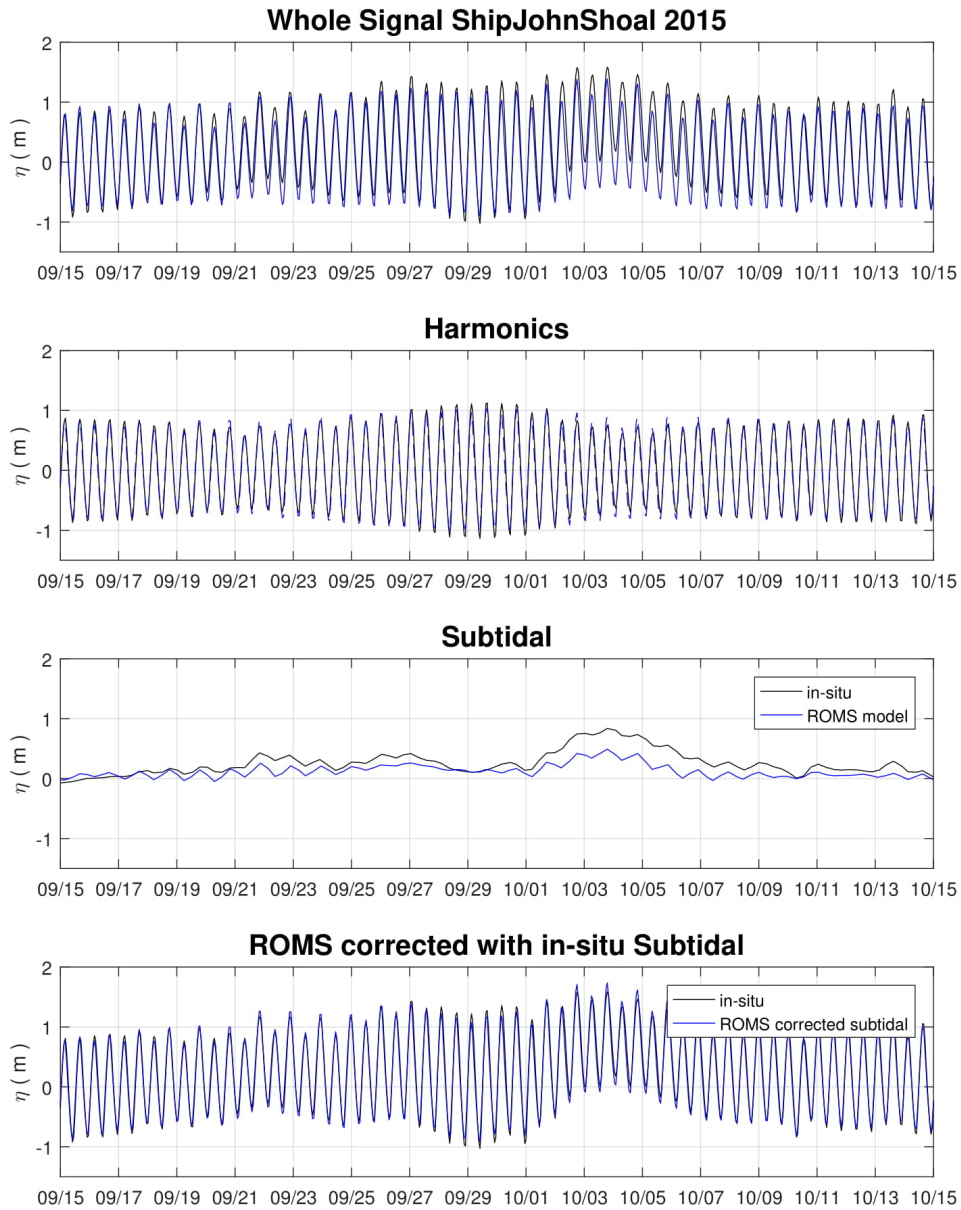


Figure 17: An illustration showing the correction sub-tidal signals from ROMS results. The top subplot shows surface elevation comparison between ROMS and in-situ data from a NOAA tide gauge (at Ship John Shoal, Delaware Bay) during September 15 to October 15, 2015. Surface elevation was separated into harmonics and sub-tidal (second and third subplot) using t-tide. Finally, the corrected surface elevation is generated from superimposed ROMS harmonics and in-situ sub-tidal (bottom subplot).

### 3.1.3 Water level over marsh platform

We deployed 6 Onset HOBO U20 water-level logger in the marsh platform to continuously measure the pressure during 2015. This small submersible pressure logger is capable of recording about 22,000 pressure and temperature samples at rates up to 1 Hz. The raw pressure data recorded by HOBO gauge is in kilopascal (KPa). Initially, we converted it to Decibar (dBar) and then removed the barometric pressure to get water surface elevation (in meters). Figure 18 shows the wetting and drying over marsh surface at our HOBO gauge locations, which later have been used in the model hydrodynamic validation.

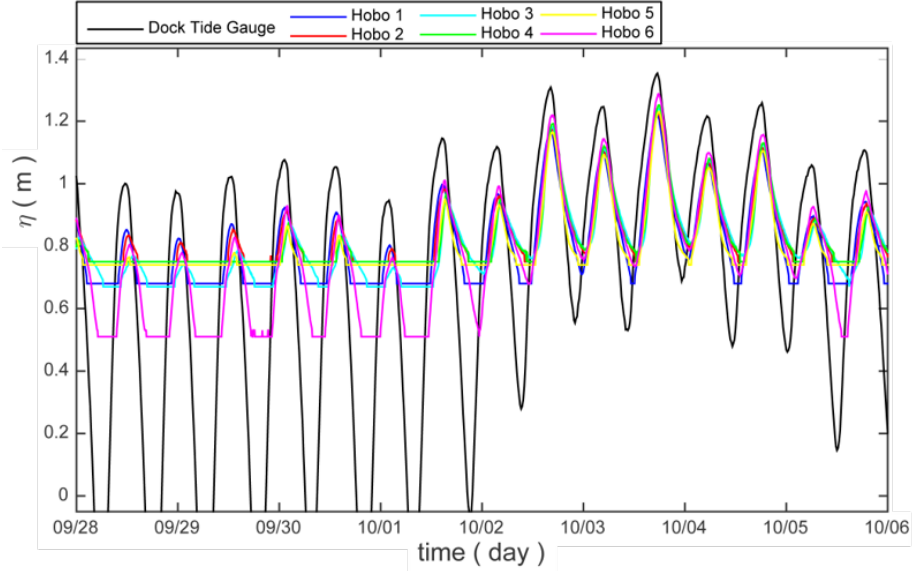


Figure 18: Water level data recorded using HOBO pressure gauge at six locations on the BHNWR marsh platform. The Dock tide gauge shows the water level variation in Leipsic River. The geographic locations of the HOBO gauges are shown in Figure 24.

## 3.2 Model validation

Initially, we collected boundary forcing data sets such as surface elevation and current at FVCOM open boundary nodes from a greater study of the Delaware area using ROMS for the year of 2012. We compared surface elevation at four tide gauge locations in the Bombay Hook area operated by DNREC (shown previously in Figure 14) and observed a good agreement between the model and observed.

Figure 19 shows the comparison at three tide gauge locations for part of February 2012. This segment includes an event with a strong draw-down of water level in the Bay, which the model reproduces well at tide gauges within BHNWR. These results indicate that the subtidal correction being used in the forcing data is working well.

Figures 20 and 21 shows the model performance during Hurricane Sandy at several locations both in Delaware Bay and BHNWR. This was done particularly to evaluate the inundation of BHNWR salt marsh system during Hurricane Sandy, 2012.

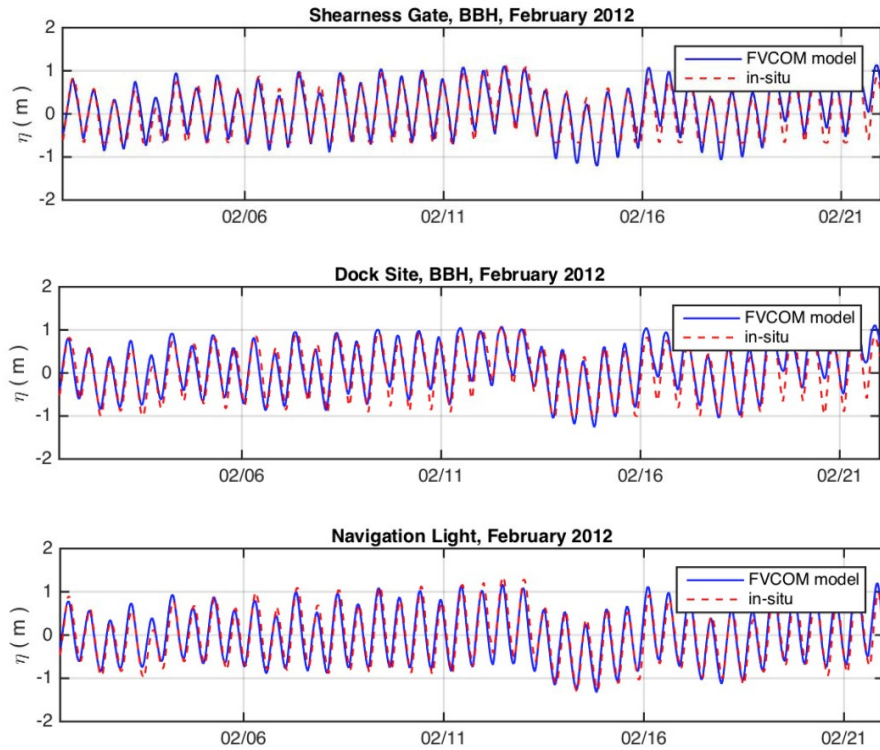


Figure 19: Comparison between FVCOM model (in blue) and in-situ (in red) water surface elevation during February, 2012 at different tide gauge locations in the BHNWR (in meters, from NAVD88 vertical reference level)

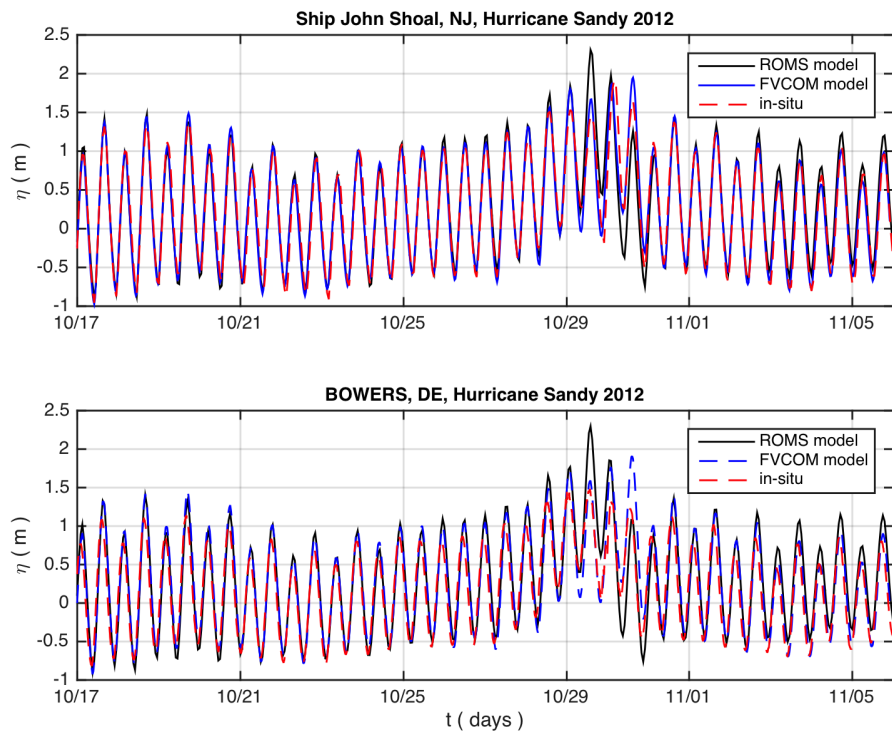


Figure 20: Comparison between ROMS (in black), FVCOM (in blue) and in-situ (in red) water surface elevation during Hurricane Sandy, 2012 at different tide gauge locations in the Delaware Bay (in meters, from NAVD88 vertical reference level)

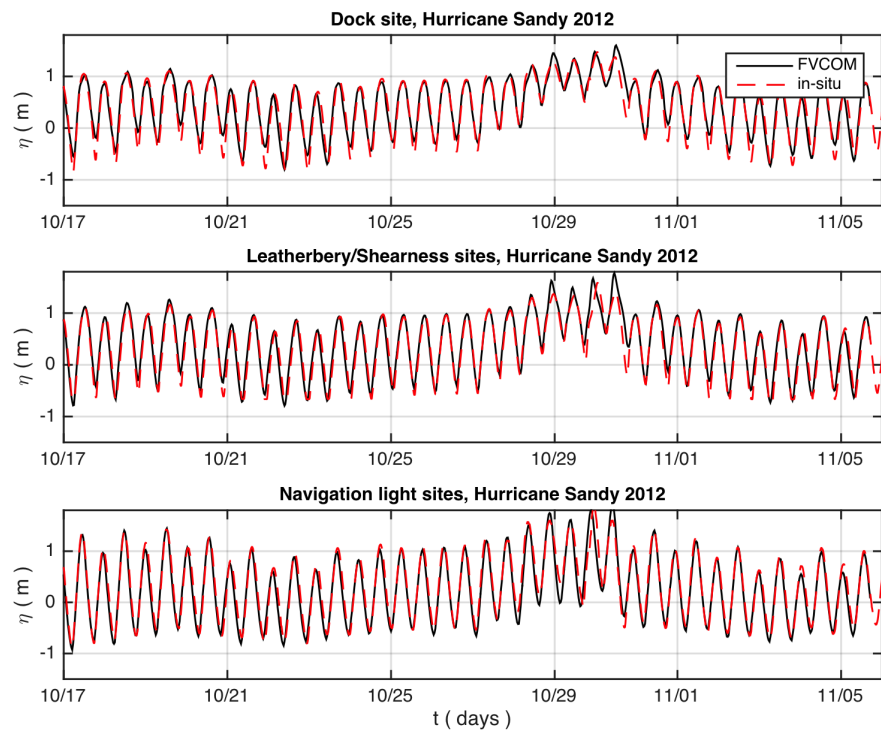


Figure 21: Comparison between FVCOM (in black) and in-situ (in red) water surface elevation during Hurricane Sandy, 2012 at different tide gauge locations in the BHNWR (in meters, from NAVD88 vertical reference level)

The model was seen to exhibit one particular problem; a continuous storage of water on the marsh platform due to artificially isolated low spots in the model DEM depressions formed by channel berms. Figure 22 shows an example of this artificial ponding and drainage problem over the marsh surface during low tide. The artificial ponding results from the inability of model DEM to resolve small cuts and rills that drain these depressions during low tide, leading to excess storage over the marsh surface. This is a significant modeling error if we want to resolve flow hydrodynamics and sediment transport over marsh surfaces. This was more evident after evaluating the total volume of water going in and out of the system, shown in Figure 23. The upper panel of Figure 23b shows the time history of water volume transported to the wetland system, separated from the Bay by a red line in Figure 23a. Figure 23b middle panel shows the volume stored in the channel areas, and indicates that the channels are draining and filling as expected. From the bottom panel of Figure 23b, we can see that the model suffers from inadequate channel connectivity, and the marsh area retains water continuously.

To look into this issue more closely we had deployed and collected water surface elevation on the marsh surface using HOBO water level loggers throughout the year 2015. We have FVCOM model comparison with the field data for the year of 2015 both at the channel and the marsh surface. Figure 24 shows the surface elevation comparison during a storm in September/October 2015 at the four DNREC tide gages within BHNWR. Figure 25 shows results obtained at six stations on the marsh platform. Locations of the HOBO gauges in the marsh are shown in Figure 25a. The results at the six HOBO stations show that FVCOM does a reasonable job of predicting maximum inundation depths, but that the model results show an elevated minimum depth in comparison to the in situ measurements (Figure 25b). There is also an error shown at each location between the low portion of the red lines (indicating local surveyed surface elevation), the elevation of the local grid cell

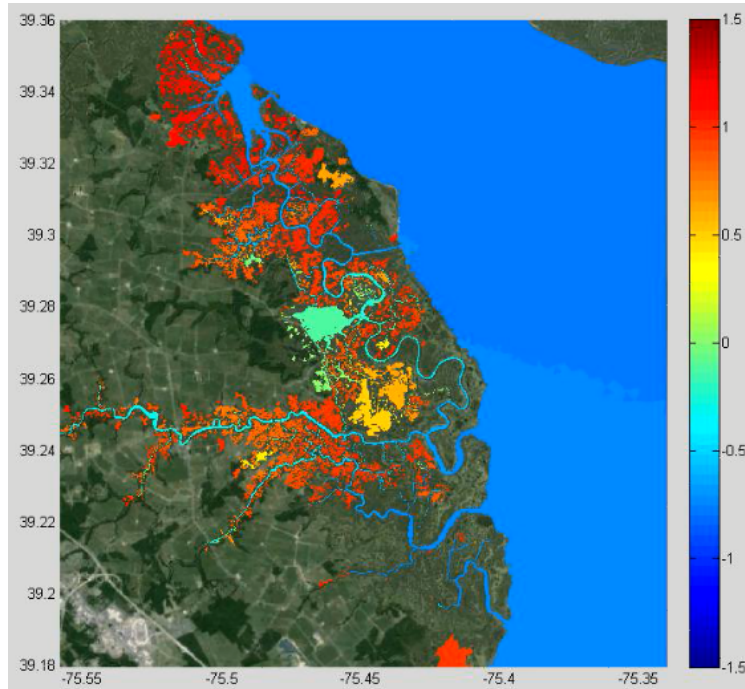


Figure 22: A snapshot of model surface elevation during a low tide and artificial ponding on the marsh platform. The colorbar on the right side represents water surface elevation (in meters, from NAVD88 vertical reference level)

in the model DEM (black line) and the elevation of the gridded NOAA 2011 LiDAR data (green line). The differences between the green and black lines are related to horizontal interpolation and resolution errors in first smoothing over high resolution LiDAR data to get the model DEM, followed by an added error in interpreting local depth in a low order triangulated grid system. These errors are usually comparable to the vertical resolution errors that are inherent to the LiDAR measurement. There are instances, however, where the effect of extra water storage is readily apparent, as seen at HOB0 6.

Aquadopp current profiles were deployed several times during 2015 To measure the flow velocity in various channels. However, we are unable to use most of the data sets for model validation, due to problems with disturbances to the instrument platforms and to bad in-

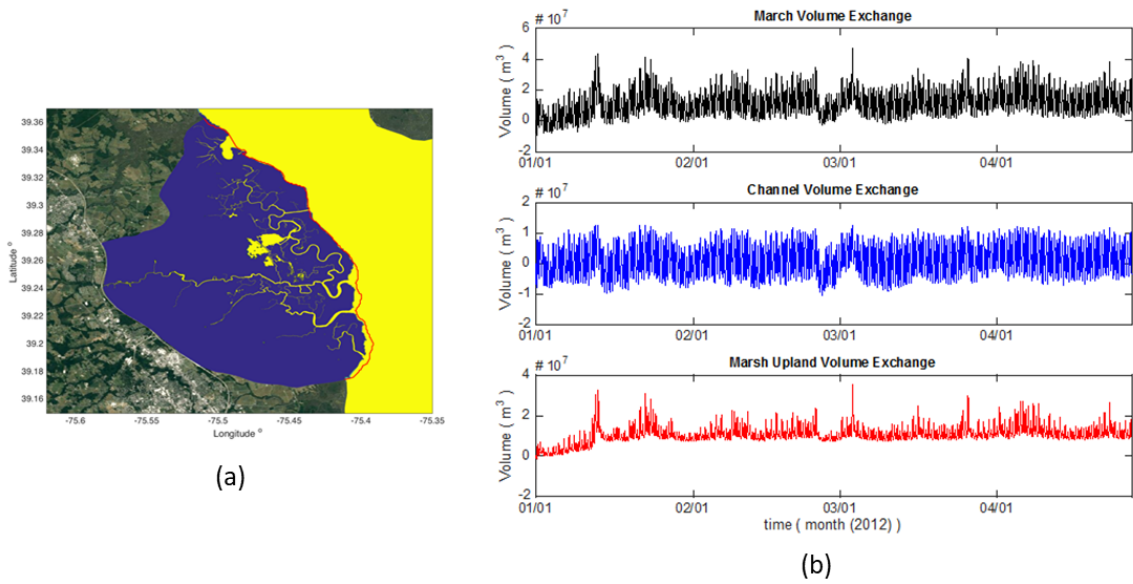


Figure 23: (a) Geographic representation of Bombay Hook wetland and Delaware Bay area separated into land (in blue) and water surface (in yellow) (b) Total volume of water going in and out of the system (top subplot), volume exchange in the channels (middle subplot) and volume exchange over marsh platforms (bottom subplot)

strument configuration in several instances. Here, we have selected one sample aquadopp measurement for model comparison which had no instrument errors during the entire deployment period. Figure 26 shows the instrument location in Duck Creek and data collection period. We can observe from the figure that the depth averaged model velocity agrees well with the collected velocity (depth averaged).

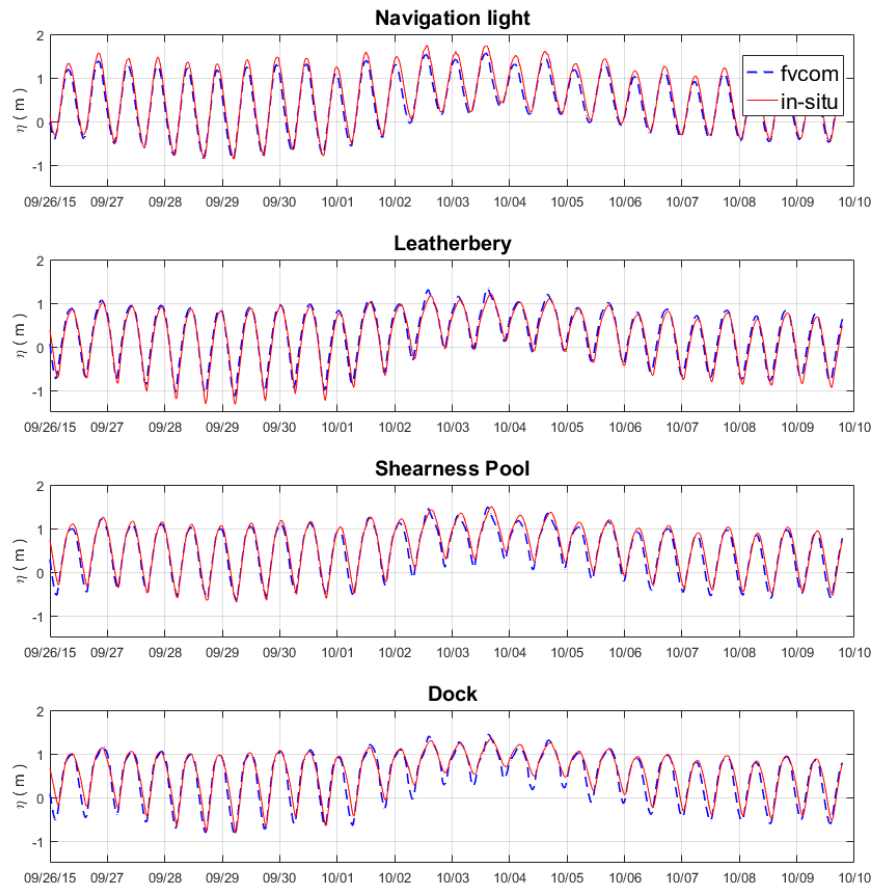
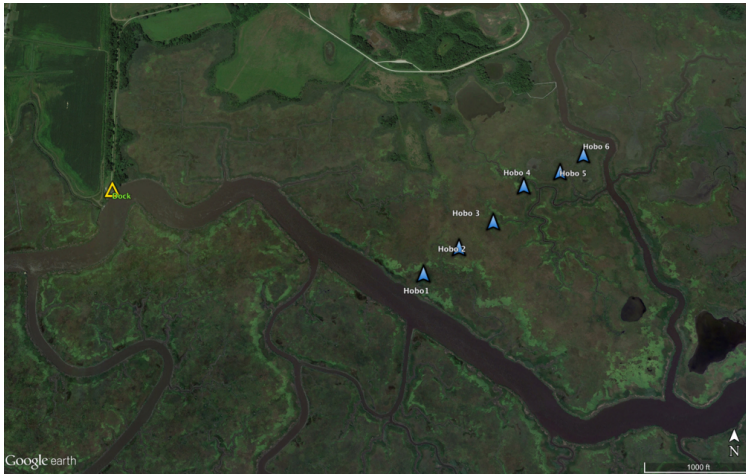
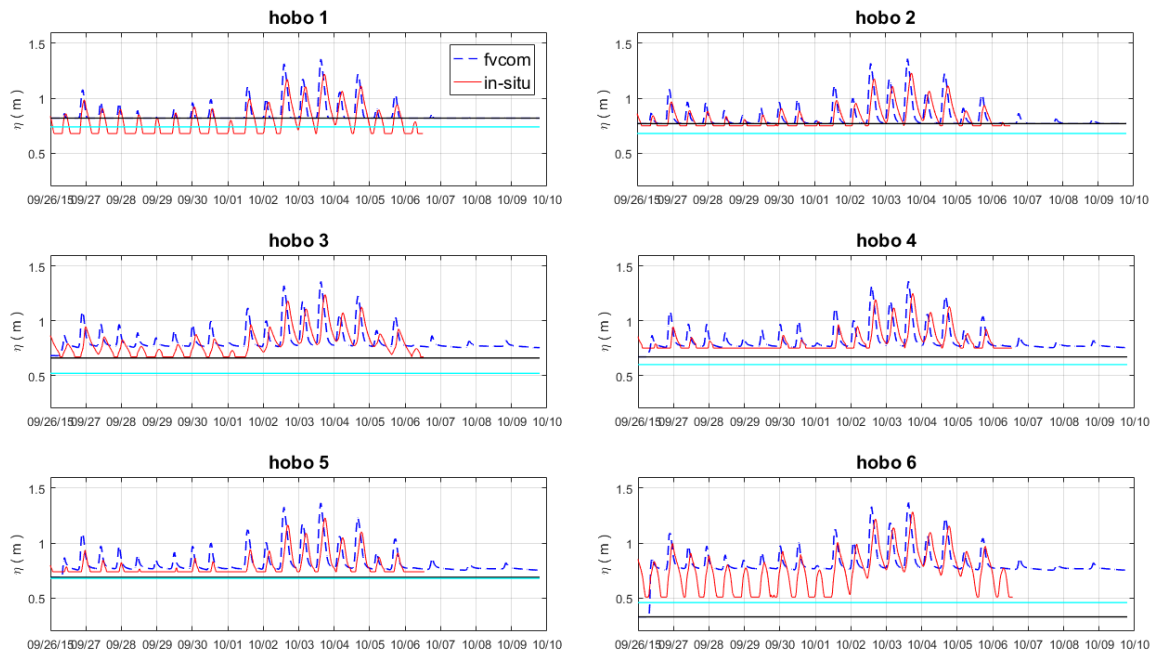


Figure 24: Comparison between FVCOM model (in blue) and in-situ (in red) water surface elevation during September storm, 2015 at different tide gauge locations in the Bombay Hook area (in meters, from NAVD88 vertical reference level).



(a)

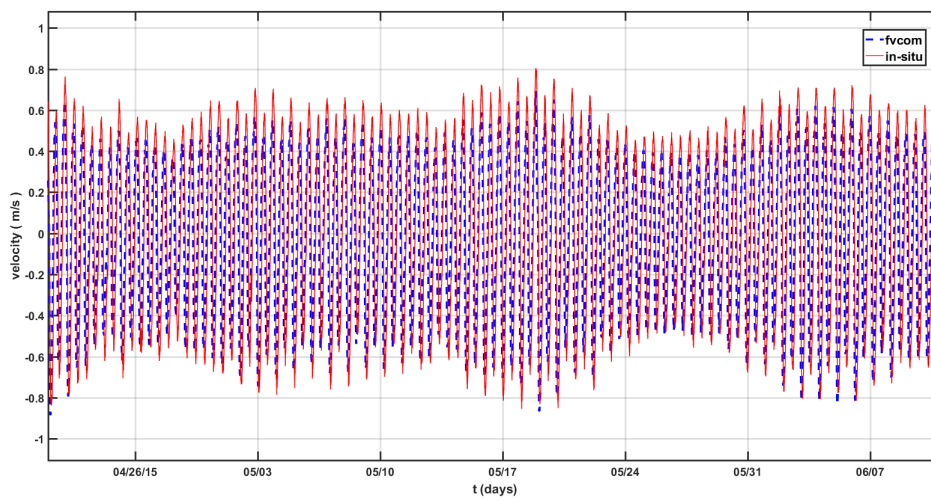


(b)

Figure 25: (a) Geographic location of deployed HOBOS gauges in the Bombay Hook area (b) Comparison between FVCOM model (in blue) and in-situ (in red) water surface elevation during September storm, 2015 at different HOBOS gauge locations (in meters, from NAVD88 vertical reference level)



(a)



(b)

Figure 26: (a) Geographic location of deployed ADCP in Duck Creek (b) Comparison between FVCOM model (in blue) and aquadopp depth-averaged current data (in red) collected from Duck Creek, Bombay Hook during May, 2015

## 4 FVCOM sediment transport model (3D)

One of the main objectives of this study is to evaluate the net import/export of sediment to/from the BHNWR wetland system. The total transport to/from the system depends on many major physical processes such as the hydrodynamics, sediment properties, supply from the Bay, and tidal flat and marsh edge erosion due to wind waves. For the erosion problem in our study area, initially we looked into the sediment exchange in the system in response to the hydrodynamics only. Several historic and probable morphological changes are implemented to assess the role of historic disturbances and channel bathymetry on the ongoing erosion. We used the 3-D sediment module available in FVCOM that includes suspended load and bedload transport, active layer concept, unlimited number of sediment classes and cohesive sediment erosion/deposition algorithms. Concept of the sediment module is taken from the community model for coastal sediment transport developed by the USGS and other researchers (see <http://woodshole.er.usgs.gov/project-pages/sediment-transport/>). Previously, the USGS community sediment transport model has been implemented in structured-grid ocean model ROMS. In FVCOM, it is converted to an unstructured version to use the mass conservative finite-volume approach for sediment advection.

### 4.1 Governing equations

FVCOM sediment module includes transport of both suspended load and bedload. The suspended load model uses a concentration-based approach described in the FVCOM manual as:

$$\frac{\partial C_i}{\partial t} + \frac{\partial u C_i}{\partial x} + \frac{\partial v C_i}{\partial y} + \frac{\partial (w - w_i) C_i}{\partial z} = \frac{\partial}{\partial x} (A_h \frac{\partial C_i}{\partial x}) + \frac{\partial}{\partial y} (A_h \frac{\partial C_i}{\partial y}) + \frac{\partial}{\partial z} (K_h \frac{\partial C_i}{\partial z}) \quad (17)$$

where  $C_i$  is the concentration of sediment  $i$ ,  $A_h$  is the horizontal eddy viscosity and  $K_h$  is the vertical eddy viscosity. The settling velocity  $w_i$  is prescribed by the user for each sediment

type.

The no-flux boundary condition at the surface:

$$K_h \frac{\partial C_i}{\partial z} = 0, \quad z = \eta \quad (18)$$

Sediment flux at the bottom is from the difference between deposition and erosion:

$$K_h \frac{\partial C_i}{\partial z} = E_i - D_i, \quad z = -H \quad (19)$$

The erosion rate:

$$E_i = \Delta t Q_i (1 - P_b) F_{bi} \left( \frac{\tau_b}{\tau_{ci}} - 1 \right) \quad (20)$$

where  $Q_i$  is the erosive flux,  $P_b$  is the bottom porosity,  $F_{bi}$  is the fraction of sediment  $i$  in the bottom,  $\tau_b$  at the bottom shear stress, and  $\tau_{ci}$  is the critical shear stress of sediment  $i$ .

The bedload can be modeled using the Meyer-Peter and Müller formula, and we can define the empirical parameters of the Meyer-Peter and Müller formula using the model sediment input file.

## 4.2 Model forcing and sediment parameters

Initially, we constructed a tidal signal using M2 and S2 constituents only that represents a complete spring-neap cycle and used it to force the model from open boundary nodes (at the Bay side, southern boundary). Information about the tidal constituents is taken from Ship John Shoal tide gauge (operated by NOAA) located in the Delaware Bay. Also, sediment supply into the Bay, salinity and temperature are incorporated using nudging at the open boundary nodes. A constant salinity value of 30 PSU, temperature value 25° C and sediment concentration 50 mg/l is given for boundary nudging. Then, we applied river forcing

(discharge data, sediment load, temperature and salinity) at the model upstream boundary to take the contribution from Delaware river into account. Based on some literatures and field studies on the Delaware estuary (e.g., Sommerfield & Wong (2011)), we defined a continuous average river discharge of 500 cubic meters, salinity value of 15 PSU, temperature value 20° C and sediment concentration 50 mg/l at the river nodes.

For the initial model simulations only one sediment type (fine silt) is selected based on the Bay-Bottom study available from Delaware Estuary Benthic Inventory (DEBI) (see <http://www.delawareestuary.org/data-and-reports/bay-bottom-inventory/>). From the geographic distribution of the bay bottom sediment type, we have identified silt-clay combination as the dominant type around the BHNWR area compared to sand. We have implemented the following values as sediment parameters in our preliminary analysis, taken from a previous FVCOM sediment transport modeling case study by Khangaonkar *et al.* (2017). Sediment type: fine silt, Settling velocity ( $mm/s$ ): 0.1, Mean diameter ( $mm$ ): 0.014 Erosion rate ( $kgm^{-2}s^{-1}$ ):  $1.2 * 10^{-5}$ , Critical stress for erosion ( $Nm^{-2}$ ): 0.05.

## 5 Wetland morphology scenarios and net transport

In recent decades, channel depths inside the BHNWR wetland have progressively increased, and new mudflats are forming due to collapse of previously established marsh platform. These ongoing erosion events lead to hypotheses on a few historical and morphological scenarios. Model simulations with changing morphology can describe the ongoing and future changes of hydrodynamics and sediment transport in BHNWR. The BHNWR area has four different connections the Delaware Bay (Leipsic River, Simon River, Sluice Ditch/Duck Creek and Woodland Beach) connected to each other via interior channels of the wetland system (Figure 27). Of these, the Sluice Ditch channel is an artificially opened inlet which has potentially had a strong impact on tidal exchange and resulting tide range in the interior of the system. In this section, we first establish a baseline based on a month long simulation of the system under regular tidal forcing and using the present geometry. Then, as a first hypothetical historic case, in section 5.1.2 we consider a channel bathymetry set to a maximum depth of 5 m throughout the entire wetland system, and artificially fill the existing Sluice Ditch. Section 5.1.3 considers a similar case of channel depth limited to 5m, but introduces Sluice Ditch into the system. This scenario illustrates the role of Sluice Ditch in enhancing transport processes in the eroding marsh system.

The bay shoreline has also experienced extensive erosion over time due to the action of wind waves, which break at the marsh edge and cause a landward retreat of shoreline. The last scenario considered here considers the effect of a hypothetical breakthrough in the area where Duck Creek is close to the present bay shoreline (Figure 28). This scenario is intended to illustrate the effect of further progressive erosion and the formation of new inlets within the system, and is considered in section 5.1.4.

After carrying out the scenario computations, we consider changes in tidal circulation

resulting from each scenario in section 5.2, and consider potential erosion and net sediment transport effects in section ??.

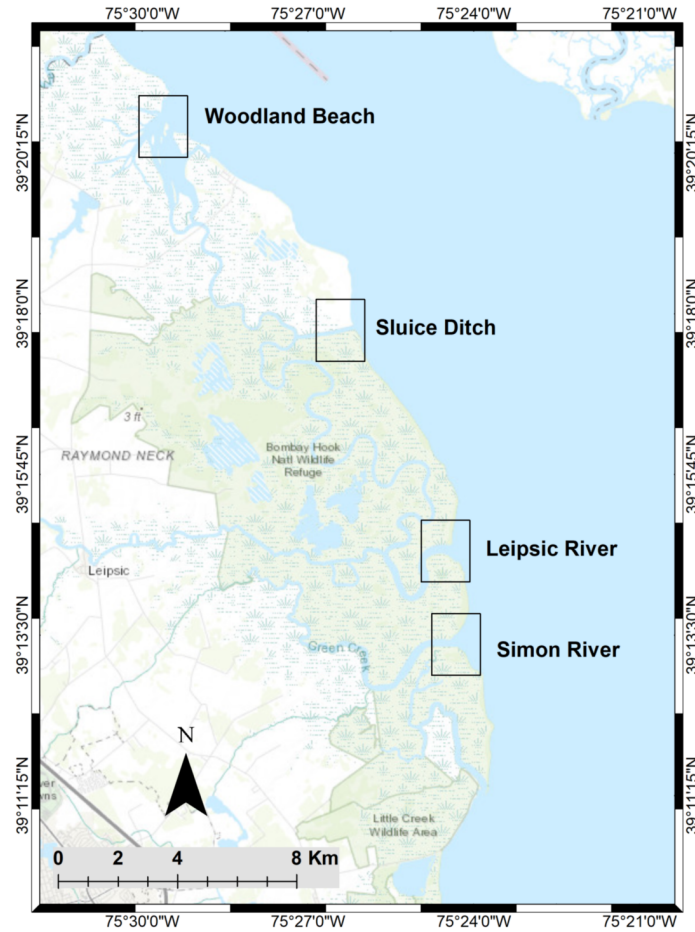


Figure 27: Leipsic River, Simon River, Sluice Ditch/Duck Creek and Woodland Beach inlets that connect BHNWR wetland system with the Delaware estuary and Bay. The total volume and sediment flux going in/out of the system are estimated later using these four inlets.



Figure 28: A critical location close to Leipsic River where an interior pool in the marsh platform is rapidly growing from inside and also the shoreline being eroded due to wind waves. This could possibly end up merging both the interior channel, Duck Creek and the Bay, creating a new inlet for the wetland.

## 5.1 Simulations of scenarios based on altered marsh configurations

### 5.1.1 Baseline conditions.

For our first case, we ran the 3-D model with sediment transport for 23 days considering the existing bathymetry. We chose only two vertical sigma layers for now due to model stability issues that arise from the very shallow bathymetry over marsh platform during a high tide. A uniform friction coefficient of 0.0025 is considered for the preliminary model runs; a more representative map of spatially varying friction coefficient will be developed in the future after issues with artificial ponding are addressed in ongoing work for Sea Grant. The baseline case was run for an entire spring-neap cycle, with all the boundary forcing mentioned in section 3.1.1. Averaging over the full cycle is then carried out to examine net transport as well as spring-neap variations.

First, volume flux in and out of the system through each inlet is determined. A transect is drawn at each river inlet covering the entire width. All unstructured grid nodes and cells that falls close to the transect are selected for depth, water surface elevation and velocity extraction. This first creates a new line of model grid nodes that follows the assigned transect. Subsequently, velocities from the triangular cells on both sides of the line are multiplied by total depth to obtain a local volume flux. Total depth  $h + \eta$  at the cell edge is estimated by averaging between nodes from cell ends, and width of the cell edge is also measured for flux estimation. Multiplying average velocity with total depth and width provides volume flux through each cell at the transect, and an integral over the transect represents total volume flux at each inlet. For the baseline case, the Leipsic River and Sluice Ditch inlets are observed to be ebb dominant, with higher velocities during ebb tide than flood tide, while Simon River and Woodland Beach are flood dominant. We combined fluxes through all the inlets to obtain the total instantaneous flux going into or out of BHNWR,

shown as the bright green lines in Figure 29. The first subplot of the Figure 29 shows total flux for the entire period, and the following ones represent total flux magnitude separated for spring and neap tide cycles. It is apparent that the ebb tidal flux is much stronger than flood tidal flux in the present marsh and under spring tide conditions, where flooding of the marsh platform is enhanced. In contrast, the ebb/flood asymmetry is reduced in neap tide conditions.

The tide averaged volume flux going in/out of BHNWR system is shown in Figure 30 where the mean fluctuates around zero. Total averaged flux is not exactly zero due to the accuracy of approximations used in estimating local fluxes. The values are on the order of 1% of the peak flux magnitude of almost 1250 m<sup>3</sup>/s during spring and 1000 m<sup>3</sup>/s during neap tide.

According to Friedrichs & Madsen (1992) the tidal asymmetry depends on time-varying amplitude, channel depth and embayment width according to

$$\gamma = \frac{5}{3} \frac{a}{\bar{h}_0} - \frac{\Delta \bar{b}}{\bar{b}_0} \quad (21)$$

where  $a$  is amplitude,  $\bar{h}_0$  is the average channel depth,  $\Delta \bar{b}$  represents average change in estuary width between low and high tide,  $\bar{b}_0$  is the average width of the entire embayment. A value of  $\gamma > 0$  indicates that the changes in channel depth during the tidal cycle are more important than changes in embayment width, and the effect of  $\gamma < 0$  is simply the opposite.  $\gamma < 0$  leads to an ebb dominant system, where a faster falling tide is accompanied by a more slowly rising tide (Friedrichs & Madsen, 1992). The scenarios considered below will demonstrate a gradually increasing tendency towards ebb dominance in the system. In our scenarios, the average depth in the Leipsic River increases from 5 m (historic case) to almost 10 m (present model bathymetry) and it is evident that the inlet gradually becomes ebb dominant. We evaluate the role of current embayment width in amplifying the tidal

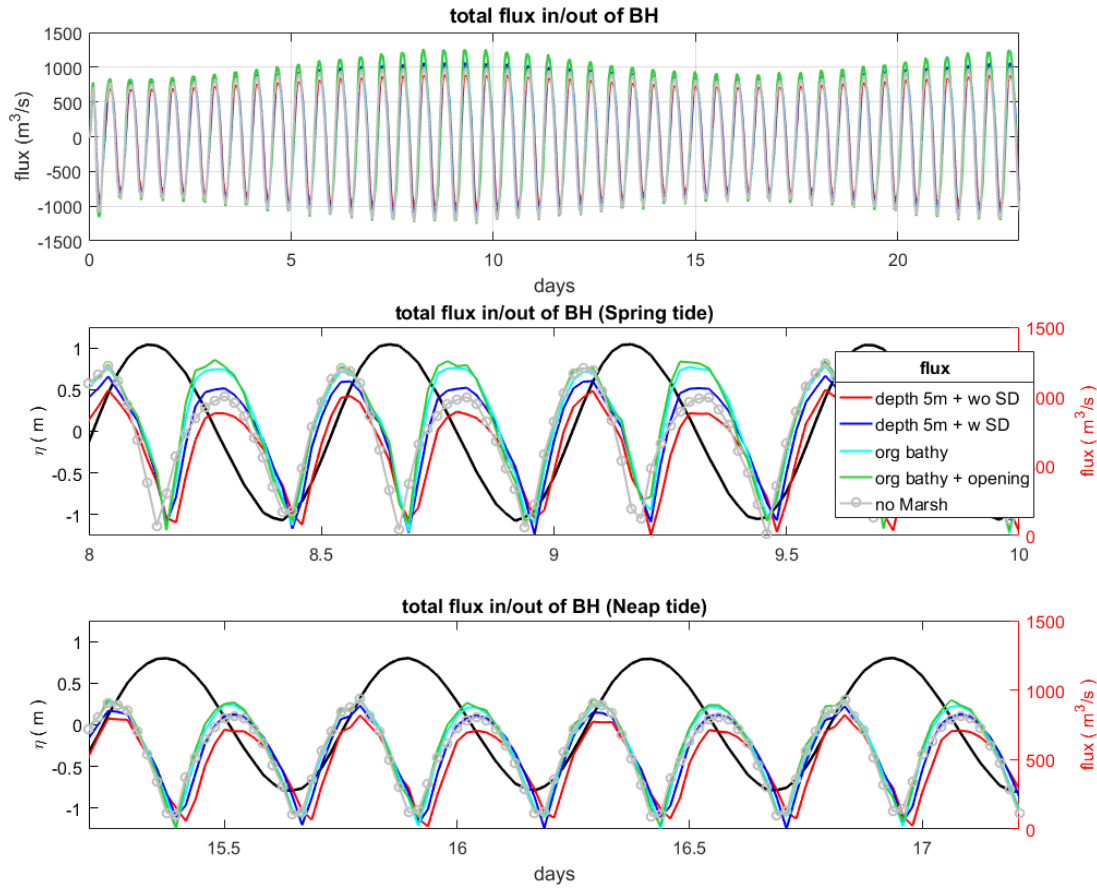


Figure 29: Total volume flux (in  $\text{m}^3/\text{s}$ ) going in/out of BHNWR for different morphological scenarios. First subplot shows total flux for the entire spring-neap cycle used for model run (here, positive flux represents going out from the wetland, negative represents going in). The second and third subplot represents total flux magnitude separated into a spring and neap tidal cycle respectively (label provided on the right side). Surface elevation from a Leipsic River inlet model grid point (referenced to NAVD88, in meters) is shown with the solid black line (label provided on the left side). Flux magnitude and surface elevation are plotted together to identify the asymmetry during flood and ebb tide. [**legend:** depth 5m + wo SD: all channel depth goes up to 5 m and no Sluice Ditch, depth 5m + w SD: depth kept to 5 m and we have Sluice Ditch, org bathy: present grid bathymetry, org bathy + opening: present grid bathymetry with a new inlet, no Marsh: marsh surface is elevated by 2 m and kept above the tidal range]

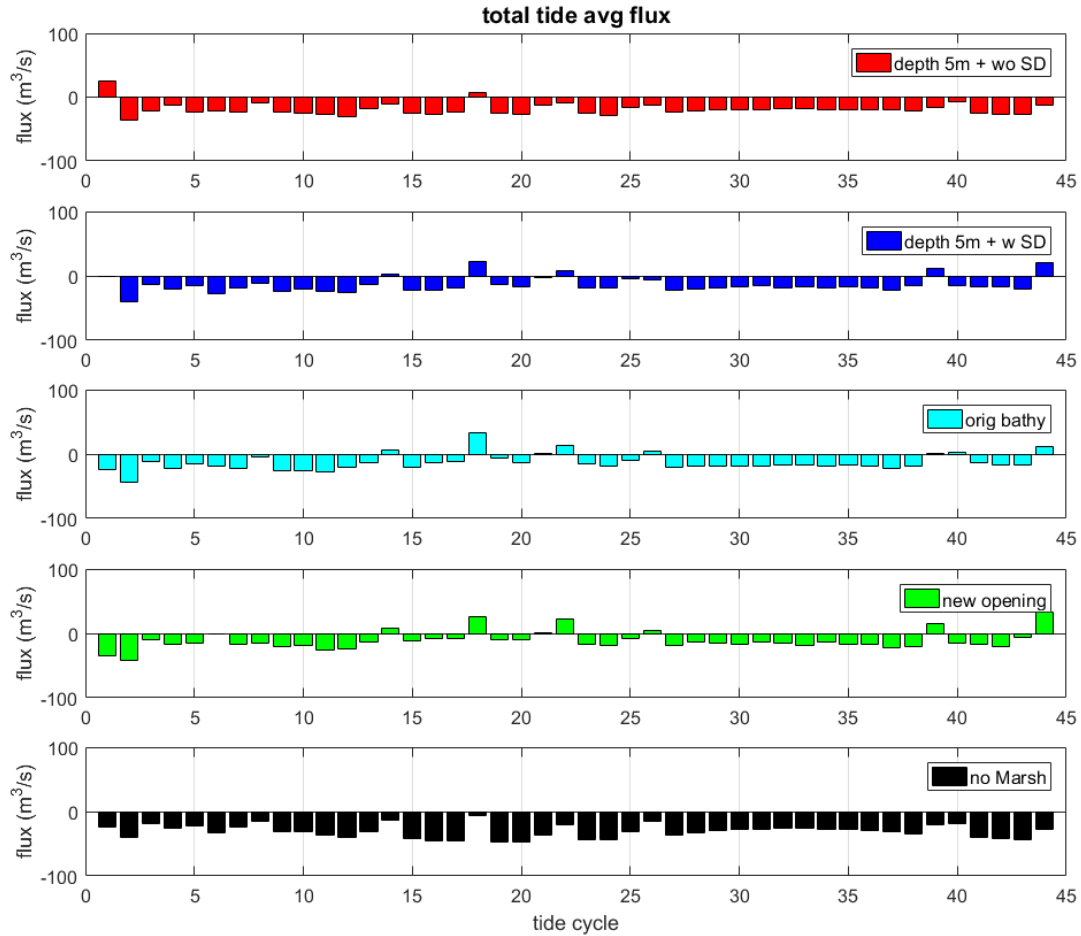


Figure 30: Tide averaged volume flux (in  $\text{m}^3/\text{s}$ ) going in/out of BHNWR for different morphological scenarios. The wave averaging is done by applying zero-upcrossing method on the surface elevation data from Leipsic River inlet model grid point. Total averaged flux is not exactly zero due to approximate estimation using transects; however, it is more or less than 1% of the peak flux magnitude of almost  $1250 \text{ m}^3/\text{s}$  during spring and  $1000 \text{ m}^3/\text{s}$  during neap tide. Detailed description about the figure legend is given in Figure 29.

asymmetry and existing ebb dominance, by keeping the present model channel bathymetry the same but elevating the marsh platform by almost 2 m, in order to reduce variations in channel width associated with overtopping of the marsh platform. The results of this calculation are shown in Figures 29 as the grey curves with circle marks, and as the bottom panel in 30. The results show a clear reversal of the role of asymmetry, with the system being strongly flood dominant during rising spring tides, and with, again, much less of an effect of asymmetry during neap tide conditions.

### 5.1.2 Scenario 1: Reduced channel depth and closure of Sluice Ditch

The first scenario considered consists of reducing maximum channel depths to 5 m and closing Sluice Ditch, which is a step towards simulating historical conditions that were possibly in effect before the start of major erosional changes in the system. We have made no corresponding attempt to narrow channels or recreate river oxbows that have been straightened, and the choice of a 5 m depth is arbitrary. We also note that the tidal flat areas such as Money Marsh would have been areas of continuous marsh platform, further reducing the available volume for tidal exchange. For this case Figure 29 (red curves) shows a shift to flood dominant conditions which mimic the high marsh calculation discussed above. This occurs in spite of the fact that the marsh elevation itself is unaltered in this scenario, and is thus potentially subject to the same level of flooding as in the baseline state. The along-channel velocity at the middle of Leipsic River is still observed to be ebb dominant with an increase in magnitude and duration considering the result with present morphology (Figure 31 & 32). On the other hand, velocity along the channel banks becomes flood dominant, providing a spatially varying tidal asymmetry.

Corresponding stage/discharge results for neap tide are shown in Figure 33, and show a much less pronounced difference between baseline and scenario 1 conditions. Figures 31

and 33 also show much less tendency towards tidal asymmetry in the Simon River, Sluice Ditch and Woodland Beach entrances than is seen in the Leipsic River. Figures 34-36 show results in the same format as Figure 32 for the remaining three entrances, and again show much less asymmetry in flux and velocity.

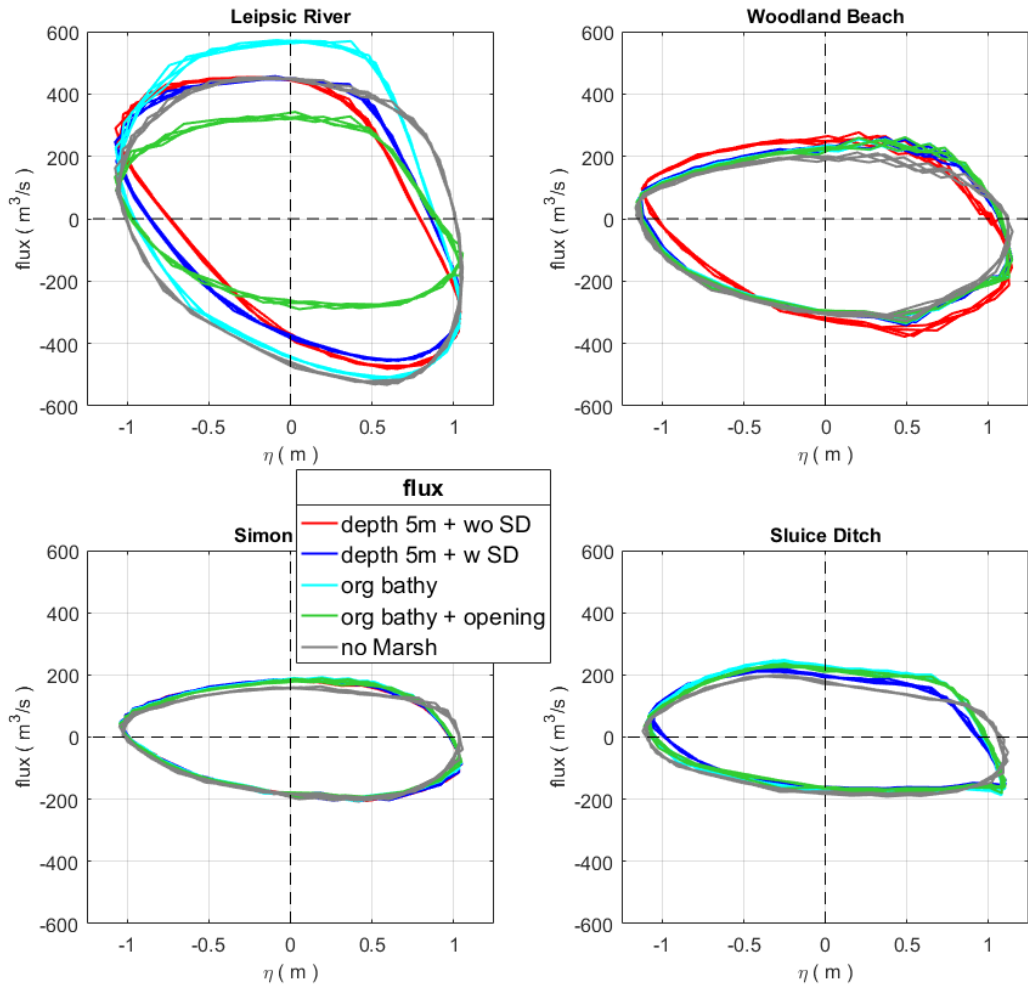


Figure 31: Stage/discharge relationship during a spring tide at the four inlets (Leipsic River, Woodland Beach, Sluice Ditch and Simon River) of BHNWR with different morphology scenarios. Here, positive flux represents going out from the wetland and negative represents going in. Detailed description about the figure legend is given in Figure 29.

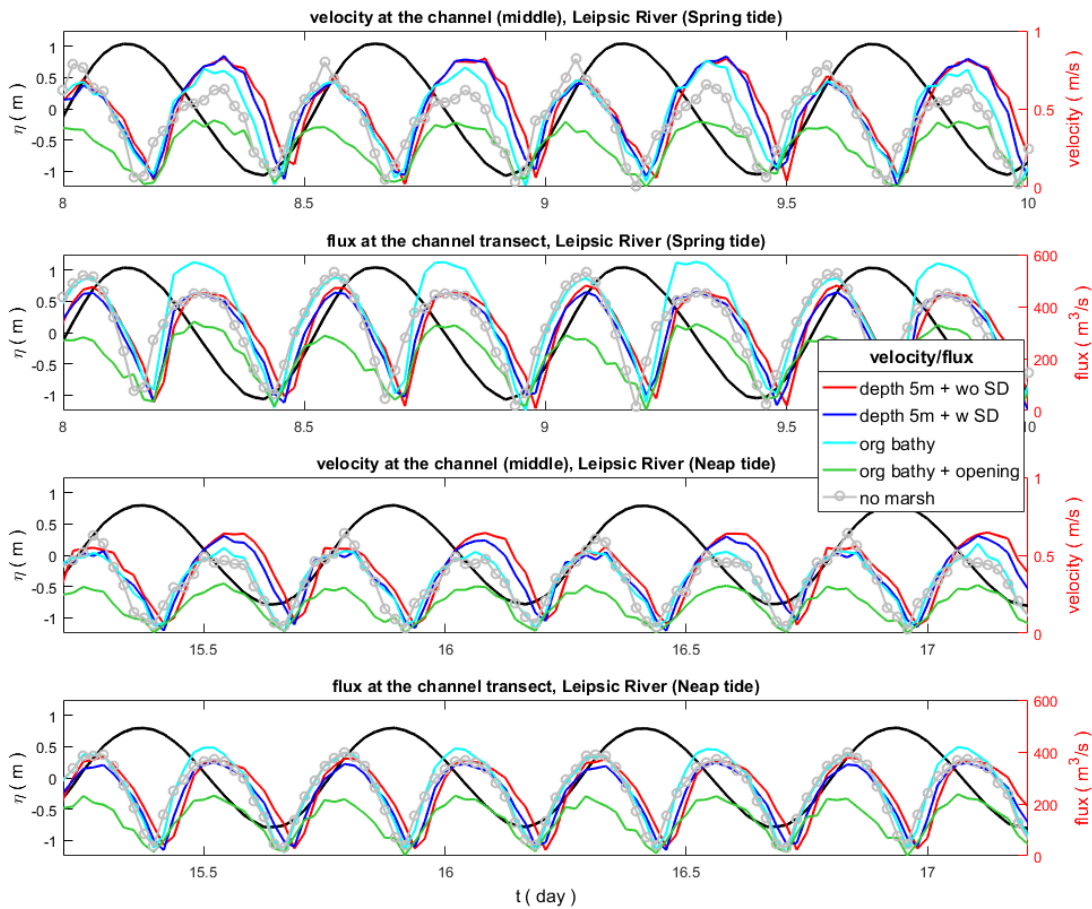


Figure 32: Along channel velocity and volume flux (in  $\text{m}^3/\text{s}$ ) going in/out through Leipsic River inlet for different morphological scenarios. First subplot shows along channel velocity magnitude at the middle of the inlet during a spring tide and the second subplot represents the corresponding volume flux through the entire inlet. Remaining third and fourth subplot displays similar velocity and flux magnitude during a neap tide. Surface elevation from a Leipsic River inlet model grid point (referenced to NAVD88, in meters) is shown with the solid black line (label provided on the left side). Velocity and flux magnitude, and surface elevation are plotted together to identify the asymmetry during flood and ebb tide. Detailed description about the figure legend is given in Figure 29.

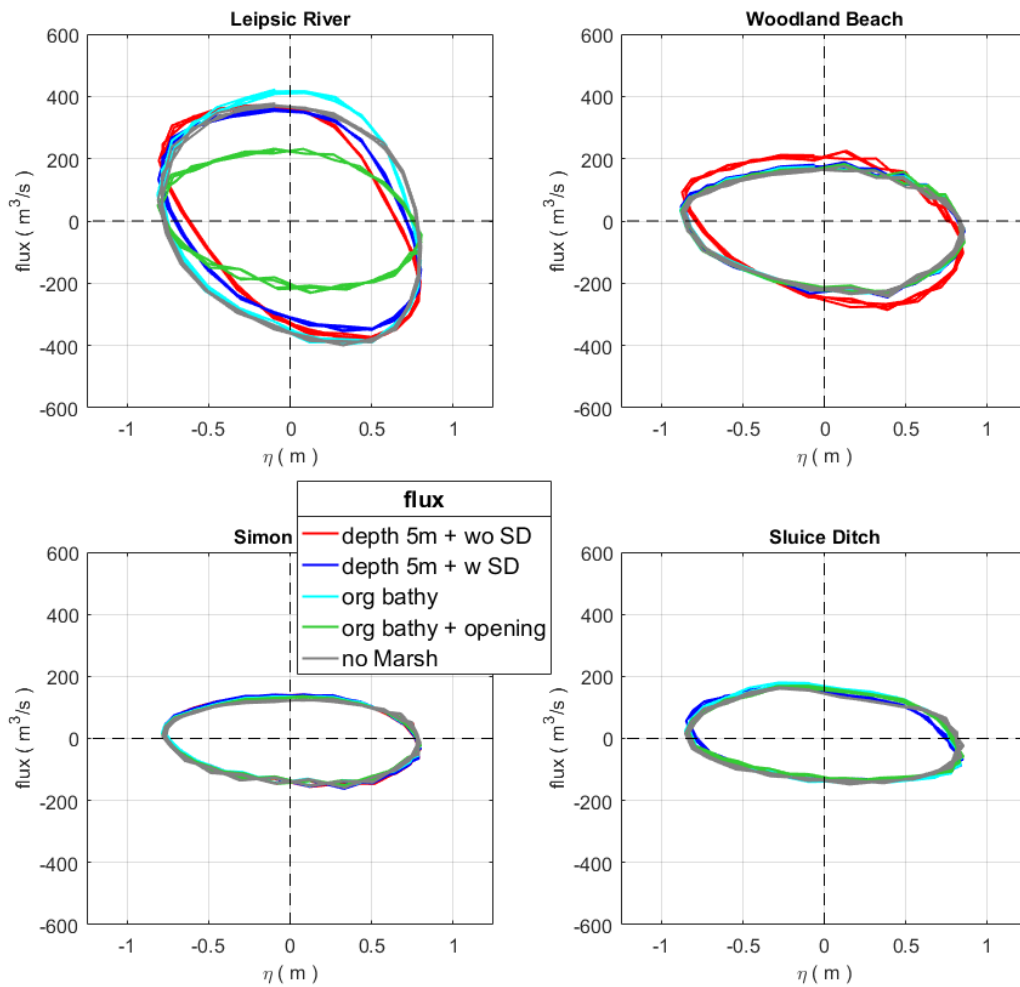


Figure 33: Stage/discharge relationship during a neap tide at the four inlets (Leipsic River, Woodland Beach, Sluice Ditch and Simon River) of BHNWR with different morphology scenarios. Here, positive flux represents going out from the wetland and negative represents going in. Detailed description about the figure legend is given in Figure 29.

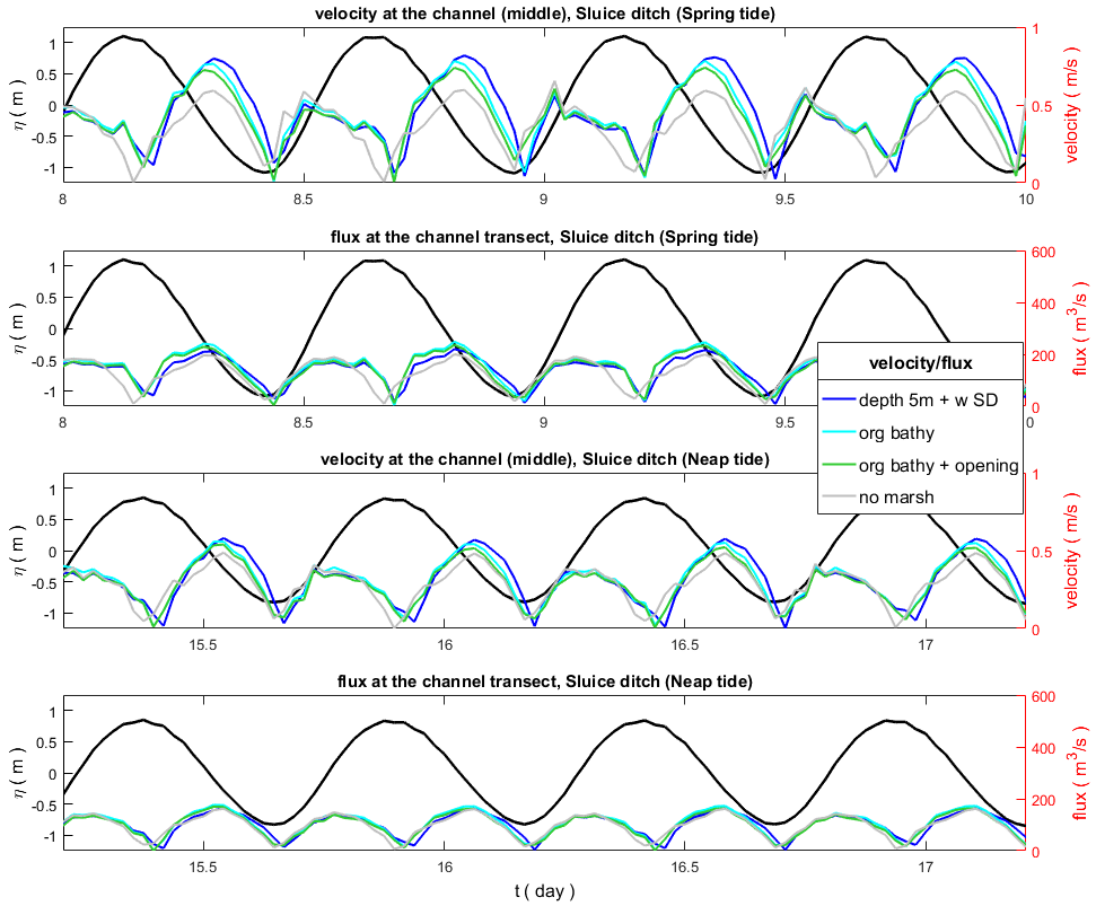


Figure 34: Along channel velocity and volume flux (in  $\text{m}^3/\text{s}$ ) going in/out through Sluice Ditch inlet for different morphological scenarios. First subplot shows along channel velocity magnitude at the middle of the inlet during a spring tide and the second subplot represents the corresponding volume flux through the entire inlet. Remaining third and fourth subplot displays similar velocity and flux magnitude during a neap tide. Surface elevation from a Sluice Ditch inlet model grid point (referenced to NAVD88, in meters) is shown with the solid black line (label provided on the left side). Velocity and flux magnitude, and surface elevation are plotted together to identify the asymmetry during flood and ebb tide. Detailed description about the figure legend is given in Figure 29.

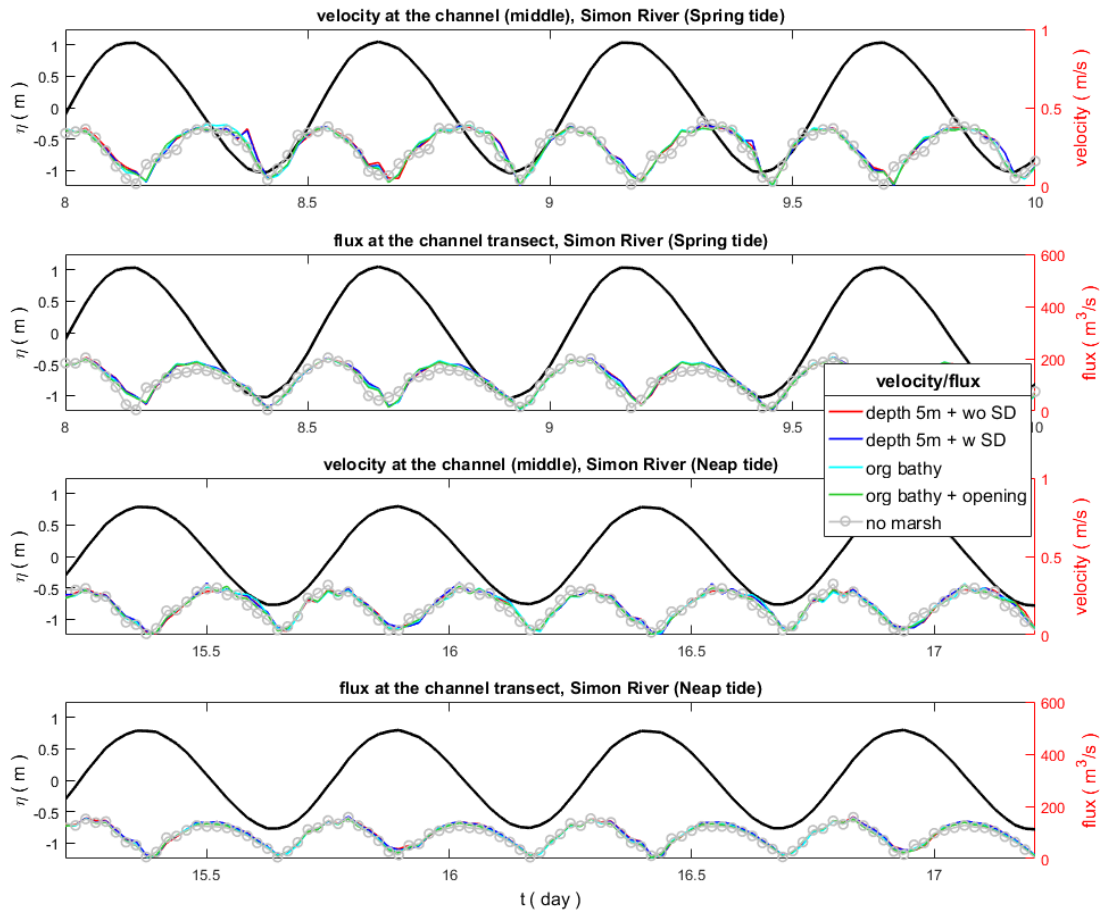


Figure 35: Along channel velocity and volume flux (in  $\text{m}^3/\text{s}$ ) going in/out through Simon River inlet for different morphological scenarios. First subplot shows along channel velocity magnitude at the middle of the inlet during a spring tide and the second subplot represents the corresponding volume flux through the entire inlet. Remaining third and fourth subplot displays similar velocity and flux magnitude during a neap tide. Surface elevation from a Simon River inlet model grid point (referenced to NAVD88, in meters) is shown with the solid black line (label provided on the left side). Velocity and flux magnitude, and surface elevation are plotted together to identify the asymmetry during flood and ebb tide. Detailed description about the figure legend is given in Figure 29.

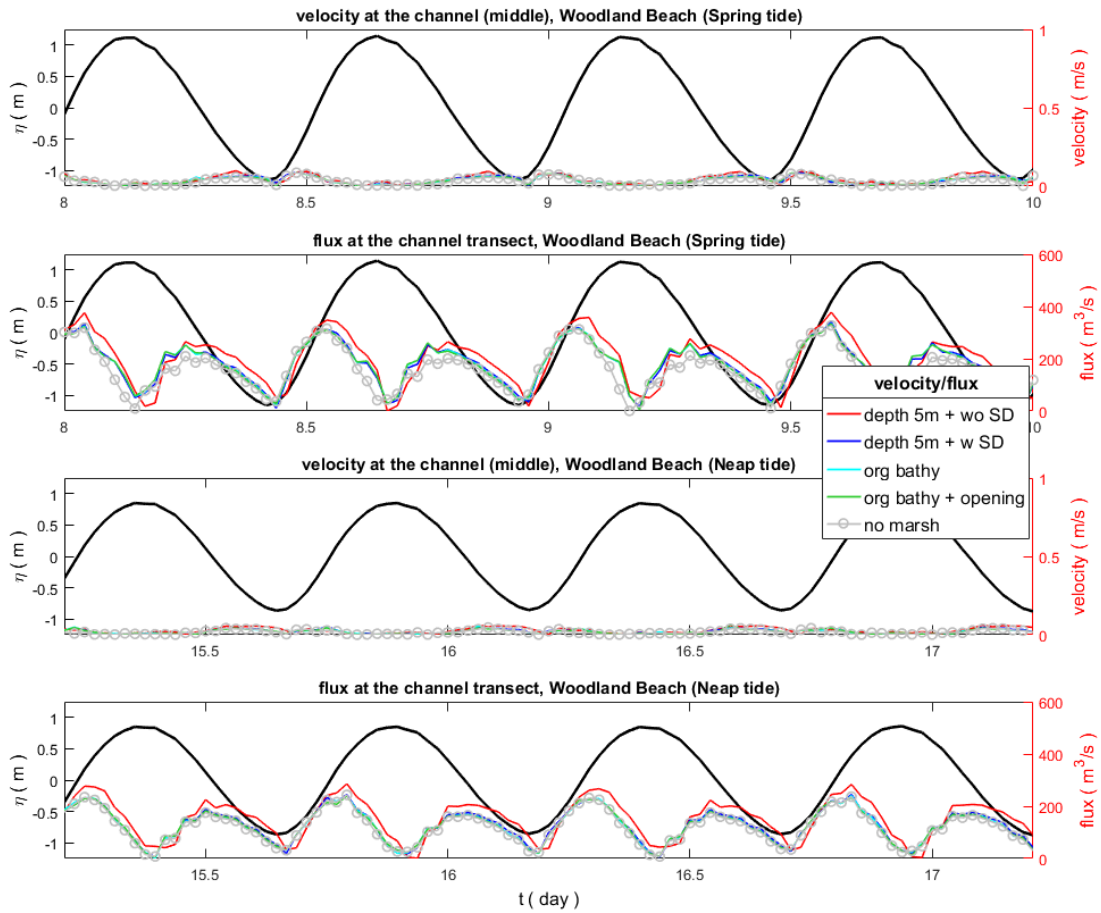


Figure 36: Along channel velocity and volume flux (in  $\text{m}^3/\text{s}$ ) going in/out through Woodland Beach inlet for different morphological scenarios. First subplot shows along channel velocity magnitude at the middle of the inlet during a spring tide and the second subplot represents the corresponding volume flux through the entire inlet. Remaining third and fourth subplot displays similar velocity and flux magnitude during a neap tide. Surface elevation from a Woodland Beach inlet model grid point (referenced to NAVD88, in meters) is shown with the solid black line (label provided on the left side). Velocity and flux magnitude, and surface elevation are plotted together to identify the asymmetry during flood and ebb tide. Detailed description about the figure legend is given in Figure 29.

### 5.1.3 Scenario 2: Reduced channel depth with Sluice Ditch open

For this scenario, Sluice Ditch is reintroduced into the bathymetry of scenario 1 (with the limitation to 5m depth). The total instantaneous flux going in or out of the entire wetland becomes more symmetric during both spring and neap conditions, indicating a loss of the flood dominance seen in the most restricted example of Scenario 1 (Figure 29). Response at the Leipsic River, Simon River and Woodland Beach inlets remains similar to the previous case with Sluice Ditch closed (Figures 31-33 and 35 - 36). However, the newly opened Sluice Ditch inlet shows new ebb dominance that is in opposition to the previous dominant behavior of the system (Figure 34).

Figures 37 and 38 show spatial maps of tidal range and maximum velocity magnitude on the channels and mudflats for the scenarios considered. The opening of Sluice Ditch has a pronounced effect on tidal range in all areas of the system aside from those most adjacent to the Leipsic and Simon River entrances, with the tide range doubled in some instances along Duck Creek and at the entrance into Money Marsh. In contrast, the opening reduces the maximum velocity in some instances, but can flip the orientation of that velocity and thus affect the overall flood/ebb dominance or direction of transport within the marsh system. In this scenario, the system has two ebb dominant channels and is thus more prone towards exporting sediment on average.

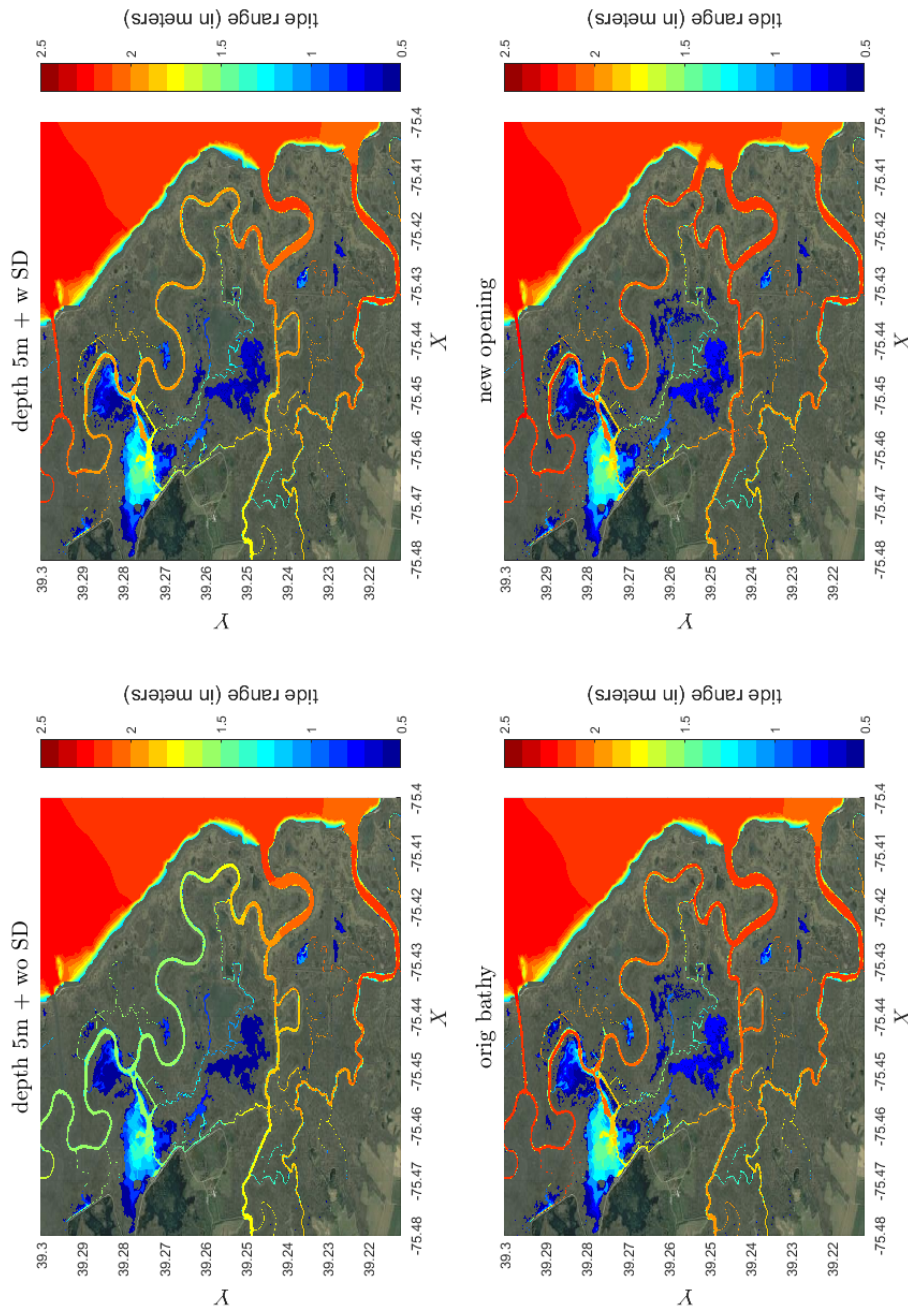


Figure 37: Changes in the tidal range (referenced to NAVD88, in meters) in BHNWR due to different morphological scenarios.

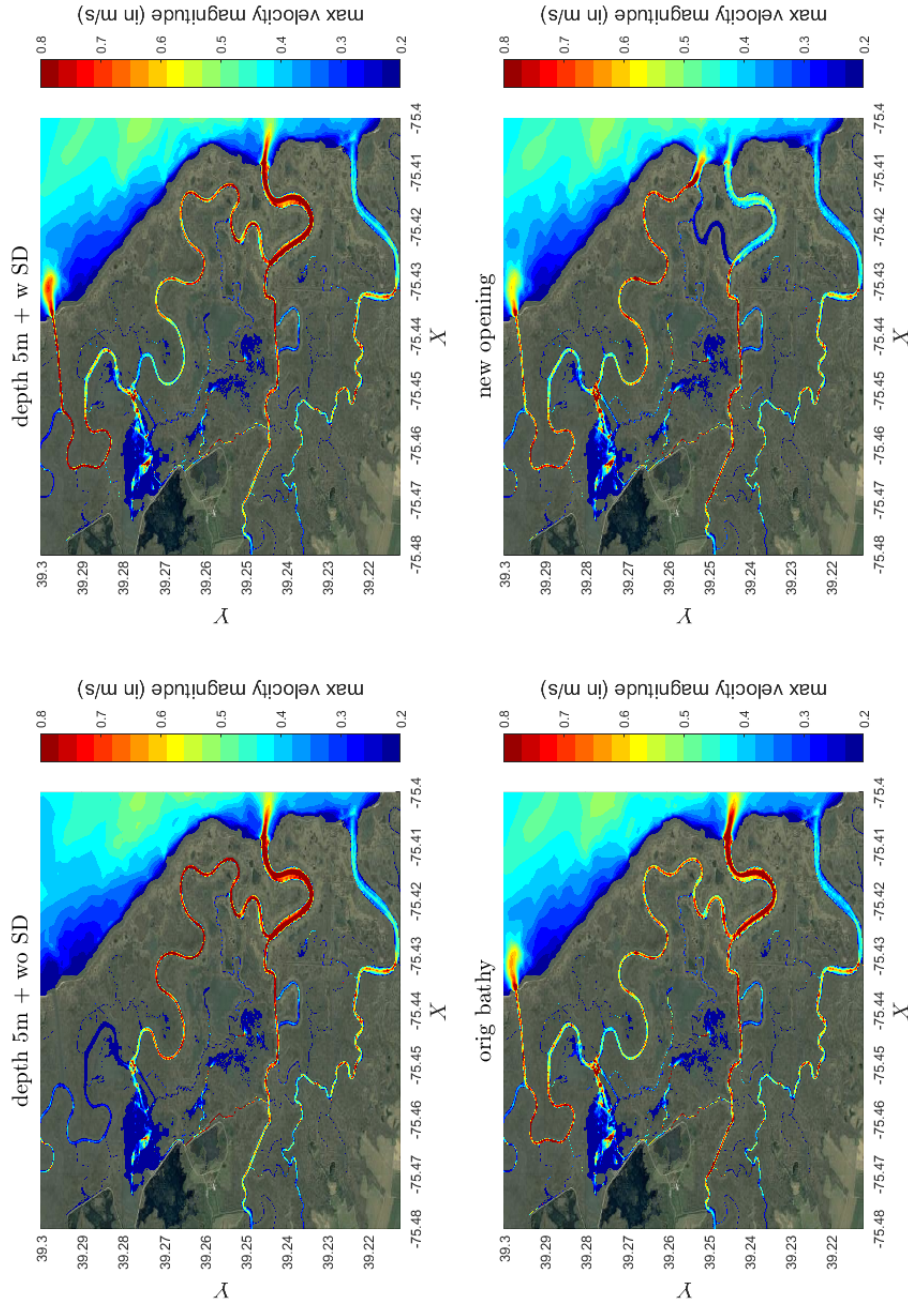


Figure 38: Changes in the maximum velocity magnitude (in m/s) in BHNWR due to different morphological scenarios.

#### 5.1.4 Scenario 3: Future opening of a connection between Duck Creek and Delaware Bay

We next consider the effect of the opening of a new entrance along Duck Creek due to progress shoreline erosion on the bay shoreline (Figure 28). The net flux going in/out of the wetland seems to remain unchanged from the estimate with present morphology (Figure 29), with about the same degree of spring tide asymmetry. However, hydrodynamics in the Leipsic River changes dramatically. Velocity and flux through Leipsic River is reduced by almost half during both spring and neap tide (Figures 31 - 33). Surprisingly, this new opening has a minimal influence on the other three inlets. From the spatial distribution shown in Figure 36 - 37 we can see that the tidal prism has increased slightly, while the velocity magnitude decreases significantly in the Leipsic River and in the stretch of Duck Creek connecting the Leipsic River to the new entrance. The new entrance is seen to divert the majority of the Duck Creek flow that originally passed through the Leipsic River entrance, leading to a dramatic reduction in maximum velocities in the Leipsic River itself.

Figures 39 and 40 show the instantaneous volume flux and velocity in each of the five open inlets in scenario 3. Volume flux through the new opening is comparable to flux in the Leipsic River, and the flux in either case is reduced to a value comparable to that of the Simon River during flood stage. The new entrance, along with the Leipsic River and Sluice Ditch, remain ebb dominant, however.

## 5.2 Erosion and net sediment transport

Sediment transport calculations were carried out for all scenarios using the 3D model described in section 4.1. Figure 41 shows the instantaneous sediment flux in or out of the

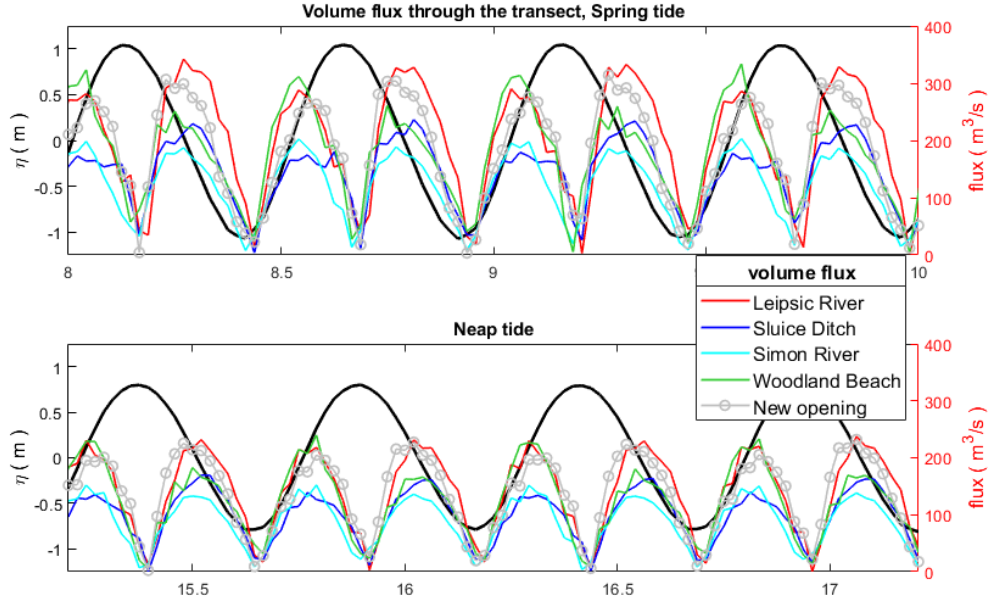


Figure 39: Total volume flux (in  $\text{m}^3/\text{s}$ ) through each inlet in scenario 3, with a new entrance on Duck Creek.

entire system, while Figure 42 shows the tidally-averaged net flux for each scenario. Our preliminary model results indicate that there is a net export of sediment to the Bay due to the ebb dominant tidal asymmetry in BHNWR system. Starting from the scenario 1 configuration, we see a slight increase in net export of sediment with the opening of Sluice Ditch, followed by a gradual drop in net export in the deeper present-day system. All three of these conditions indicate a tendency towards sediment export from the system, which would have been a destabilizing influence over time. It is possible that a more historically accurate scenario with narrower channels and the absence of mud flats in portions of the marsh that have collapsed would reduce this tendency, as it is unlikely that the marsh would have successfully evolved in place while continually exporting sediment to the Bay, which serves as the primary available source.

Surprisingly, scenario 3 with a new opening shows a dramatic drop in sediment export,

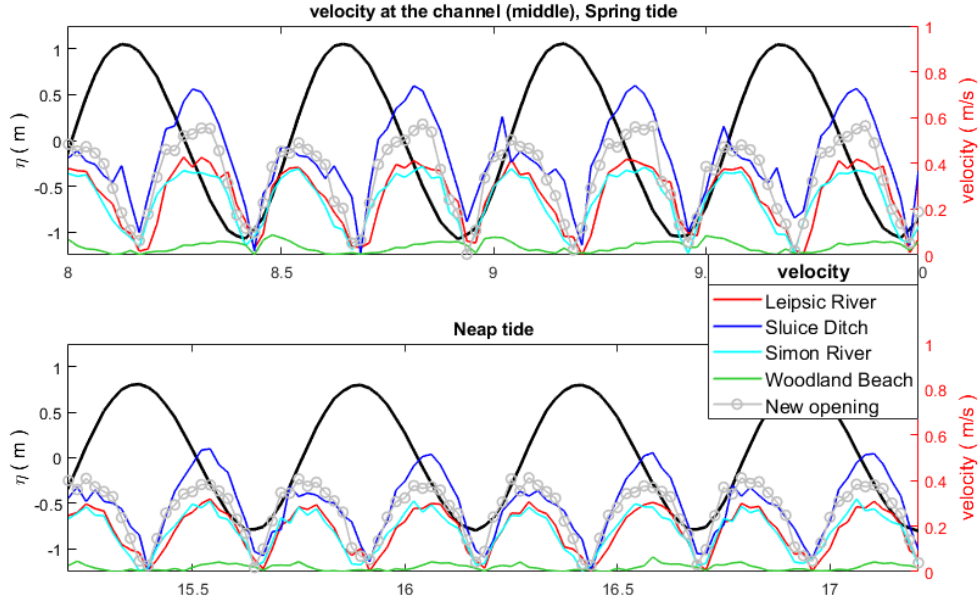


Figure 40: Centerline velocity (m/s) in each inlet in scenario 3, with a new entrance on Duck Creek.

with volume flux values reduced by almost half in comparison to present conditions. This is more evident from Figure 32 of Leipsic River inlet where the velocity magnitude with the new opening becomes half of one with the present morphology. Figure 43 represents the spatial map of maximum sediment concentration in BHNWR channels and mudflats. Sluice Ditch introduces a new plume to the system and we have net export through both Leipsic River and Sluice Ditch inlets. As the depth increases the maximum erosion at different parts of BHNWR and concentration of the sediment in both the plumes decreases. Moreover, the new opening weakens net export significantly by reducing erosion further. From the time averaged sediment flux plot (Figure 42) we can see that the residual transport is much smaller than predicted for the present-day scenario.

Figures 44 - 47 show the instantaneous sediment flux through each of the original four inlets for each of the scenarios considered. The change in configuration significantly reduces

sediment flux in the Leipsic River, to a maximum value approximately 1/3 of that under present conditions. Changes are less pronounced in the other inlets, as expected. The temporal distribution of sediment flux remains ebb dominant in all scenarios in each of the inlets, which, again, could be due to an underestimation of available sediment in the Bay during flood conditions.

Finally, Figure 48 shows the distribution of sediment fluxes through all inlets in scenario 3, and shows that the new inlet is the largest conduit of sediment flux, exceeding the contribution from the Leipsic River by roughly a factor of two, and remaining ebb dominant in neap tide conditions. This result is likely due to an ongoing, rapid adjustment of morphology in the newly opened entrance, which may adjust to a configuration different from what was initially specified over a reasonably short period of time.

Figures 44 - 47 show the instantaneous sediment flux through each of the original four inlets for each of the scenarios considered.

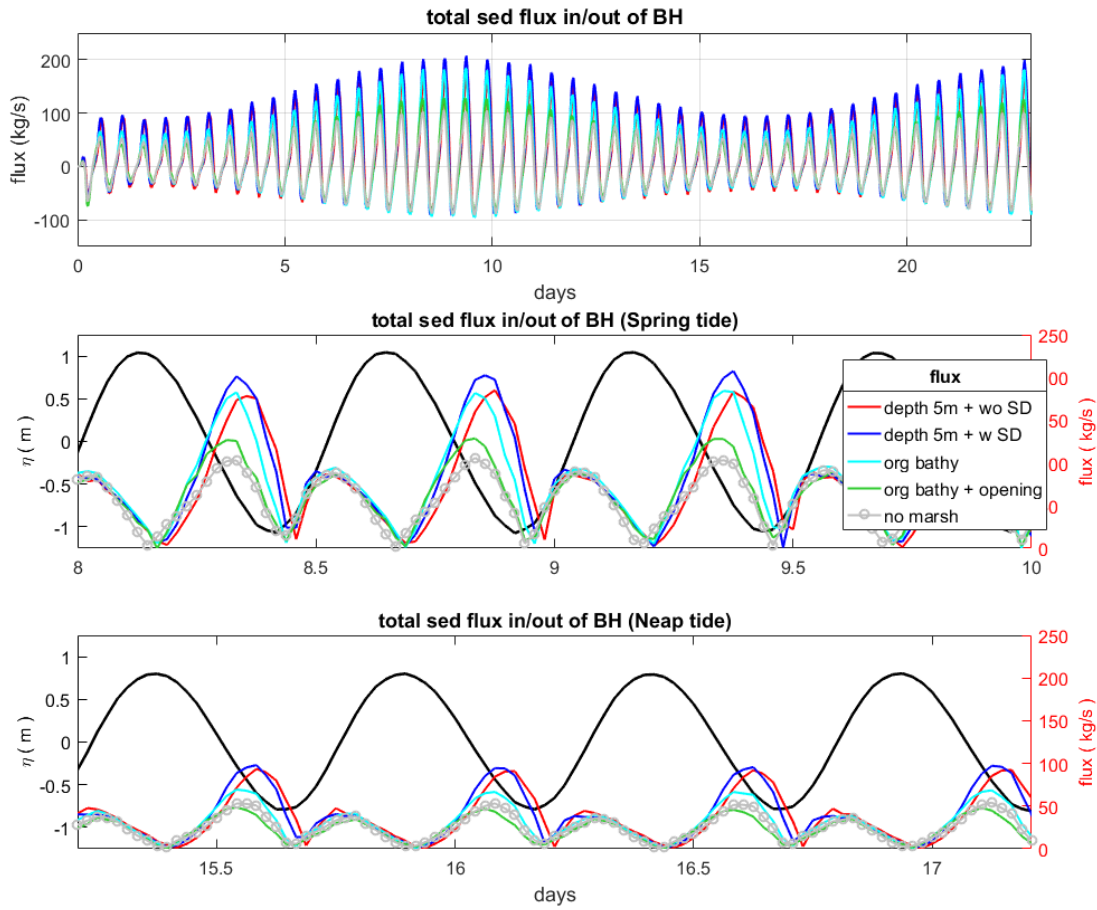


Figure 41: Total sediment flux (in kg/s) going in/out of BHNWR for different morphological scenarios. First subplot shows total flux for the entire spring-neap cycle used for model run (here, positive flux represents going out from the wetland, negative represents going in). The second and third subplot represents total flux magnitude separated into a spring and neap tidal cycle respectively (label provided on the right side). Surface elevation from a Leipsic River inlet model grid point (referenced to NAVD88, in meters) is shown with the solid black line (label provided on the left side). Flux magnitude and surface elevation are plotted together to identify the asymmetry during flood and ebb tide.

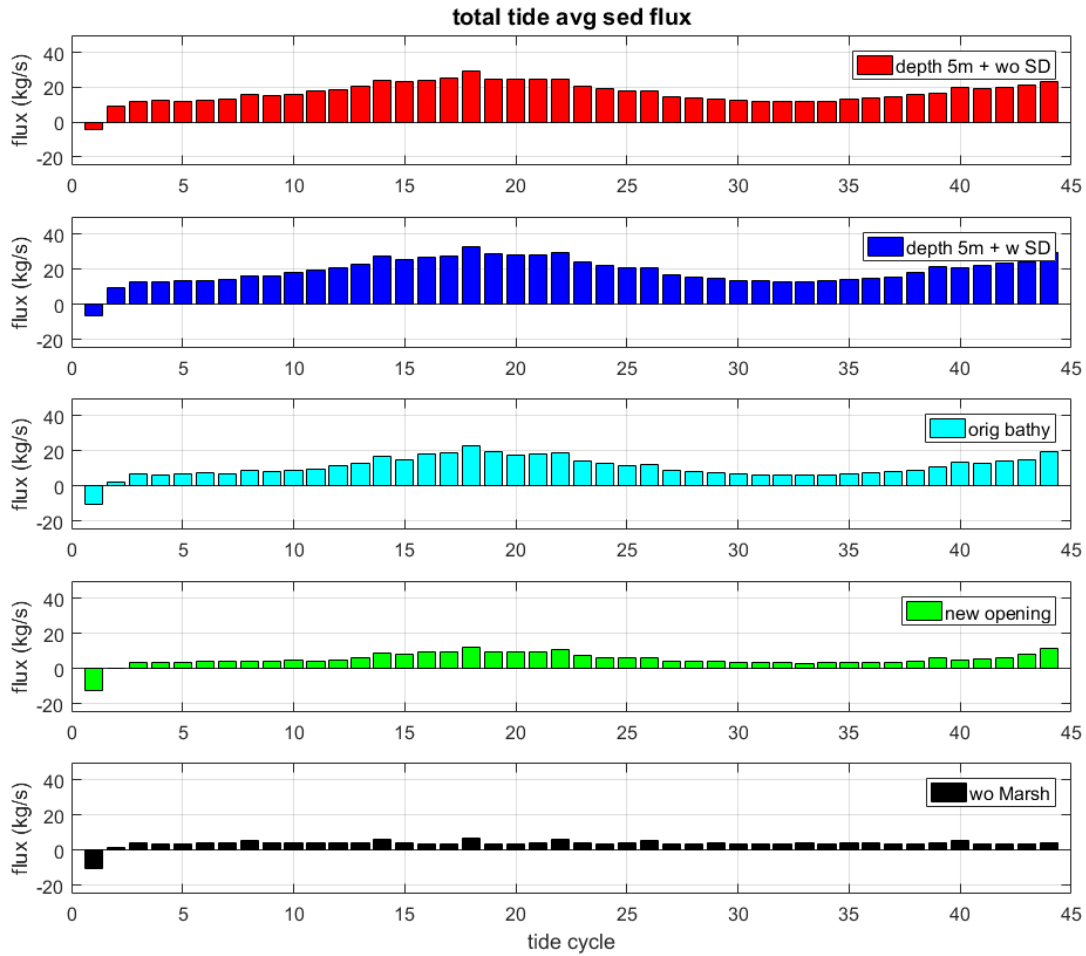


Figure 42: Tide averaged sediment flux/residual transport (in kg/s) going in/out of BH-NWR for different morphological scenarios. The wave averaging is done by applying zero-upcrossing method on the surface elevation data from Leipsic River inlet model grid point. Detailed description about the figure legend is given in Figure ??.

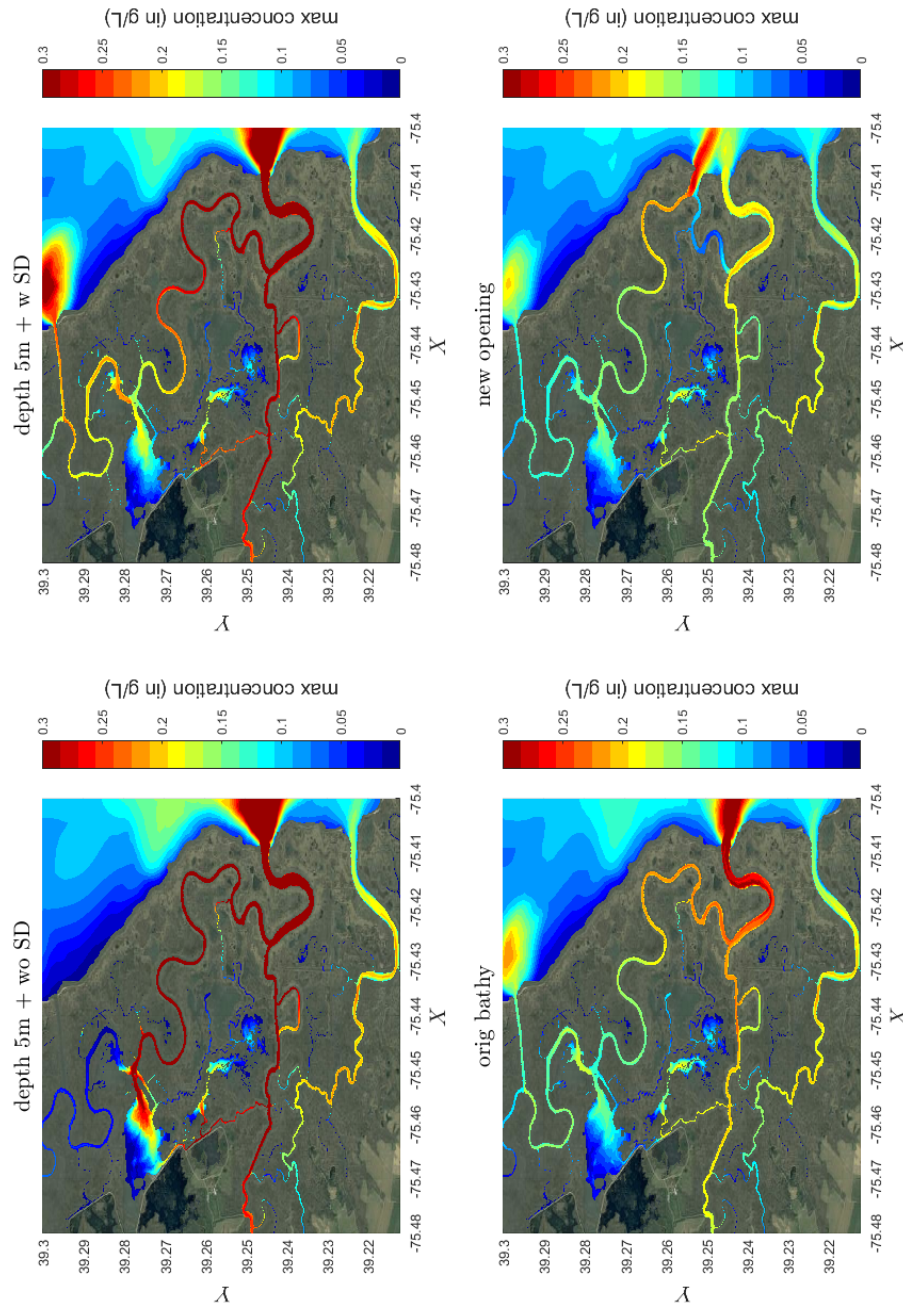


Figure 43: Changes in the maximum sediment concentration (in g/L) in BHNWR due to different morphological scenarios.

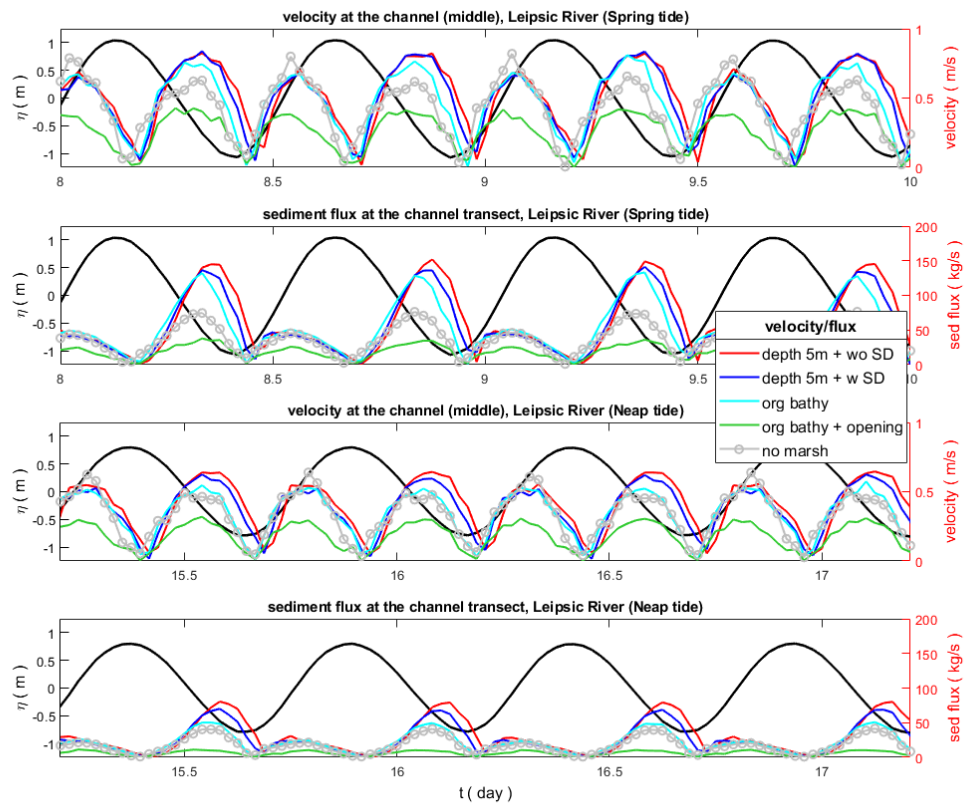


Figure 44: Total sediment flux (in kg/s) during spring and neap tide conditions in the Leipsic River for each of the scenarios considered.

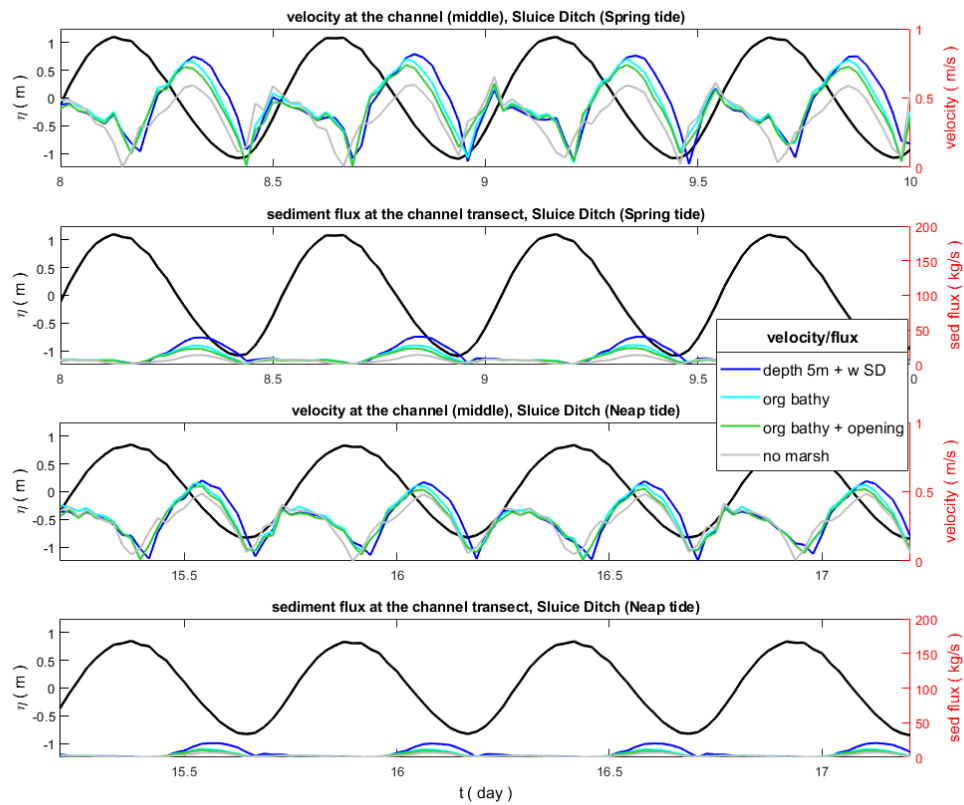


Figure 45: Total sediment flux (in kg/s) during spring and neap tide conditions in Sluice Ditch for each of the scenarios considered.

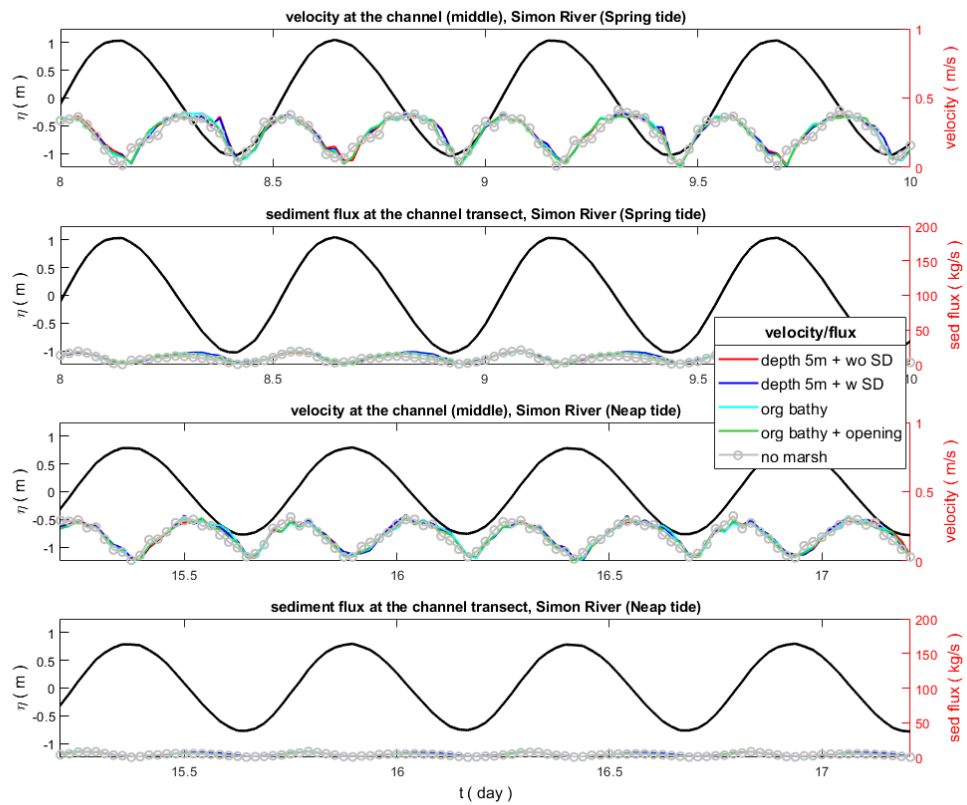


Figure 46: Total sediment flux (in kg/s) during spring and neap tide conditions in the Simon River for each of the scenarios considered.

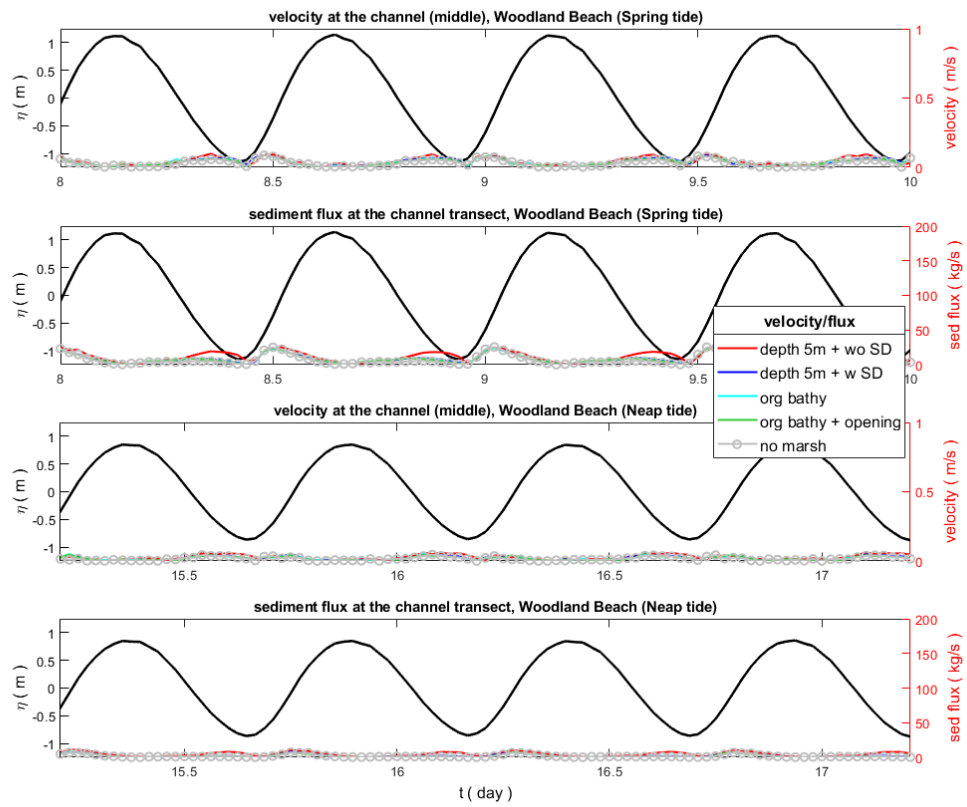


Figure 47: Total sediment flux (in kg/s) during spring and neap tide conditions in the Woodland Beach entrance for each of the scenarios considered.

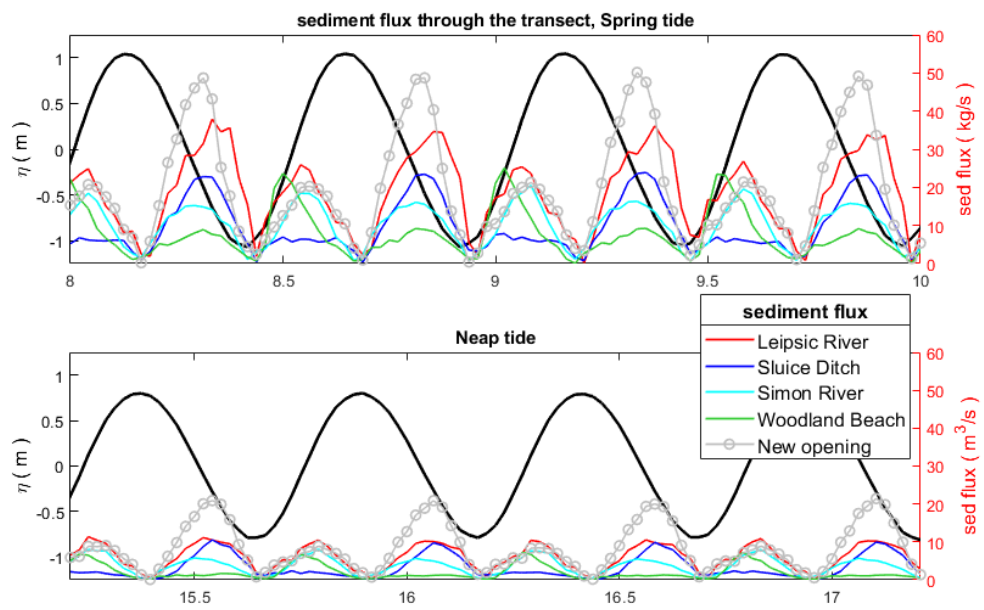


Figure 48: Sediment flux (in kg/s) during spring and neap tide conditions in the each entrance for scenario 3.

## 6 Wind waves on the Money Marsh mudflat

Salt marsh degradation is often thought to be connected to erosion and collapse of marsh shorelines due to wave erosion. Potentially, erosive effects from wind waves, in regularly flooded flats, is responsible for collapse of marsh platform and formation of variably-inundated tidal mud flats. The edge erosion would lead to enlargement of mud flats in the long term. The dynamics taking place at the boundary between salt marsh and tidal flat is of significant importance, where marsh vegetation, elevation of the tidal flat and fetch distance largely influence the wave energy and erosion rates. Money Marsh, a growing tidal mudflat, is located inside the Bombay Hook National Wildlife Refuge. It has undergone significant degradation over the last 50 to 75 years and is now about 1 km in extent in all directions, large enough to experience effects of fetch-limited wind wave growth. The presence of a significant wave climate potentially accelerates marsh shoreline erosion.

In this section, we describe an ongoing study of wave climate in Money Marsh mudflat and the influence of wave action on marsh boundaries. The study employs wave data analysis and numerical modeling in an effort to estimate the long term potential for wind wave-driven shoreline erosion and resulting enlargement of the tidal flat. Wave modeling has been carried out using the SWAN model (Booij *et al.*, 1999a), to examine wave growth in both idealized and observed conditions, and compared with a fetch limited wind wave model (Young & Verhagen, 1996a,b) to evaluate the effect of fetch distances. The SWAN model is shown to predict a reasonable estimate of spatially varying wave period and height at field measurement locations, and is thus potentially useful as a tool for quantifying shoreline wave climate.

The collection of pressure data used in this section is described in section 2 of Deb *et al.* (2018).

## 6.1 Instrument location

In-situ measurement of pressure fluctuation caused by moving water surface is essential in reconstructing the surface displacement time series in shallow water. There are two parts of the pressure under water, mainly hydrostatic pressure and pressure caused by the waves. In this study, we use two subsurface pressure sensors (RBRsolo D wave) deployed on the tidal flat to continuously record tidal elevation and superposed short wind waves at a frequency of 16 Hz. Atmospheric pressure collected at the same time is removed from the raw data to get pressure due to water waves only. Also, we collected data from another tide gauge (RBRsolo D tide) deployed at Leatherberry mudflat to describe the time varying water level in our non-stationary SWAN model simulations. Geographic location of the sensors is shown in Figure 49. The RBR1 sensor is on the shallower side of the tidal flat, where the bed elevation is at -0.2 m NAVD88. The RBR2 sensor is on the northern side at a slightly lower bed elevation of -0.8 m NAVD88. Both sensor locations are influenced by the wetting and drying effects from a tidal range of 2.0 m and measure only atmospheric pressure during a low tide.

## 6.2 Data processing and extraction of wave signal

The description of the RBR Solo D instruments and the collection of data is described in section 2 of [Deb \*et al.\* \(2018\)](#). The collected data is first corrected for bad points, and linear interpolation is used to replace missing values. Then, barometric pressure is removed from the corrected data to retain only the subsurface pressure. Figure 50 shows the raw pressure data collected from sensors deployed on the Money Marsh mudflat.

Then, a linear trend is constructed for each sequential 15 minute segment of data in order to obtain a smoothed record of tidal elevation. (This was relatively difficult to do using

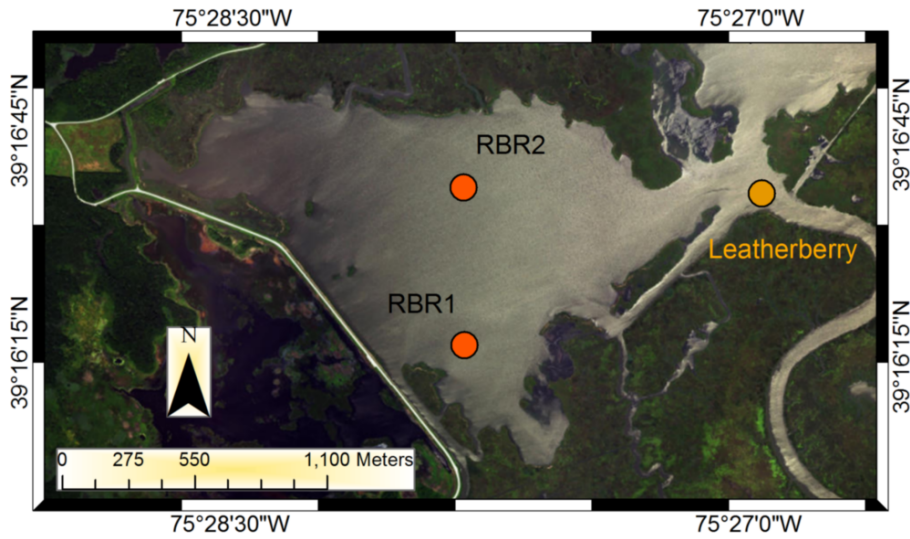


Figure 49: Pressure gauges in the tidal flat

Fourier analysis, due to the data segments where the instruments are simply measuring air pressure. The linear trends are then subtracted from the subsurface pressure data, leaving what is assumed to be the signal related to surface waves. An example segment of pressure signal separated into tidal and wave components is shown in Figure 52.

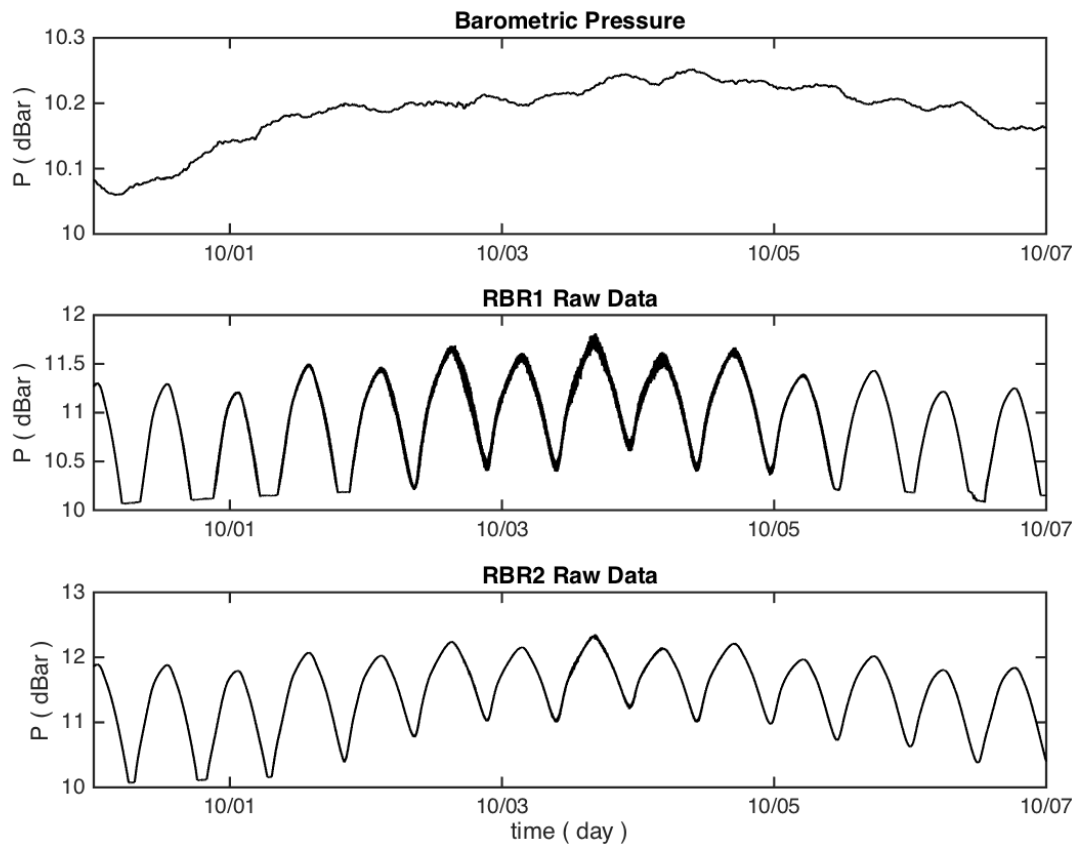


Figure 50: Barometric pressure and raw pressure data (dBar) collected from the RBR gauges

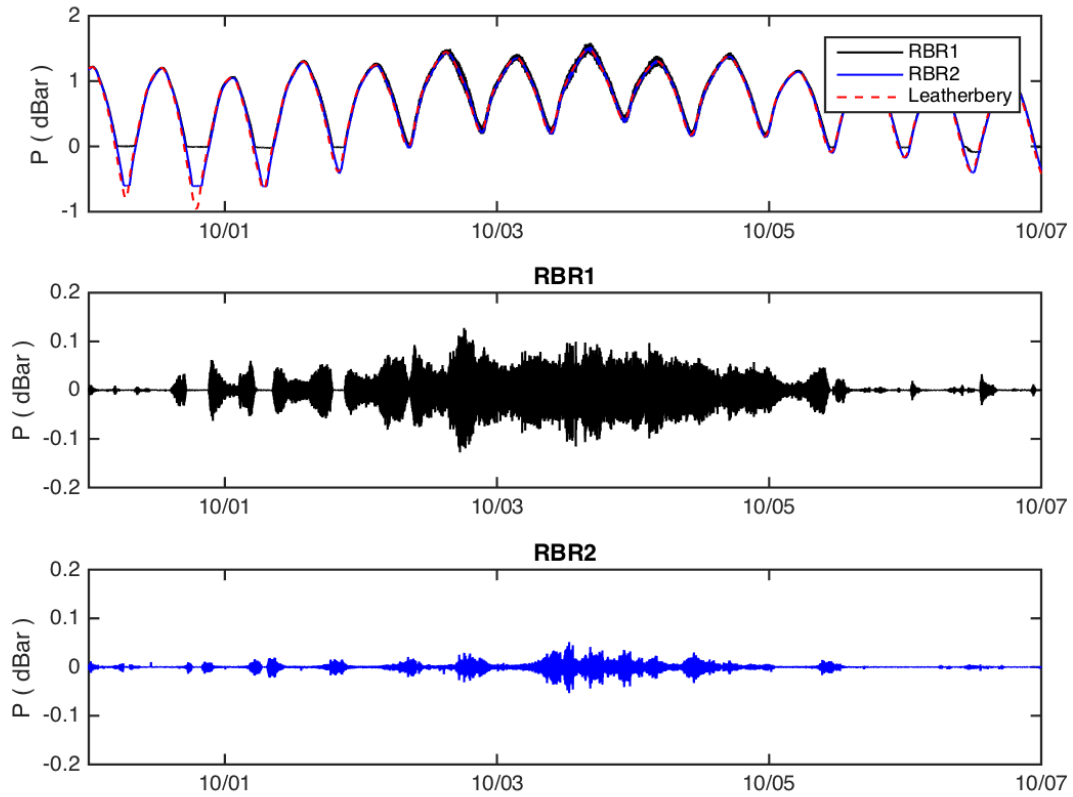


Figure 51: Pressure data (dBar) collected from the gauge excluding barometric pressure. First subplot represents the pressure data for long waves and the last two illustrates wind waves at different locations

### 6.2.1 Pressure to surface conversion

The conversion of the high frequency pressure signal to a representative water surface elevation requires the use of a theoretically-based transfer function. Here, we use a conversion based on linear, intermediate depth wave theory (Dean & Dalrymple, 1991). The total pressure is separated into static and dynamic parts, where here the static part represents the slowly-varying tidal signal which has already been removed, and the dynamic part is assumed to represent surface waves. For a single monochromatic, progressive wave, the total pressure is given by

$$P(x, z, t) = -\rho g z + \rho g a \frac{\cosh k(h+z)}{\cosh kh} \cos(kx - \omega t) \quad (22)$$

where  $x$  and  $z$  are horizontal and vertical position (with  $z = 0$  taken to correspond to the position of the tidal inundation in each 15 minute data segment),  $t$  is time,  $h$  is water depth (or the height of the tidal water surface above the bottom at the gauge location),  $a$  is amplitude,  $g$  is gravitational acceleration, and  $\omega = 2\pi/T$  and  $k = 2\pi/L$  are angular frequency and wavenumber (with  $T$  and  $L$  being the wave period and wavelength), related by

$$\omega^2 = gk \tanh kh \quad (23)$$

We normalize pressure by the specific weight in order to get a pressure expressed as a length. For a sinusoidal wave and a bottom-mounted gauge, we can then write the dynamic pressure as

$$\frac{P}{\rho g} = a_p \cos(kx - \omega t) = \frac{a}{\cosh kh} \cos(kx - \omega t) \quad (24)$$

which shows how the pressure signal is attenuated with increasing depth relative to a given surface wavelength. We write this as

$$a_p = K_p a \quad (25)$$

where  $K_p$ , the pressure response factor, is given by

$$K_p = \frac{1}{\cosh kh} \quad (26)$$

In practice, the wave field consists of components covering a range of frequencies, with the pressure response factor  $K_p(\omega, h)$  determined from (23) and (26). The pressure response factor is depth and frequency dependent. So, the compensation needs to be carried out in the frequency domain, instead of the time domain. The standard procedure for carrying out the conversion is based on Fourier transforms, discussed in the next section. When  $kh$  is large,  $K_p$  tends to become very small eventually making the transfer function very large for high frequency waves. This can lead to undesirable amplification of the pressure signal that consists white noise. So, in this study we have restricted the pressure response factor up to a value 0.01 and neglected any higher frequencies from the total analysis that can lead to a smaller value.

Using the water depth for the data segment, we calculate wave numbers for individual frequencies following the approximation provided by Eckart (1952). The wave number at each frequency and water depth is then used to compute the pressure response factor  $K_p(\omega, h)$ .

Examples of the variation of  $K_p$  with absolute frequency  $f = \omega/2\pi$  are shown in Figures 52 and 53. The pressure response factor has a value of 1.0 in the low frequency limit, and then decreases with increasing frequency, with the drop-off being more rapid for larger water depths.

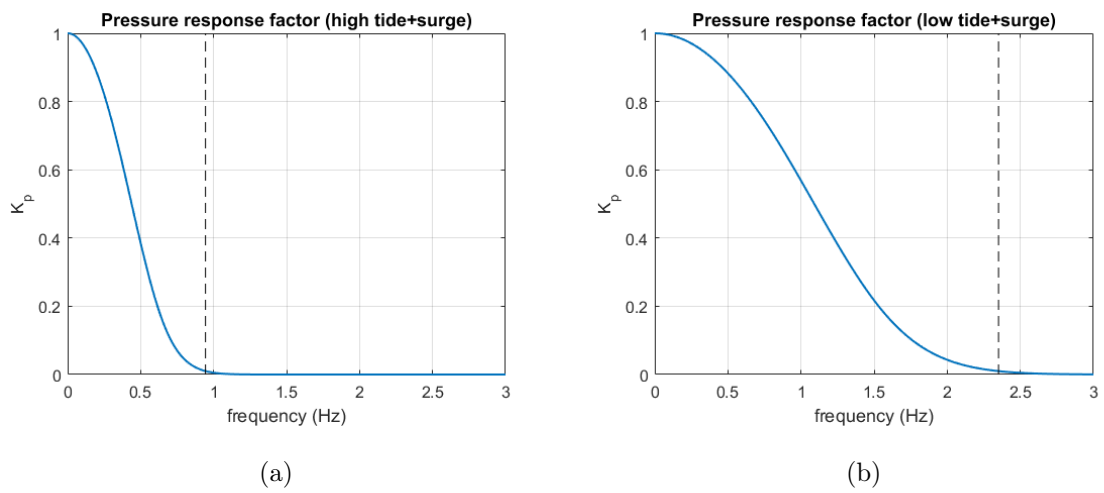


Figure 52: (a) Pressure response factor  $K_p$  at RBR1 location during a storm event & high tide (b) same storm event & low tide. Here, the dashed line represents maximum frequency taken into account based on the pressure response factor value 0.01.

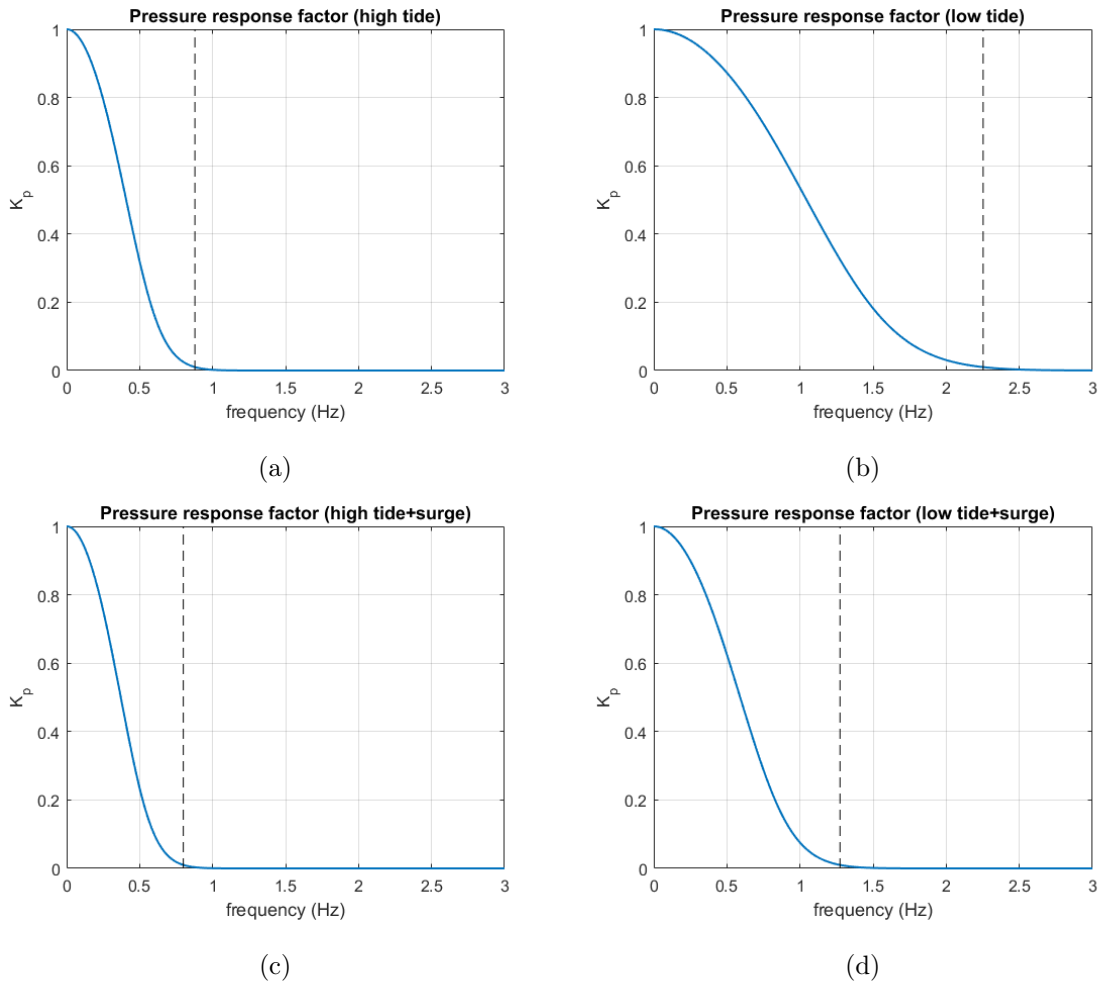


Figure 53: a) Pressure response factor  $K_p$  at RBR2 location during high tide (b) during low tide (c) during a storm event & high tide (d) same storm event & low tide

### 6.3 Wave data analysis

We now describe the processing of wave data for each 15 minute data sample. The 15 minute segment is divided into 14 subsections of 1024 data points each. The subsection is then Fourier transformed using the FFT algorithm in Matlab. The discrete Fourier transform for an original sample  $f_j = f(t_j), t_j = j\Delta t$  is given by

$$f_j = \sum_{n=0}^{N-1} F_n e^{2\pi i \frac{nj}{N}} \quad (27)$$

where the Fourier transform coefficients  $F_n$  are given by

$$F_n = \frac{1}{N} \sum_{j=1}^N f_j e^{-2\pi i \frac{nj}{N}} \quad (28)$$

$F_n$  is the discrete Fourier transform of the function  $f_j$  and  $N$  is the number of sample points (here = 1024). The sample variance for the segment is given by

$$\sigma^2 = \frac{1}{N} \sum_{j=1}^N (f_j)^2 = \sum_{n=0}^{N-1} |F_n|^2 \quad (29)$$

The Fourier transform applied to the segment of normalized pressure data  $(P/\rho g)_j$  gives a set of Fourier coefficients  $p_n$  that represent amplitudes of individual sinusoidal modes at frequencies  $\omega_n = 2\pi n/N\Delta t$ , where  $\Delta t$  is the sampling interval. The corresponding Fourier amplitudes for the surface displacement  $\eta_j$  are then reconstructed from

$$a_n = K_{pn} p_n \quad (30)$$

and the surface is recovered from the inverse transform

$$\eta_j = \sum_{n=0}^{N-1} a_n e^{2\pi i \frac{nj}{N}} \quad (31)$$

Figure 54 shows the measured pressure head (in meters) and the reconstructed water surface for a 15 minute sampling window.

In addition to the deterministic reconstruction of the water surface for a given sample, we are also interested in constructing smoothed power spectra which give an indication of

the distribution of wave energy with frequency. We consider the wave field to be an ergodic process, for which each 15 minute sample is taken to be an independent realization of the process as seen through a 15 minute long sampling window. We define a power spectrum  $S(f)$  which is related to the signal variance by

$$\sigma^2 = \int_0^\infty S(f)df = \sum_{n=0}^{N/2} S_n \Delta f \quad (32)$$

where  $\Delta f$  is the sampling frequency of 16 Hz, and where the upper limit  $N/2$  is imposed by the Nyquist limit. This can be compared to (29) to immediately give an estimate of  $S_n$  in terms of the  $F_n$  Fourier coefficients. In order to provide smoothing, we use Welch's method and construct an averaged estimate of the frequency-by-frequency according to

$$\overline{|a_n|^2} = \frac{1}{N_s} \sum_{n_s=1}^{N_s} (|a_n|^2)_{n_s} \quad (33)$$

where  $n_s$  denotes an individual 15 minute sample and  $N_s$  is the number of samples (here 14). Comparing (29) and (32) then gives the spectral estimate

$$S_n = 2\overline{|a_n|^2}/\Delta f = 2N\Delta t\overline{|a_n|^2} \quad (34)$$

where the factor of 2 arises from wrapping the positive and negative frequency components onto the positive frequency axis.

For our analysis, we use a cutoff frequency for surface spectra based on  $K_p$  value of 0.01, and reconstructed all the energy density beyond that cut-off frequency following the shape of a TMA spectrum (Bouws *et al.*, 1985) in order to avoid over-amplifying contributions from the noise at higher frequencies (Young & Verhagen, 1996b).

The spectral information is then represented in terms of spectral moments in the frequency domain as

$$m_n = \int_0^\infty f^n S(f)df \quad (35)$$

The zero-order moment ( $m_0$ ) represents the area under the spectra, which is the variance of the sea surface elevation. We can compute the zero-moment wave height from the wave spectrum and it is equivalent to the significant wave height ( $H_{1/3}$ ) for a narrow banded sea.

$$H_{m0} = 4.004\sqrt{m_0} \quad (36)$$

The peak period  $T_p$  corresponds to the frequency of the spectra representing highest concentration of energy,

$$T_p = \frac{1}{f_p} \quad (37)$$

Likewise, we can calculate the mean wave period from

$$T_{m01} = \frac{m_0}{m_1} \quad (38)$$

and the average zero-up-crossing period,

$$T_{m02} = \sqrt{\frac{m_0}{m_2}} \quad (39)$$

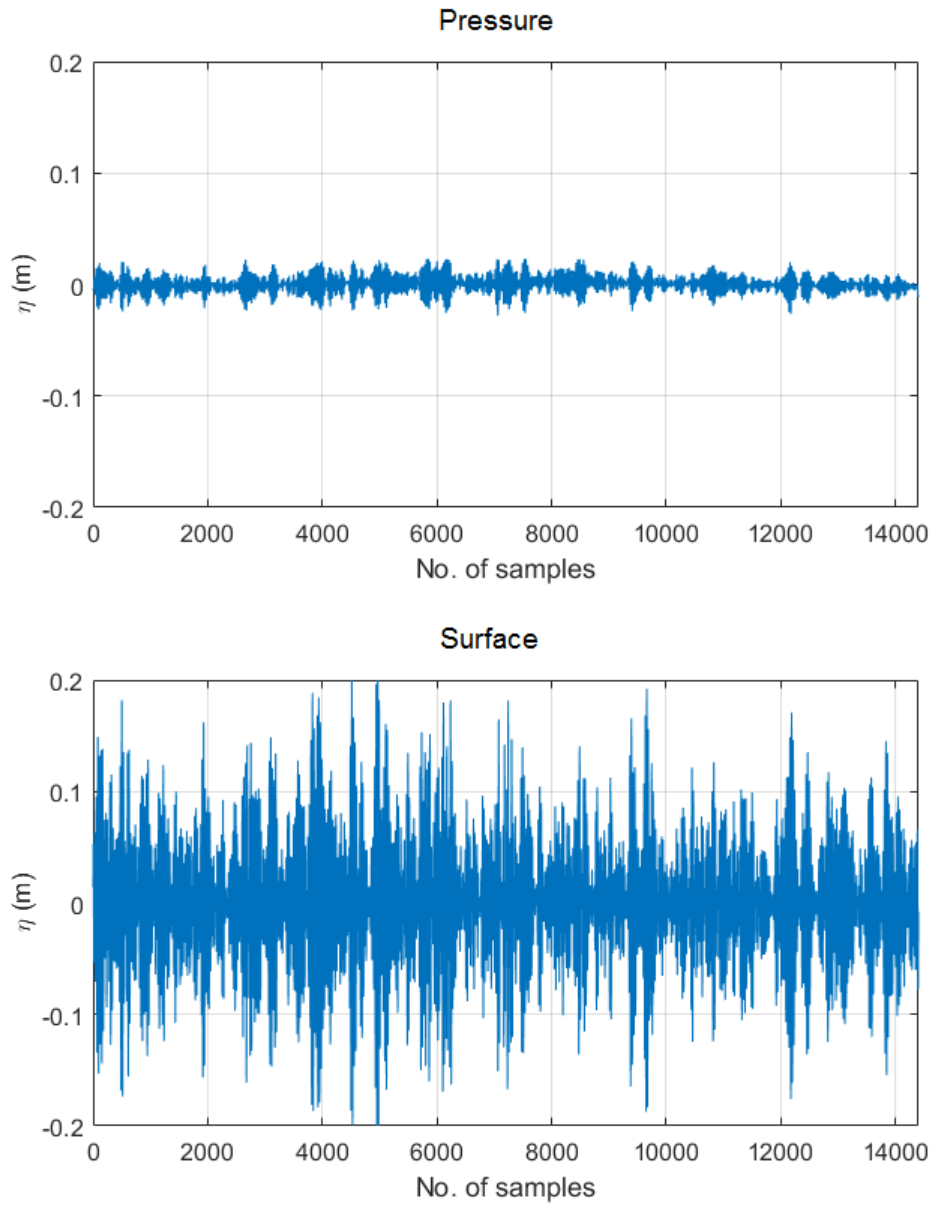


Figure 54: Pressure head and the surface elevation (in meters) using  $K_p$

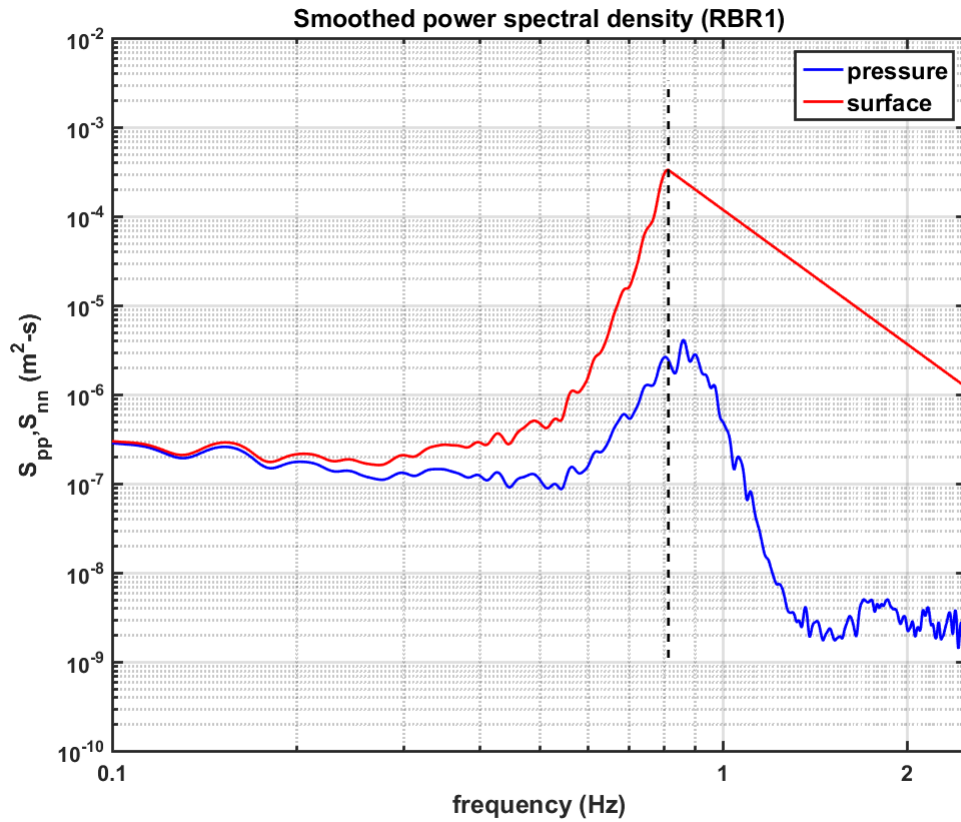


Figure 55: Smoothed spectral estimate obtained using Welch's method at RBR1 for pressure head (in blue) and corrected surface elevation (in red). Tail of the spectrum is reconstructed following the shape of a TMA spectrum.

## 6.4 Spectral wave model SWAN

### 6.4.1 Model background

The Simulating Waves Nearshore (SWAN) (Booij *et al.*, 1999b; Ris *et al.*, 1999) model is a third generation discrete wave model which can estimate waves from nearshore to surf zones. SWAN has been extensively used at coastal regions with shallow water and tidal flats where most of the region is dominated by wetting and drying due to the tidal range. Ris *et al.* (1999) used SWAN at the Haringvliet estuary in Netherlands, and Gorman & Neilson (1999) used it at an estuary with large fetch and inter-tidal flat in New Zealand. Qin *et al.* (2005) used SWAN in the Delaware Bay to simulate random, short-crested wind generated waves. We used SWAN in our study area to observe the spatial and temporal variability of the wave climate due to local winds. SWAN includes several physical processes in its simulation such as refraction, wave-current interaction, depth-induced breaking, dissipation due to bottom friction and whitecapping, and non-linear interactions. SWAN solves action density equation taking the ambient current into consideration. The action density is equal to the energy density divided by the relative angular frequency,

$$N(\sigma, \theta) = E(\sigma, \theta)/\sigma \quad (40)$$

The SWAN governing equation in Cartesian coordinates is

$$\frac{\partial N}{\partial t} + \frac{\partial c_x N}{\partial x} + \frac{\partial c_y N}{\partial y} + \frac{\partial c_\sigma N}{\partial \sigma} + \frac{\partial c_\theta N}{\partial \theta} = \frac{S}{\sigma} \quad (41)$$

where  $x$ ,  $y$  are horizontal Cartesian coordinates,  $t$  is time,  $\theta$  is the propagation direction of each wave component, and  $c_x$ ,  $c_y$ ,  $c_\sigma$ ,  $c_\theta$  stand for the propagation velocity in the respective spaces.  $S$  is the energy source term, which includes the effect from generation, dissipation, and nonlinear wave-wave interaction. The first term on the left-hand side of equation 41 is

the rate of change of action density in time, the second and third terms are propagation of action in physical space. The fourth and fifth term shows shifting of the relative frequency and the refraction.

In our study, we used SWAN to evaluate the performance of spectral modeling in extremely shallow water conditions. The model results are then validated with the field data to simulate long term scenarios of the wave climate in the money marsh tidal flat. We used time varying water level and wind data to simulate model results in non-stationary conditions.

#### **6.4.2 Unstructured grid for the mudflat**

Initially, we developed two different grids, one high resolution structured grid (10 m x 10 m) consisting 40655 nodes, and a low resolution unstructured grid with 3629 nodes and 7053 elements (element size: min 7 m, max 43 m) to evaluate the efficiency of an unstructured grid. An unstructured grid with good model convergence can be very efficient and economic. Source of the bathymetry data is same as described previously in the hydrodynamic modeling section. Figure 56 shows the unstructured grid used in SWAN simulations and the grid topobathymetry.

We ran SWAN in the stationary mode with both the structured and unstructured grids using a constant wind speed and direction of 15 m/s and 30 degrees respectively. The wind direction in the analysis is basically from the North-East to South-West which limited the fetch distance to approximately 1.5 km. Comparison between the grid results are shown in the Figure 57 & 58. It is evident from Figure 58 that the unstructured grid with significantly less number of computational nodes can produce similar results and is a good choice for further analysis considering the performance and economy.

### 6.4.3 SWAN model validation with the field data

To run SWAN in a non-stationary mode with our unstructured grid we collected the time varying wind and water level data from different local sources. The water level data is available from our Leatherbery tide gauge and we updated the water level of the entire domain at each 15 minutes based on it. The dominant wind directions in the area are from the north-west and south-east sides, mainly from the Bay. In this study, the wind data has been always obtained from the closest weather station located in the Bay (Ship John Shoal, Delaware Bay Operational Forecast System). Our study area is a closed tidal flat which has no entrance for open ocean swells, and waves in the domain are all wind generated. Figure 59 & 60 represents the wind data from Delaware Bay and water level data used for SWAN model validation during a storm in our area. Model simulations are performed for 14 days using a single CPU and the serial version of SWAN 41.01. Source terms for the wave dissipation such as whitecapping, friction and breaking were taken into consideration. Detailed description about the non-linear wave generation and dissipation terms can be found in [Booij \*et al.\* \(1999b\)](#).

Dissipation due to vegetation has also been included in the analysis. Wave dissipation is expressed following the approach of [Dalrymple \*et al.\* \(1984\)](#), who modeled the vegetation effect as drag on an array of vertical rigid cylinders. Here, the energy losses are estimated based on the plant induced forces over the entire vegetation height. In SWAN, the time averaged energy dissipation rate per unit area is estimated based on the modified equation by [Mendez & Losada \(2004\)](#) for irregular waves.

$$\epsilon_v = \frac{1}{2\sqrt{\pi}} \rho \tilde{C}_d b_v N_v \left(\frac{gk}{2\sigma}\right)^3 \frac{\sinh^3 k\alpha_h + 3 \sinh k\alpha_h}{3k \cosh^3 kh} H_{rms}^3 \quad (42)$$

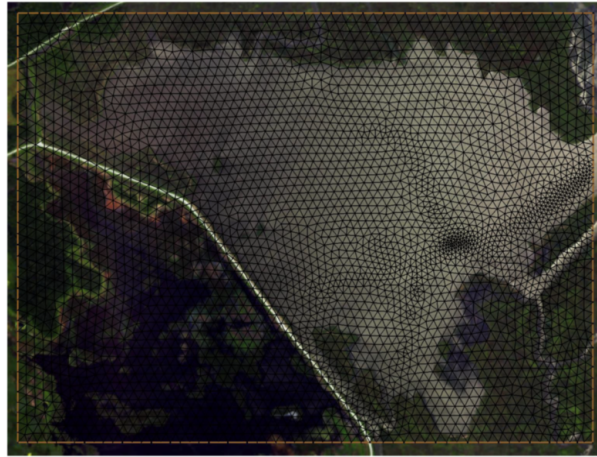
Here,  $\rho$  is the water density,  $\tilde{C}_d$  is the bulk drag coefficient that depends on the wave

height,  $b_v$  is the stem diameter of cylinder (plant),  $N_v$  is the number of plants per square meter,  $\alpha_h$  is the vegetation height,  $h$  is the water depth and  $H_{rms}$  is the root mean square wave height. In our study area, we assumed the plant diameter to be of 2.5 cm, vegetation height of 1 m, 100 plants per square meter and the drag coefficient equal to 0.2. The vegetation coverage in our area is shown in the Figure 61.

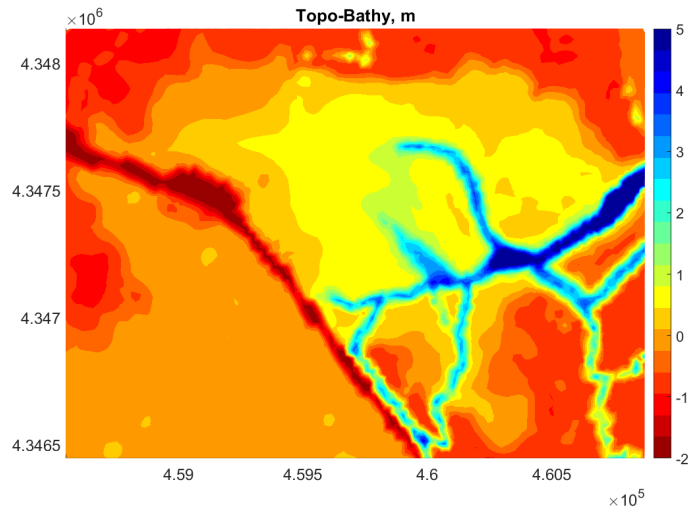
After completing our model simulations we compared the results with processed field data from two RBR wave gauge locations. We mainly prioritized comparing the significant wave height and peak wave period from model and measurement data. During the normal high tides, significant wave height and peak wave period in the domain peaks upto 0.15 m and 1 s, and there is no wave activity during low tides as most of the domain dries out. During a storm with high surge and strong gust, like our model validation case, the wave height and period increases upto 50%. Figure 62 - 65 shows the comparison between wave properties from field and model data. The BIAS, RMS and SI (scatter index) for significant wave height at both the gauges vary between 2–2.2 cm, 1–1.2 cm and 10–16% respectively. Whereas, for peak period, the error quantities ranges from  $-0.14 - 0.07$  s,  $0.07 - 0.075$  s and 5 – 7% respectively (Table 3).

Table 3: Model and observed data comparison

Location	Parameter	Bias	RMS	Scatter Index
RBR1	Hs	0.02	0.012	9.98
	Tp	0.067	0.074	7.12
RBR2	Hs	0.027	0.012	16
	Tp	-0.14	0.073	5

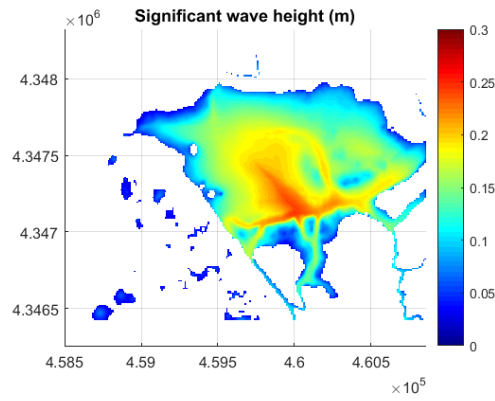


(a)

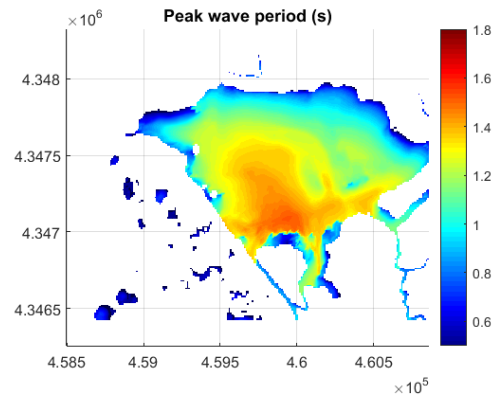


(b)

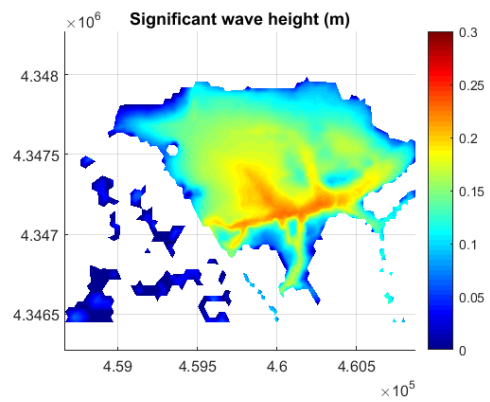
Figure 56: (a) Unstructured grid resolution (b) Topo-bathymetry of the unstructured grid (in meters) from NAVD88 vertical reference level



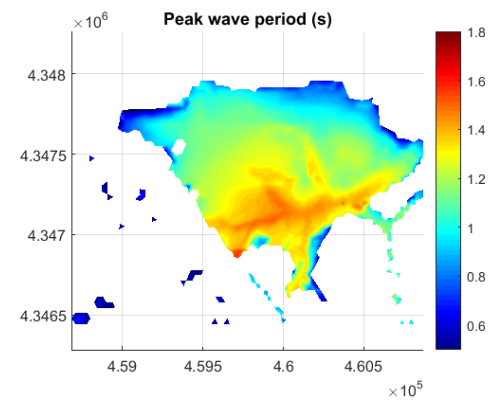
(a)



(b)

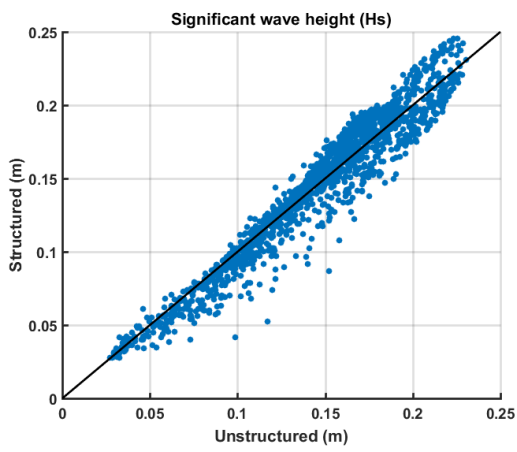


(c)

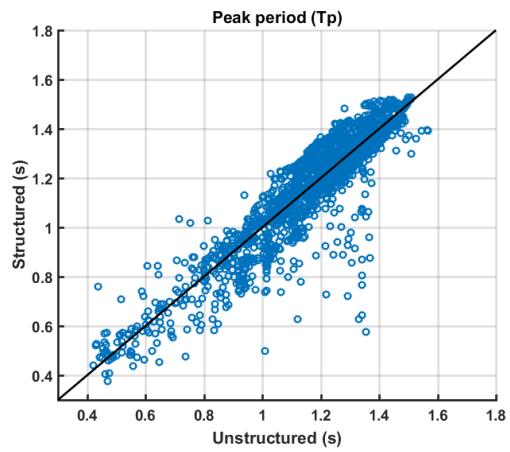


(d)

Figure 57: (a)(b) Significant wave height (in meters) and peak wave period (in seconds) for the high resolution structured grid (c)(d) Significant wave height (in meters) and peak wave period (in seconds) for the unstructured grid



(a)



(b)

Figure 58: (a) Comparison between structured and unstructured grid significant wave height (in meters). (b) Comparison between structured and unstructured grid peak wave period (in seconds).

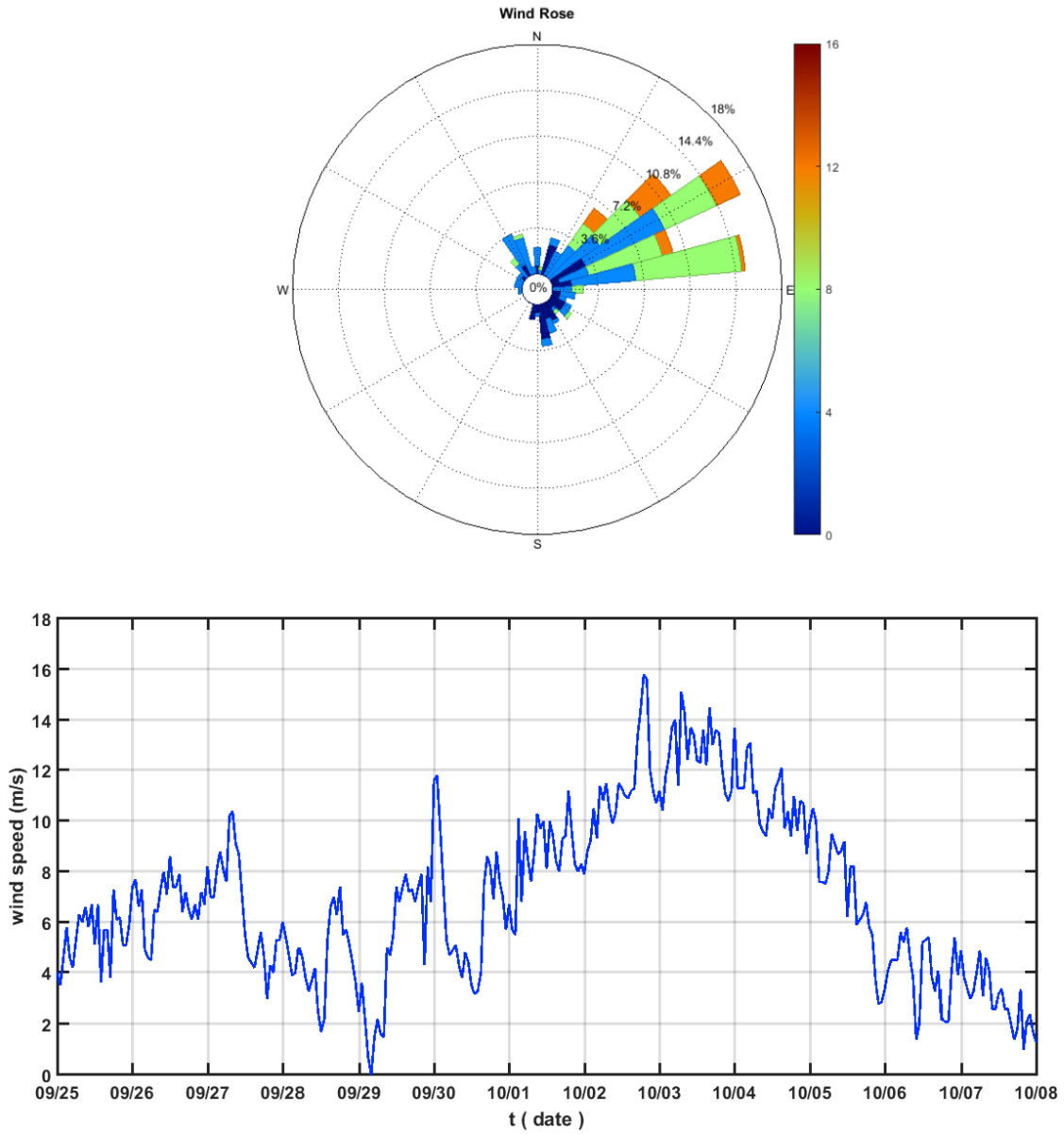


Figure 59: Wind rose diagram and wind speed at 10 m elevation (in m/s) during a storm (September 25 to October 8, 2015) at Ship John Shoal, NJ

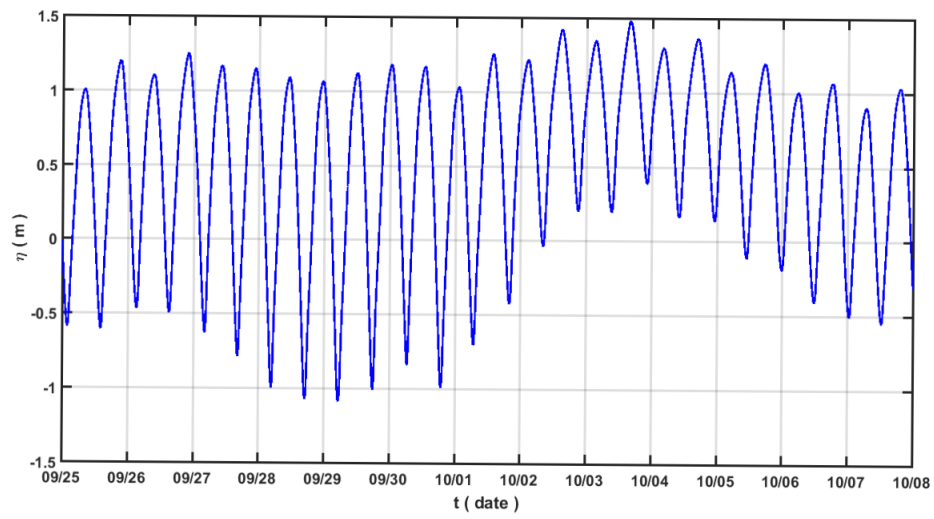


Figure 60: Water level data from Leatherbery tide gauge (in meters, referenced from NAVD88 vertical datum) during a storm (September 25 to October 8, 2015)

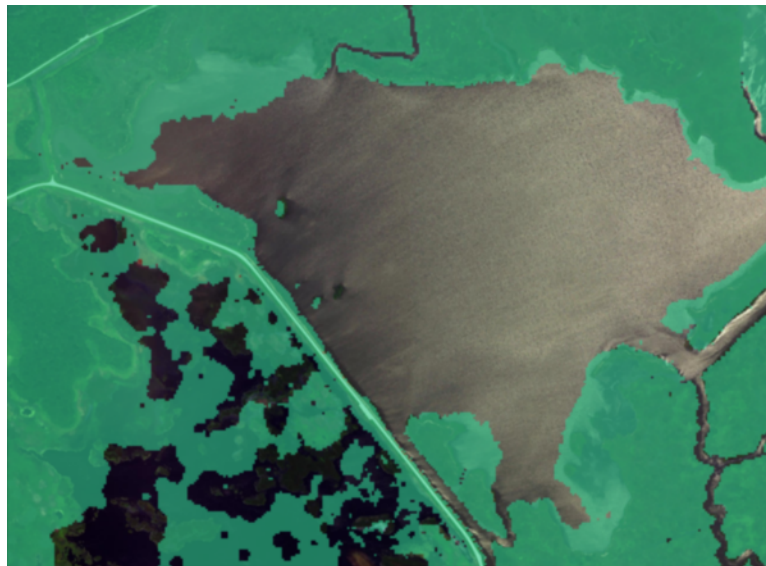


Figure 61: Spatial representation of the vegetation coverage around money marsh tidal flat

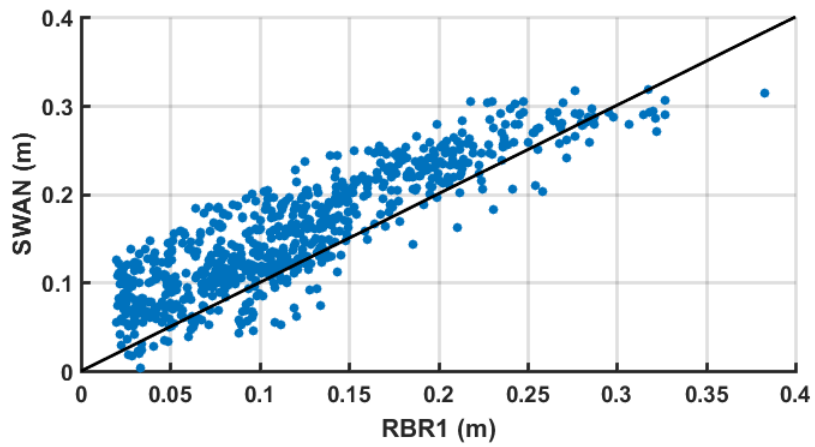
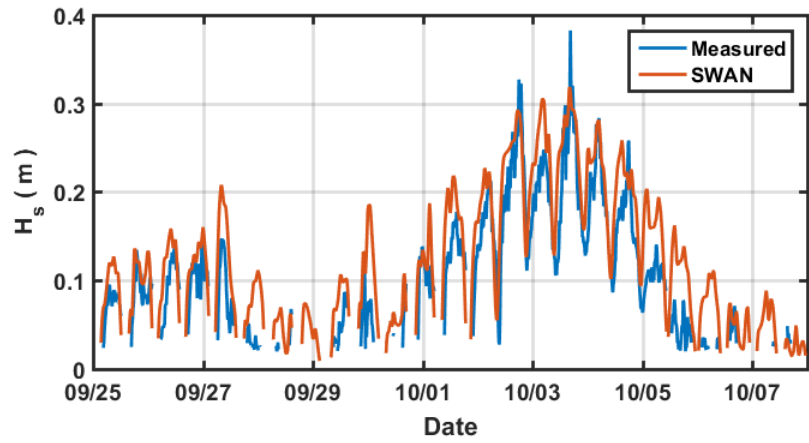


Figure 62: Comparison between SWAN generated and measured significant wave height at RBR1 (in meters)

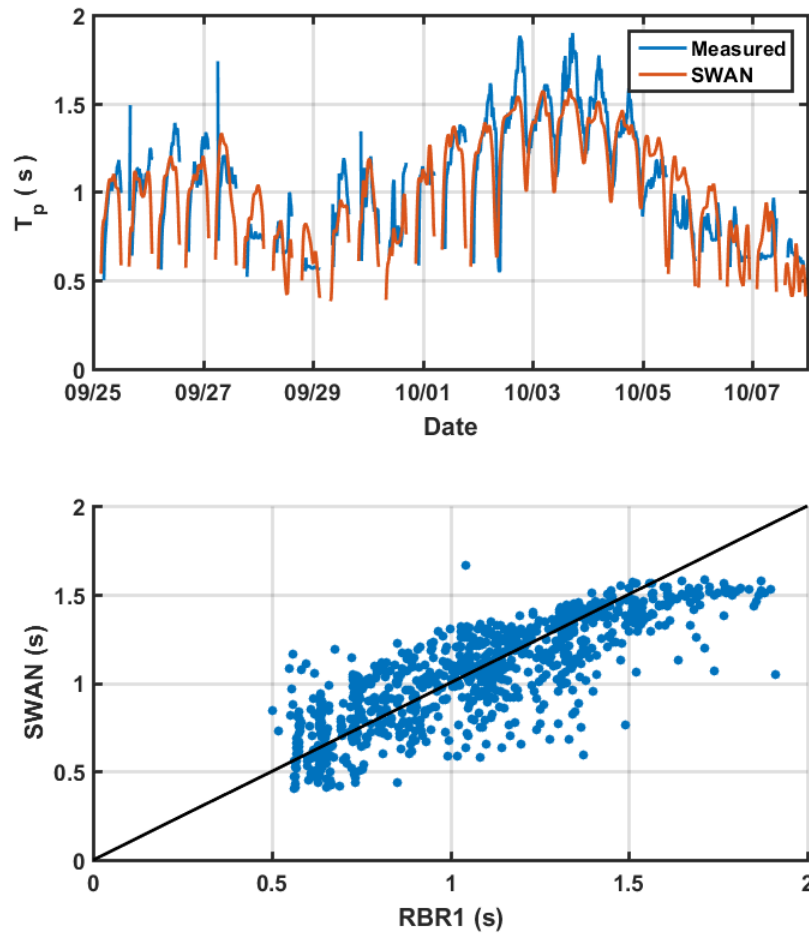


Figure 63: Comparison between SWAN generated and measured peak period at RBR1 (in seconds)

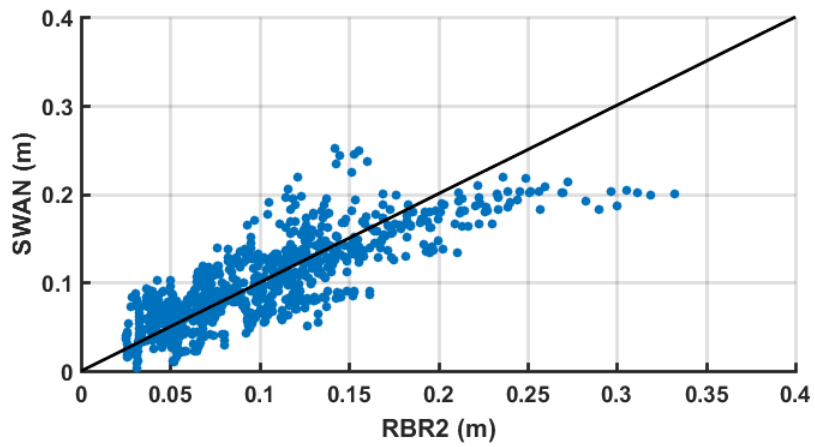
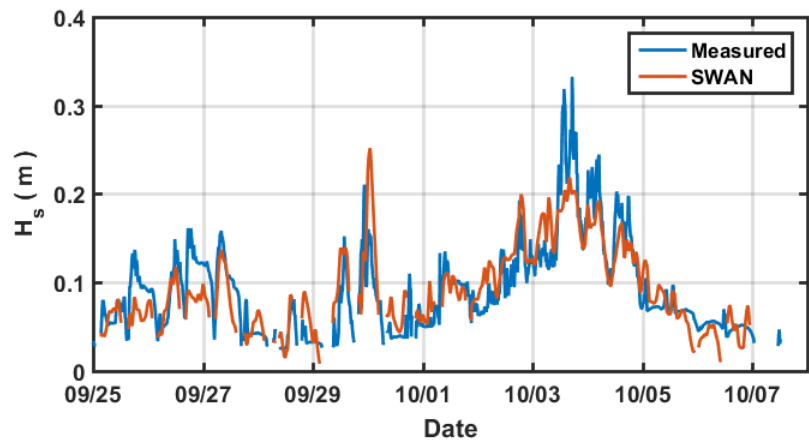


Figure 64: Comparison between SWAN generated and measured significant wave height at RBR2 (in meters)

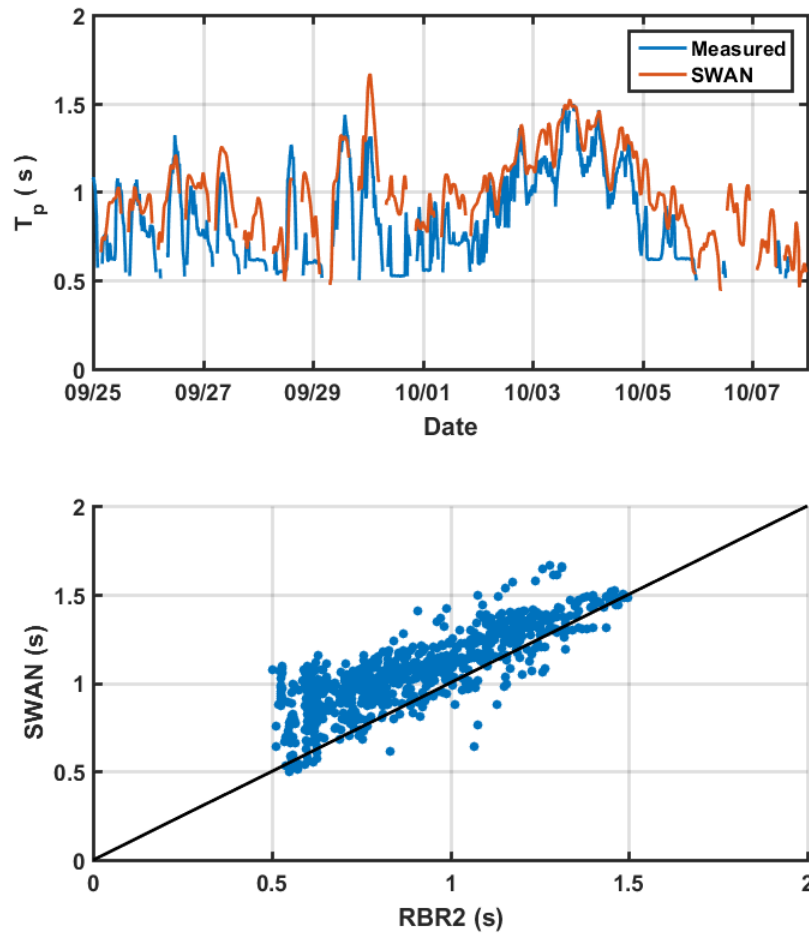


Figure 65: Comparison between SWAN generated and measured peak period at RBR2 (in seconds)

## 6.5 Analytic estimates of fetch limited waves

Wave fields resulting from local winds in our study area are controlled by the fetch width (or distance across the flooded mud flat in the direction of the wind) and finite water depth. In such conditions, the wave growth can be estimated using empirical equations which are depth and fetch dependent. Here, we followed the methodology developed by [Young & Verhagen \(1996a\)](#) for shallow water wave growth, where non-dimensional wave energy and frequency are calculated based on the fetch distance and depth. The methodology is described in section 6.5.1. We then compare predictions of fetch-limited wave growth to model predictions from SWAN in section 6.5.2 in order to examine the accuracy of the simplified approach.

### 6.5.1 Methodology

[Young & Verhagen \(1996a,b\)](#) have collected field data such as wind wave spectra, wind speed and direction from Lake George, a 20 km long lake with uniform bathymetry of 2 m. They tried to evaluate the nondimensional total energy and peak frequency as a function on nondimensional fetch in a water of finite depth. At short fetch, they observed that the waves are in deep water and shows similar growth as seen from JONSWAP relations. On the other hand, at large fetch, evolution of both total energy and peak frequency becomes depth limited. Compared to the single growth law formula as in deep water, there is a family of curves, one for each value of nondimensional depth.

In this study, following [Young & Verhagen \(1996a\)](#), we have nondimensionalized the fetch distance and depth using the gravitational acceleration and characteristic wind velocity at 10 m elevation  $U_{10}$ , and obtain a non-dimensional fetch

$$\chi = \frac{gf_x}{U_{10}^2} \quad (43)$$

and non-dimensional depth

$$\delta = \frac{gh}{U_{10}^2} \quad (44)$$

Here,  $f_x$  is the fetch distance and  $h$  is the water depth.

The dimensionless wave energy and peak frequency are related to the nondimensional fetch and dimensionless water depth. We can express the nondimensional energy as

$$\epsilon = 3.64 * 10^{-3} (\tanh A_1 \tanh \frac{B_1}{\tanh A_1})^{1.74} \quad (45)$$

where

$$A_1 = 0.493\delta^{0.75} \quad (46)$$

$$B_1 = 3.13 * 10^{-3} \chi^{0.57} \quad (47)$$

and the nondimensional frequency as

$$\nu = 0.133 (\tanh A_2 \tanh \frac{B_2}{\tanh A_2})^{-0.37} \quad (48)$$

where

$$A_2 = 0.331\delta^{1.01} \quad (49)$$

$$B_2 = 5.215 * 10^{-4} \chi^{0.73} \quad (50)$$

Here,  $\delta$  is the nondimensional depth and  $\chi$  is the nondimensional fetch.

Now, we can go back to the dimensional energy and peak frequency form using gravitational acceleration and characteristic wind velocity at 10 m elevation to estimate the wave height and peak period. We have calculated wave height  $H$  using the expression  $E = \frac{1}{8}\rho g H^2$ , where  $E$  is the dimensional wave energy.

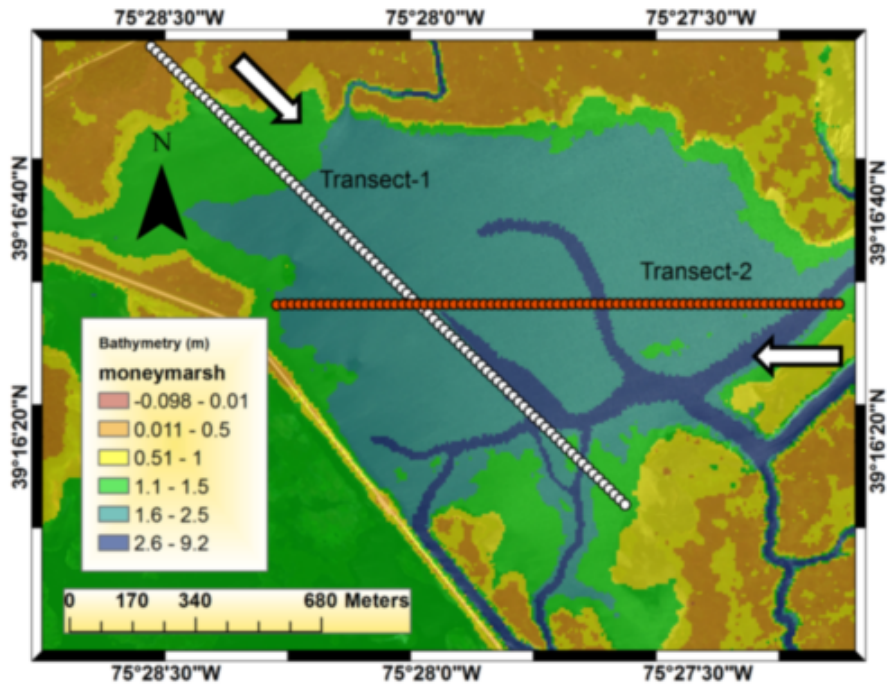


Figure 66: Transects and wind directions to compute wave growth using non-dimensional fetch distance and depth

### 6.5.2 Fetch limited wave growth vs SWAN

The transects representing fetch used in our domain are shown in Figure 66. We selected two transects with the largest possible fetch distance to observe considerable wave growth. Depth at each fetch segment has been estimated taking the average of subsequent transect points. Suppose, if we have 10 points in a fetch segment, then depth for the entire transect distance is taken from the average of all points following the wind direction. This gives a constant depth for each segment and ultimately shows a smooth transition of bathymetry along the fetch (Figure 67 & Figure 68). Results obtained using these empirical equations shows a good match with SWAN results. Significant wave height and peak period estimated from the non-dimensional energy and frequency are almost the same as resulted from SWAN. This comparison helped us to evaluate the significance of both the approaches to model wave

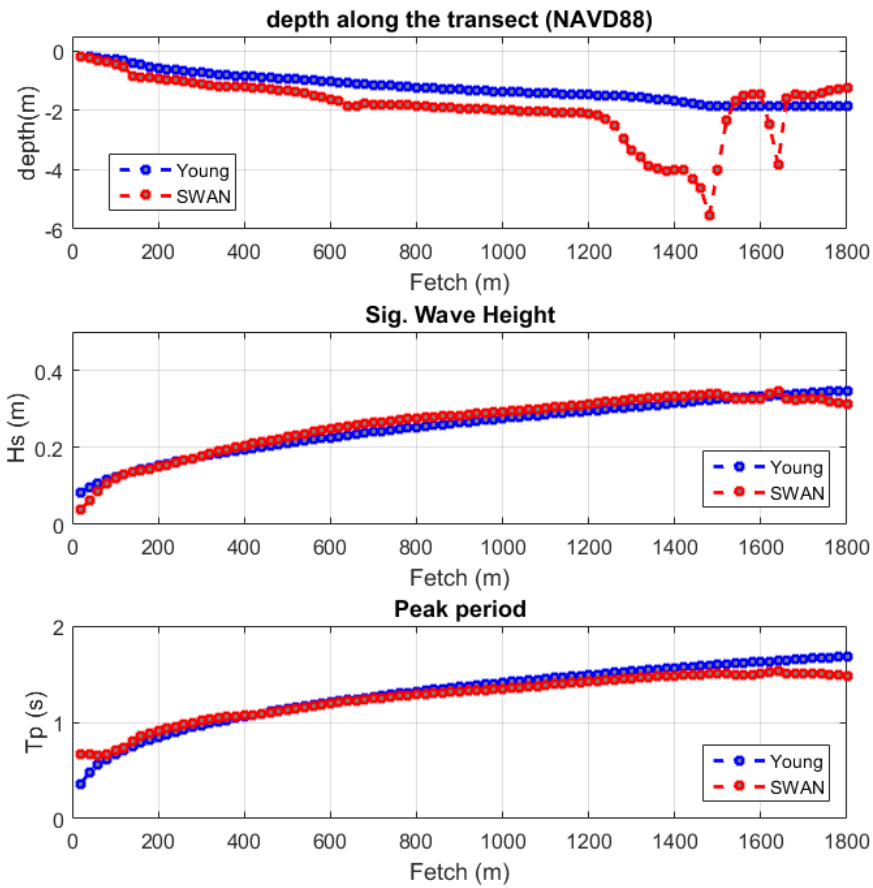


Figure 67: Comparison of depth (in meters) from NAVD88 vertical reference level, significant wave height (in meters) and peak wave period (in seconds) for Fetch-wave and SWAN at Transect 1

climate in any fetch limited environment. Because of its efficiency and simplicity we have used the Fetch-wave methodology extensively in some of our assessments.

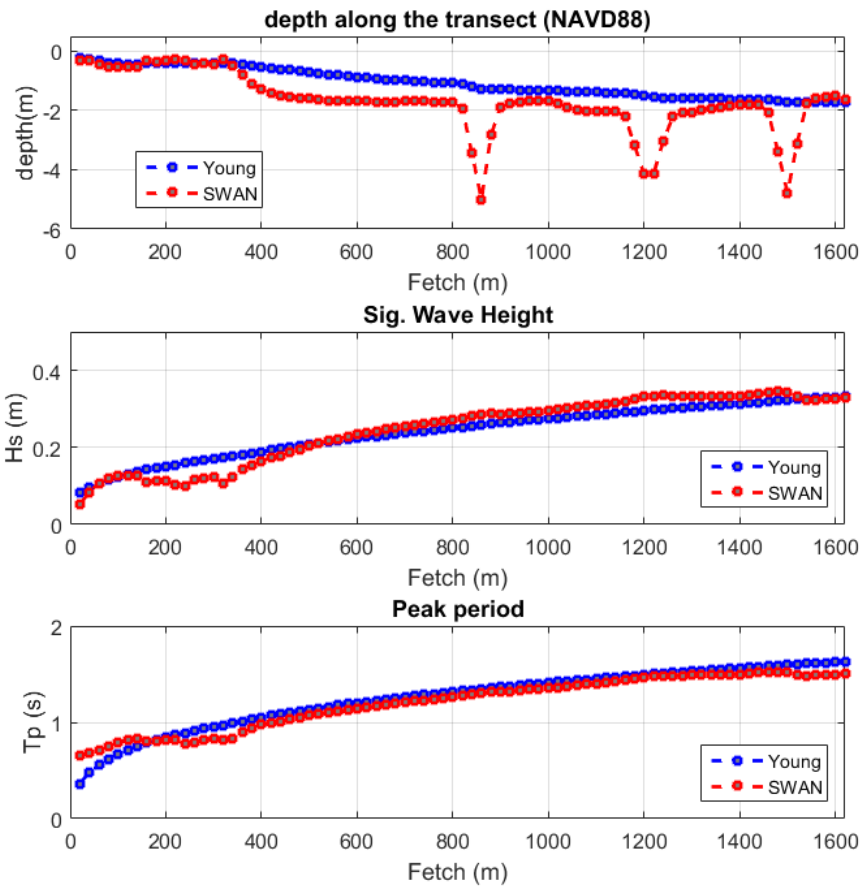


Figure 68: Comparison of depth (in meters) from NAVD88 vertical reference level, significant wave height (in meters) and peak wave period (in seconds) for Fetch-wave and SWAN at Transect 2

## 7 Conclusions

In this study, we have provided an overview of ongoing field and modeling efforts in the 13,000 acres of salt marshes within the Bombay Hook National Wildlife Refuge. The field observations in this study included extensive bathymetric surveying in channels, current velocity measurements using ADCPs in several major channels, tide gauges mounted on the marsh platform, and rapid-sampling pressure gauges deployed in a large tidal flat area located within the marsh and isolated from the open water of the Bay (Deb *et al.*, 2018). We have implemented sophisticated Artificial Neural Network techniques to remove vegetation bias in measured LiDAR elevations, and validated the corrections against ground truth survey data.

The unstructured grid model FVCOM was used as the basis for numerical simulations. The model was run on an unstructured horizontal grid which covered the entire marsh system with sufficient grid resolution to resolve small channels and creeks. The model is driven by current and surface elevations derived from a larger scale ROMS model of Delaware Bay. The FVCOM model validation is carried out using historic tide gauge observations up through 2012 and using a more detailed data set including current meter deployments and measurements of marsh platform inundation in 2015. The model showed good accuracy in reproducing storm events in 2012 (particularly Hurricane Sandy surge levels) and good reproduction of water levels, currents and marsh inundation depths in comparison to data collected for the project.

The FVCOM model is used in 3D with the sediment transport module activated to investigate the ongoing and future changes of hydrodynamics and sediment transport in BHNWR. Preliminary results described the overall wetland system as ebb-dominant, with the Leipsic River and Sluice Ditch being ebb dominant and the Simon River being flood

dominant. The study results show that the opening of Sluice Ditch and the progressive deepening and widening of channels within the marsh has led to a progressively increasing tendency towards ebb-dominance in the overall system. The model predicts that the system is exporting sediment under all conditions tested, but this conclusion may be faulty due to inadequate understanding of sediment supply in the Bay as well as the use of too simple a model of sediment properties.

Wave climate in the tidally-inundated flat, Money Marsh contained within the BHNWR has been studied using field measurements and numerical modeling. Wave modeling has been carried out using the SWAN model, to examine wave growth in both idealized and observed conditions, and compared with a fetch limited wind wave model to evaluate the effect of fetch distances. As the Bombay Hook National Wildlife Refuge is one of the largest wetland system in the U.S. mid-Atlantic region, resolving the interaction between critical processes will certainly provide important remarks which can be implemented at other major wetland systems. This study will provide a platform to develop wetland loss mitigation strategies that help in the long-term resilience of the wetland systems. Finally, the proposed improvement of the commonly used unstructured grid finite volume model would benefit the modeling community by increasing accuracy when dealing with a complex salt marsh environment.

Extensive sediment coring and analysis of sediment accumulation rates has been carried out in a range of low and high marsh regions in BHNWR. This work is reported separately in [McDowell \(2017\)](#).

The results of the study have emphasized the need for further work before the model could be used to assess long term sedimentation problems.

- The prediction of net transport of sediment in the BHNWR system depends on the hydrodynamics, sediment properties and supply from the Delaware River and Bay.

In our preliminary analysis, we have used only one sediment class and a constant supply at the River and Bay boundaries. The chosen ambient sediment conditions has not been calibrated using data from in situ measurements, and could be a significant source of error in the present computations. Measurements leading to a more accurate specification of sediment supply should be an aim of future studies.

- Small features on the marsh platform, such as rills and cuts through channel berms, are often unresolved in the model grid, leading to artificial ponding at artificially isolated depressions in the model DEM. They are missing due to both incomplete resolution in data sources such as LiDAR as well as loss of resolution in the development of DEM's and model grids. In ongoing Sea Grant-funded research, we are adding an artificial porosity to selected areas of the marsh platform, in order to replace the effects of small rills and defects in channel berms. This model enhancement is crucial to obtaining accurate estimates of the depth and duration of inundation, which is crucial in the selection process of vegetation species, and of the volume and speed of flooding and draining processes, which is crucial to estimation of sedimentation rates and marsh platform geomorphological evolution.
- Our study of wave climate in an open tidal flat area has shown that reasonable estimates of wave conditions can be obtained from model simulations or formula-based estimates. Our work was inconclusive in establishing whether the wave climate would play a significant role in accelerating marsh edge erosion and further lateral expansion of the mud flat. Further pursuit of this problem would help to estimate the long term potential for wind wave-driven shoreline erosion and resulting enlargement of the tidal flat. Many state or private organizations who are working on wetland resilience for coastal flood mitigation, wetland ecology or coastal geomorphology would potentially benefit from extensions of this work.

As the Bombay Hook National Wildlife Refuge is one of the largest wetland system in the U.S. mid-Atlantic region, resolving the interaction between critical processes will certainly provide important remarks which can be implemented at other major wetland systems. This study has provided a modeling platform to develop wetland loss mitigation strategies to improve the long-term resilience of the wetland system.

## References

- ABDOLALI, A., GUITERAS, S., CALLAHAN, J., KIRBY, J. T., SHI & MITCHELL, L. 2016a  
vegetation bias correction in tidal salt marsh LidAR data sets with artificial neural networks. In *(RAETCS16) Restore America's Estuaries 8th National Summit on Coastal and Estuarine Restoration and 25th Biennial Meeting of The Coastal Society*. New Orleans, LA.
- ABDOLALI, A., KIRBY, J. T., SHI, F., GUITERAS, S. & DEB, M. 2016b Field and modeling studies of salt marshes in Bombay Hook National Wildlife Refuge in Delaware. In *RAETCS16) Restore America's Estuaries 8th National Summit on Coastal and Estuarine Restoration and 25th Biennial Meeting of The Coastal Society*. New Orleans, LA.
- BOOIJ, N., RIS, R. C. & HOLTHUIJSEN, L. 1999a A third generation wave model for coastal regions 1. model description and validation. *Journal of Geophysical Research* **104** (C4), 7649–7666.
- BOOIJ, N., RIS, R. C. & HOLTHUIJSEN, L. H. 1999b A third-generation wave model for coastal regions: 1. model description and validation. *Journal of Geophysical Research: Oceans* **104** (C4), 7649–7666.

- BOUWS, E., GÜNTHER, H., ROSENTHAL, W. & VINCENT, C. L. 1985 Similarity of the wind wave spectrum in finite depth water 1. spectral form. *Journal of Geophysical Research* **90** (C1), 975–986.
- CAHOON, D. R., REED, D. J., KOLKER, A. S., BRINSON, M. M., STEVENSON, J. C., RIGGS, S., CHRISTIAN, R., REYES, E., VOSS, C. & KUNZ, D. 2009 Coastal wetland sustainability. In *Coastal Sensitivity to Sea-Level Rise: A Focus on the Mid-Atlantic Region*. Washington DC: U.S. Environmental Protection Agency.
- CHEN, C., BEARDSLEY, R. C., COWLES, G., QI, J., LAI, Z., GAO, G., STUEBE, D., LIU, H., XU, Q., XUE, P., GE, J., HU, S., JI, R., TIAN, R., HUANG, H., WU, L., LIN, H., SUN, Y. & ZHAO, L. 2013 An unstructured grid , finite-volume community ocean model FVCOM user manual (3rd edition). *Tech. Rep.* MITSG 12-25. Sea Grant College Program, Massachusetts Institute of Technology.
- CHEN, C., QI, J., LI, C., BEARDSLEY, R. C., LIN, H., WALKER, R. & GATES, K. 2008 Complexity of the flooding/drying process in an estuarine tidal-creek salt-marsh system: An application of FVCOM. *Journal of Geophysical Research* **113** (C07052).
- DALRYMPLE, R. A., KIRBY, J. T. & HWANG, P. A. 1984 Wave diffraction due to areas of energy dissipation. *Journal of Waterway, Port, Coastal, and Ocean Engineering* **110** (1), 67–79.
- DEAN, R. G. & DALRYMPLE, R. A. 1991 *Water wave mechanics for engineers and scientists*. World Scientific.
- DEB, M., ABDOLALI, A., MCDOWELL, C., KIRBY, J. T., SOMMERFIELD, C. K. & SHI, F. 2018 Hydrodynamic, survey and sediment data collection. Bombay Hook National Wildlife Refuge, Delaware. Research Report CACR-18-03. Center for Applied Coastal

- Research, Department of Civil and Environmental Engineering, University of Delaware, Newark, DE.
- DNREC 2007 2007 DNREC Lidar: Kent and New Castle Counties. *Tech. Rep.*. Delaware Department of Natural Resources and Environmental Control.
- ECKART, C. 1952 The propagation of gravity waves from deep to shallow water. In *Gravity Waves*, p. 165.
- ELSEY-QUIRK, T, SELISKAR, D M, SOMMERFIELD, C K & GALLAGER, J L 2011 Salt marsh carbon pool distribution in a Mid-Atlantic lagoon, USA: Implications for sea level rise. *Wetlands* .
- FAGHERAZZI, S., KIRWAN, M. L., MUDD, S. M., GUNTENSPERGEN, G. R., TEMMERMAN, S., D'ALPAOS, A., VAN DE KOPPEL, J., RYBCZYK, J. M., REYES, E., CRAFT, C. & CLOUGH, J. 2012 Numerical models of salt marsh evolution: Ecological, geomorphic, and climatic factors. *Reviews of Geophysics* **50** (1), RG1002.
- FRIEDRICHS, C. T. & MADSEN, O. S. 1992 Nonlinear diffusion of the tidal signal in frictionally dominated embayments. *Journal of Geophysical Research* **97** (C4), 5637.
- GORMAN, R. M. & NEILSON, C. G. 1999 Modelling shallow water wave generation and transformation in an intertidal estuary. *Coastal Engineering* **36** (3), 197 – 217.
- HUND, E. 2013 NOAA orthorectified Digital Elevation Model (DEM) image tiles, Bombay Hook, Delaware, 2011. *Tech. Rep.* NODC Accession 0112173. Coastal Services Center, National Oceanographic Data Center.
- KAUFFMAN, G. J., HOMSEY, A., CHATTERSON, S., MCVHEY, E. & MACK, S. 2011 Economic value of the Delaware estuary watershed. *Institute for Public Administration's Water Resources Agency, University of Delaware* .

- KHANGAONKAR, T., NUGRAHA, A., HINTON, S., MICHALSEN, D. & BROWN, S. 2017 Sediment Transport into the Swinomish Navigation Channel, Puget Sound—Habitat Restoration versus Navigation Maintenance Needs. *Journal of Marine Science and Engineering* **5** (2), 19.
- KUKULKA, T., JENKINS III, R. L., KIRBY, J. T., SHI, F. & SCARBOROUGH, R. W. 2017 Surface wave dynamics in delaware bay and its adjacent coastal shelf. *Journal of Geophysical Research: Oceans* **122**, 8683–8706.
- MCDOWELL, C. 2017 Marsh sediment accumulation and accretion on a rapidly retreating estuarine coast. Ms, University of Delaware.
- MCDOWELL, C & SOMMERFIELD, C K 2016 Geomorphic analysis of Bombay Hook NWR. Wilmington, DE: Delaware Wetlands Conference.
- MENDEZ, F. J. & LOSADA, I. J. 2004 An empirical model to estimate the propagation of random breaking and nonbreaking waves over vegetation fields. *Coastal Engineering* **51** (2), 103–118.
- NOAA 2016 2014 NOAA Post Hurricane Sandy Topobathymetric LiDAR Mapping for Shoreline Mapping. *Tech. Rep.*. National Oceanographic Data Center, NOAA.
- PAWLOWICZ, R., BEARDSLEY, R. C. & LENTZ, S. 2002 Classical tidal harmonic analysis including error estimates in matlab using t\_tide. *Computers & Geosciences* **28** (8), 929–937.
- QIN, W., KIRBY, J. T. & BADIEY, M. 2005 Application of the spectral wave model swan in delaware bay. Research Report CACR-05-09. Center for Applied Coastal Research, Department of Civil and Environmental Engineering, University of Delaware.

- RALSTON, D. K., GEYER, W. R., TRAYKOVSKI, P. A. & NIDZIEKO, N. J. 2013 Effects of estuarine and fluvial processes on sediment transport over deltaic tidal flats. *Continental Shelf Research* **60**, S40–S57.
- RIS, R. C., HOLTHUIJSEN, L. H. & BOOIJ, N. 1999 A third-generation wave model for coastal regions: 2. verification. *Journal of Geophysical Research: Oceans* **104** (C4), 7667–7681.
- RODRIGUES, A. P. F. 2016 Hydrodynamic modeling of Delaware Bay with applications to storm surges and coastal flooding: Current conditions and future scenarios. Master of science in marine studies, University of Delaware, College of Earth, Ocean and Environment.
- SOMMERFIELD, C K & VELINSKY, D 2010 Sediment accumulation and marsh accretion in a coastal plain estuary. In *Eos Transactions*, 26, vol. 91. American Geophysical Union, Ocean Sci. Meet., abstract GO23A-02.
- SOMMERFIELD, C. K. & WONG, K. C. 2011 Mechanisms of sediment flux and turbidity maintenance in the Delaware Estuary. *Journal of Geophysical Research* **116** (1), 1–16.
- STAMMERMAN, R. 2013 Hydrodynamics and sediment transport studies in tidal marshes of the Delaware Bay using high resolution numerical models. PhD thesis, Drexel University.
- USGS 2014 2014 USGS CMGP Lidar: Post Sandy (DE & MD) Point Cloud files with Orthometric Vertical Datum North American Vertical Datum of 1988 (NAVD88) using GEOID12B. [https://coast.noaa.gov/htdata/lidar1\\_z/geoid12b/data/4969/](https://coast.noaa.gov/htdata/lidar1_z/geoid12b/data/4969/). *Tech. Rep.*. US Geological Survey.
- YOUNG, I. R. & VERHAGEN, L. A. 1996a The growth of fetch limited waves in water of finite depth. Part 1. Total energy and peak frequency. *Coastal Engineering* **29** (1), 47 – 78.

YOUNG, I. R. & VERHAGEN, L. A. 1996b The growth of fetch limited waves in water of finite depth. Part 2. Spectral evolution. *Coastal Engineering* **29** (1), 79 – 99.

ZHAO, L., CHEN, C., VALLINO, J., HOPKINSON, C., BEARDSLEY, R. C., LIN, H. & LERCZAK, J. 2010 Wetland-estuarine-shelf interactions in the Plum Island Sound and Merrimack River in the Massachusetts coast. *Journal of Geophysical Research* **115** (C10039).